UNIVERSIDADE ESTADUAL DE CAMPINAS

Faculdade de Engenharia Mecânica

Felipe de Castro Teixeira Carvalho

Characterization of two-phase vertical flow in pipes using flow-induced vibration

Caracterização de escoamentos bifásicos verticais em tubulação utilizando vibração induzida por escoamentos

CAMPINAS

2018

Felipe de Castro Teixeira Carvalho

Characterization of two-phase vertical flow in pipes using flow-induced vibration

Caracterização de escoamentos bifásicos verticais em tubulação utilizando vibração induzida por escoamentos

Dissertation presented to the School of Mechanical Engineering of the University of Campinas in partial fulfillment of the requirements for the degree of Master in Mechanical Engineering, in the area of Mechatronics.

Dissertação apresentada à Faculdade de Engenharia Mecânica da Universidade Estadual de Campinas como parte dos requisitos exigidos para obtenção do título de Mestre em Engenharia Mecânica, na Área de Mecatrônica.

Orientador: Prof. Dr. Alberto Luiz Serpa

ESTE EXEMPLAR CORRESPONDE À VERSÃO FINAL DA DISSERTAÇÃO DEFENDIDA PELO ALUNO FELIPE DE CASTRO TEIXEIRA CARVALHO, E ORIENTADO PELO PROF. DR. ALBERTO LUIZ SERPA.

CAMPINAS
2018

Agência(s) de fomento e nº(s) de processo(s): FUNCAMP, 01-P-20041/2015

Ficha catalográfica
Universidade Estadual de Campinas
Biblioteca da Área de Engenharia e Arquitetura
Luciana Pietrosanto Milla - CRB 8/8129

C253c

Carvalho, Felipe de Castro Teixeira, 1993-
Characterization of two-phase vertical flow in pipes using flow-induced vibration / Felipe de Castro Teixeira Carvalho. – Campinas, SP : [s.n.], 2018.

Orientador: Alberto Luiz Serpa.
Dissertação (mestrado) – Universidade Estadual de Campinas, Faculdade de Engenharia Mecânica.

1. Processamento de sinais. 2. Escoamento bifásico. 3. Escoamento multifásico. 4. Vibração. I. Serpa, Alberto Luiz, 1967-. II. Universidade Estadual de Campinas. Faculdade de Engenharia Mecânica. III. Título.

Informações para Biblioteca Digital

Título em outro idioma: Caracterização de escoamentos bifásicos verticais em tubulação utilizando vibração induzida por escoamentos
Palavras-chave em inglês:
Signal processing
Two-phase flow
Multiphase flow
Vibration
Área de concentração: Mecatrônica
Titulação: Mestre em Engenharia Mecânica
Banca examinadora:
Alberto Luiz Serpa [Orientador]
Oscar Maurício Hernandez Rodriguez
Tiago Henrique Machado
Data de defesa: 16-08-2018
Programa de Pós-Graduação: Engenharia Mecânica

UNIVERSIDADE ESTADUAL DE CAMPINAS

FACULDADE DE ENGENHARIA MECÂNICA

COMISSÃO DE PÓS-GRADUAÇÃO EM ENGENHARIA MECÂNICA

DEPARTAMENTO DE MECÂNICA COMPUTACIONAL

DISSERTAÇÃO DE MESTRADO ACADÊMICO

Characterization of two-phase vertical flow in pipes using flow-induced vibration

Caracterização de escoamentos bifásicos verticais em tubulação utilizando vibração induzida por escoamentos

Autor: Felipe de Castro Teixeira Carvalho
Orientador: Prof. Dr. Alberto Luiz Serpa

A Banca Examinadora composta pelos membros abaixo aprovou esta Dissertação:

Prof. Dr. Alberto Luiz Serpa, Presidente
DMC/FEM/UNICAMP

Prof. Dr. Oscar Maurício Hernandez Rodriguez
DSI/FEM/UNICAMP

Prof. Dr. Tiago Henrique Machado
SEM/EESC/USP

A Ata da defesa com as respectivas assinaturas dos membros encontra-se no processo de vida acadêmica do aluno.

Campinas, 16 de Agosto de 2018.

Dedication

This dissertation is dedicated to my parents.

Acknowledgement

Foremost, I would like to express my profound gratitude and sincere thanks to my advisor Prof. Dr Alberto Luiz Serpa for the continuous support of my master study and related research, for his patience, motivation, and immense knowledge. His guidance supported me throughout my research and writing of this dissertation. I am profoundly grateful for the opportunity.

Besides my advisor, I would like to thank my qualification committee: Prof. Dr Tiago Henrique Machado and Prof. Dr Ricardo Augusto Mazza, for their insightful comments, support and also for the hard questions which incented me to widen and improve my research from various perspectives.

My sincere thanks also go to Prof. Dr Ana Maria Frattini Fileti and Dr Valdir Estevam who gave me access to the research facilities. Without their valuable support, it would not be possible to conduct this research.

My most sincere gratitude to MSc. Maurício de Melo Freire Figueiredo, who encouraged me to research this subject. Without his effort, this research would not be possible. I also thankful for his support on the experimental development, support on two-phase flows and for the stimulating discussions.

For the support, friendship and all the fun we have had in the last two years, my sincere thanks to my fellow labmates Luis Felipe Barrera, Luis Fernando Pineda, Camilo Ariza and Maurício Barrios.

I thank the Center for Petroleum Studies of the University of Campinas for the facilities, and I also thank the Artificial Lift and Flow Assurance research group which supported and provided valuable advice in the experimental assembly.

I thank the FUNCAMP, Queiroz Galvão - Exploration and Production and ANP ('Compromisso de Investimentos com Pesquisa e Desenvolvimento') for the financial support.

Finally, I express my most sincere gratitude to my parents and my brother, for supporting me throughout my master study and my life.

Let us strive for the impossible. The great achievements throughout history have been the conquest of what seemed the impossible.

Charlie Chaplin

Resumo

O escoamento multifásico é caracterizado pela passagem simultânea de duas ou mais fases em um determinado sistema. Ele ocorre em diferentes indústrias o que levou ao desenvolvimento de técnicas capazes de medir uma ou mais propriedades do escoamento. Assim, o objetivo geral deste trabalho foi desenvolver uma técnica de medição multifásica utilizando vibração induzida por escoamento em escoamentos verticais bifásicos em tubulações.

Os mecanismos de vibração em escoamentos monofásicos de líquido ou gás é razoavelmente conhecido. Contudo, apesar dos recentes desenvolvimentos no caso de escoamentos bifásicos, o conhecimento de vibrações induzidas por esse escoamento ainda necessita de um maior desenvolvimento quando comparado com escoamentos monofásicos.

Diversas técnicas de processamento sinal como transformada de Fourier, transformada de Hilbert, filtros digitais, técnicas de análise em tempo-frequência, função de correlação e algoritmos de detecção de picos foram revisados e apresentados.

A bancada experimental utilizada na medição de sinais de vibração foi montada no LABPETRO situado no CEPETRO da Universidade Estadual de Campinas. Ela possui uma linha bifásica capaz de medir de forma independente a fração volumétrica de gás presente no escoamento bifásico. Além disso, o escoamento bifásico foi filmado utilizando uma camera de alta velocidade.

Os resultados da análise no domínio do tempo indicaram um aumento sutil nas amplitudes de uma banda específica em padrões de escoamento que são notórios pela passagem periódica de gás e líquido. Assim, o sinal de vibração foi analisado utilizando técnicas de análise em tempo-frequência. Além disso, o módulo da transforma de Hilbert, envelope, do sinal de vibração também foi utilizado.

Utilizando um algoritmo de detecção de pico no envelope do sinal de vibração foi possível obter a passagem média de pistões de líquido. Além disso, fazendo a correlação cruzada entre dois acelerômetros posicionados distantes entre si na tubulação, foi possível obter a velocidade da bolha de Taylor. Foi obtido também uma relação quadrática entre o desvio padrão do envelope e a fração volumétrica de gás. Ademais, foi possível classificar o padrão de escoamento utilizando o valor eficaz do envelope e o coeficiente de correlação de Pearson.

Os resultados apresentados estão coerentes com a atual literatura. Além disso, a ideia de se analisar a variação da amplitude de uma determinada banda de frequência pode ser generalizada para outros sistemas semelhantes.

Palavras-chave: Processamento de sinal; Vibração induzida por escoamento; Escoamento bifásico ; Escoamento multifásico; Identificação de padrão de escoamento; Medição de velocidade.

Abstract

The multiphase flow is the simultaneous passage of a stream composed of two or more phases in a specific system. It occurs in different industries which encouraged the development of techniques that are capable of measuring the multiphase flow properties. Thus, the overall objective of this study was to develop a multiphase flow metering technique based on the flow-induced vibration of vertical upward two-phase flows in piping systems.

Nowadays the vibration mechanisms in single-phase flow, liquid or gas flow, are reasonably well understood. On the other hand, despite the recent progress and development in two-phase flows, the knowledge and understanding of flow-induced vibrations by two-phase flow are still far behind when compared to single-phase flows.

A few signal processing tools such as Fourier transform, Hilbert transform, digital filters, time-frequency analysis, correlation functions and peak detection algorithms were reviewed. Moreover, a few fundamental concepts of two-phase flows were presented.

The experimental apparatus required to perform the proposed vibration analysis was assembled in the LABPETRO at the CEPETRO, which is located at the UNICAMP. It has a two-phase line that was capable of measuring the gas void fraction in the two-phase flow line independently. Moreover, the two-phase flow was recorded by a high-speed camera.

The results of frequency domain analysis indicated a subtle increase in the amplitudes of a specific frequency band in flow patterns that are notorious for being oscillatory regarding liquid and gas passage. Thus, the vibration signal was analysed using time-frequency tools that showed a significant change of the frequencies amplitudes along the time. Then, the modulus of the Hilbert transform was used to analyse the signal.

Finally, using the envelope of the vibration signal with peak detection algorithms, it was possible to get the slug mean frequency. Moreover, with the cross-correlation between two accelerometers placed in a different position along the pipe, it was possible to get the 'Taylor bubble' velocity. It was found a quadratic relationship between the standard deviation of the envelope and the gas void fraction. Also, it was possible to classify the flow pattern by taking root mean square and Pearson correlation coefficient of the envelope.

The results presented were found to be consistent with the currently available literature. Moreover, the idea of analysing the amplitude variation of a specific band can be generalised to the other systems.

Keywords: Signal processing; Flow-induced vibration; Two-phase flow; Multiphase flow; Flow pattern identification; Velocity measurement.

List of Figures

List of Tables

Nomenclature

Greek Symbols

α	Gas void fraction
θ	Pipe inclination angle
δf	Frequency resolution
δt	Time discretisation
Γ	Théron constant
μ_G	Gas viscosity
μ_L	Liquid viscosity
μ_M	Average two-phase viscosity
ρ_G	Gas specific mass
ρ_L	Liquid specific mass
ρ_M	Average two-phase specific mass

Other Symbols

A_p	Area of the pipe cross-section
d	Pipe diameter
f	Frequency
Fr_l	Foude number of the liquid phase
g	Gravity
h_{Fe}	Liquid film thickness
H_L	Liquid holdup
H_{LLS}	Liquid holdup in the liquid slug body
H_{LTB}	Liquid holdup in the 'Taylor bubble'
j	Unit imaginary number

L_F 'Taylor Bubble' length

L_S Liquid slug body length

L_v Slug unit length

q Total volumetric flow rate

q_G Gas volumetric flow rate

q_L Liquid volumetric flow rate

$\mathbb{R}$ The set of real numbers

Re_M Mixture Reynolds number assuming non-slip condition

t Time

v_D Drift velocity

v_G Gas actual velocity

V_{GLS} Gas velocity in the liquid slug body

v_s Slug frequency

V_{GTB} Gas velocity inside inside the 'Taylor bubble'

v_L Liquid actual velocity

V_{LLS} Liquid velocity in the liquid slug body

V_{LTB} Velocity of the front of the 'Taylor bubble'

V_{LTBe} Velocity of the liquid film at the beginning of the liquid slug body

v_M Mixture velocity

v_{SG} Gas superficial velocity

v_{SL} Liquid superficial velocity

V_{TB} 'Taylor bubble' translational velocity

W Total mass flow rate

W_G Gas mass flow rate

W_L Liquid mass flow rate

Acronyms / Abbreviations

AC Alternate current

AMPD Automatic multiscale-based peak detection

CEPETRO Centre for Petroleum Studies

2-FIV Flow-induced vibration by two-phase flows

FIV Flow-induced vibration

GVF Gas void fraction

DC Direct current

DFT Discrete Fourier transform

ESD Energy spectral density

FFT Fast Fourier transform

fps Frames-per-second

GVF Gas void fraction

LABPETRO Experimental Laboratory of Petroleum Kelsen Valente Serra

LED Light emitter diode

MFM Multiphase flow metering

PSD Power spectral density

PS Power spectrum

RAM Random-access memory

DC Direct current

RMS Root mean squared

RSS Root sum squared

STFT Short time Fourier transform

TFA Time-frequency analysis

Contents

1 Introduction

1.1 Multi-phase flow

According to Falcone [1], a general definition of multiphase flow is the simultaneous passage of a stream composed of two or more phases in a specific system. In this context, the multiphase flow is not only the most common flow occurrences in nature but also it occurs in various major industrial fields. It ranges from the flow of blood in the human body to oil-water-gas-sand mixtures in risers in offshore oil and gas development [1, 2].

The most straightforward case of multiphase flow is the two-phase flow. It occurs when the same pure substance is present in two different phases, such as steam-water. Alternatively, if different chemical substances co-exist in a flow, they can also be referred to as two-phase flow, for instance, air-water flow [1]. In a multiphase flow, the interaction between the phases results in behaviour and shape of the interfaces which is referred to as 'flow pattern'. They are a result of competing forces or mechanisms occurring within the multiphase flow at the same time. The resultant force dictates the flow pattern [1].

In the context of two-phase flow, they are encountered in industries such as petroleum, chemical, nuclear, space and geothermal industries. In the case of the petroleum industry, the flow occurs during the transportation of oil and gas with horizontal, inclined and vertical pipes. In the chemical industry, the two-phase flows are encountered in a wide range of applications such as reactors, boilers, condensers and evaporators. In the nuclear industry, the two-phase flow is only considered for safety purposes, where the counter-current flow situation is studied. In geothermal energy plants, the two-phase flow occurs as steam-water flow in vertical risers and gathering system pipelines. In space industry, it occurs in what is called zero-gravity flow. Thus, zero-gravity two-phase flows occur in life support systems of space stations and thermal management [2].

1.2 Multiphase flow metering

The occurrence of multiphase flow in the industry encourages the development of techniques that are capable of measuring the flow rates of each phase in multiphase flow. This process is called 'multiphase flow metering' (MFM). According to Falcone [3], the development of MFM was initially driven by instrument engineers in the early 1980s. However, the first MFM commercially appeared only in the late 1990s focused on applications for oil and gas industry.

In the context of MFM, there is an interest in measuring different properties of the multiphase flow such as density and phases velocities. Thus, a large variety of measurement systems

were developed, each one intending to measure one or more of those properties. According to Falcone [4], there is a wide range of MFM techniques for each property. However, according to Figueiredo *et al.* [5], most of the current techniques to measure multiphase flow still requires additional development to be used as multiphase flow meters.

In the phases velocities case, the main measurement principle used is vortex shedding, acoustic, electromagnetic, pulsed photon activation, pulsed neutron activation, radioactive tracer and optical particle-tracking methods [4]. In the density measurement, there are more techniques than the phase velocities case, and some of the measurement principle are gamma-ray scattering [6], neutron absorption, microwave attenuation, infrared, acoustic [7, 5], impedance [8, 9, 10, 11] and tomography [12].

In the context of MFM, according to Silva *et al.* [8], the optical measurement technique is often not accessible due to the presence of opaque fluids or high to moderate interfacial area density. Silva *et al.* [8] mention that tomography visualisation is particularly attractive to MFM, once it non-invasively visualises the flow in a wide variety of industrial problems. According to Silva *et al.* [8], the tomography methods can mainly be divided into two approaches, one is the electrical tomography, and the other is radiation-based tomography techniques. The electrical tomography based techniques are easy to install, inexpensive and potentially fast. On the other hand, Figueiredo *et al.* [5] mention that radioactive methods have a high cost associated with the environmental, health and safety requirements.

1.3 Flow-induced vibration

According to Nakamura and Kaneko [13], in many industrial plants the fluid flow generates vibration and noise. In extreme cases, the flow-induced vibration affects the performance of the industrial plants, once it can cause problems such as fatigue cracks and fretting-wear [14]. This failure obstructs the smooth operation of a plant, and in severe cases can lead to significant maintenance and repair costs and losses in productivity. Thus, the proper knowledge of the flow-induced vibration is required to design and operate system subjected to flows.

Nakamura and Kaneko [13] mention that in unsteady flows the fluid forces acting on an obstacle will vary and thus the force over it, which may cause the vibration of the obstacle. Even in steady flow conditions vibration may be caused by vortex shedding behind obstacles or in turbulent flows due to the pressure fluctuations [13, 15].

In the context of multiphase flow, Ortiz-Vidal, Rodriguez and Mureithi [16] mention that in many industries, the multiphase flow, as the single-phase flow, is a source of structural excitation. Ortiz-Vidal, Rodriguez and Mureithi [16] also mention that there are studies that found a substantial dependence of the structural excitation response on the multiphase flow parameters. However, despite the proper design of system subjected to flows, the vibration may still occur, once it is an intrinsic part of the operation [16].

1.4 Objectives

The overall objective of this study is to develop a technique based on the flow-induced vibration to characterize vertical upward two-phase flows in piping systems. The technique should be able to measure the two-phase flow properties solely using the vibration signal and signal processing tools. The experimental bench was instrumented and a supervisory program was developed to control the experimental bench and perform the vibration measurements.

The specific objectives are:

- Install the required instrumentation in the experimental bench;
- Develop an experimental procedure to perform the measurements;
- Develop the supervisory program that controls the experimental apparatus;
- Implement the experimental procedure in the supervisory program to automate it;
- Filming the two-phase flow;
- Synchronise the vibration signal with the filming;
- Identify the 'Taylor bubble' passage in a water-air flow;
- Calculate the average slug frequency in a water-air flow;
- Estimate the 'Taylor bubble' velocity by using cross-correlation between two vibration signals;
- Correlate the vibration signal with the gas void fraction in a water-air flow;
- Identify the flow pattern in a water-air flow.

2 Literature review

This chapter starts by briefly outlining the historical development in flow-induced vibration by mentioning the firsts work in related subject. Additionally, the main works are mentioned and the current classification of flow-induced vibration phenomena is presented. Also, a few recent works are also mentioned. Finally, a specific review in flow-induced vibration in pipes are presented.

2.1 Flow-induced vibration

2.1.1 General aspects of flow-induced vibration

According to Kaneko *et al.* [17], the first conferences on fluid-related vibration dates back to 1972 and 1979. Those conferences presented a wide variety of practical problems related to flow-induced vibration from different industrial fields such as mechanical systems, aircraft, ships, nuclear power plants and civil engineering. Kaneko *et al.* [17] mentions that the results presented in those conferences are still relevant today. However, it was by Blevins [18] that the term flow-induced vibration (FIV) became popular. It was by Blevins [18] that the FIV phenomenon was first classified into steady and unsteady flow related [19, 17]. Not long later, Blevins [20] published a handbook which focuses on frequencies and eigenmodes of structural and fluid systems related to FIV. Those works developed the first guide to analyse the FIV related problems [19].

Pettigrew *et al.* [14] mention that the vibration mechanisms in single-phase flows,liquid or gas flows, are reasonably well understood. On the other hand, despite the recent progress and developments in two-phase flows, the knowledge and understanding of flow-induced vibrations by two-phase flows (2-FIV) are still far behind when compared to FIV in single-phase flows, and it is still considered an open topic [14, 21, 22, 23, 24]. In this context, Kaneko *et al.* [17] classify the FIV mechanisms that had already been confirmed according to the type of flow involved. The authors based on the Blevins [18] classification, mentioned above, adding the two-phase flow mechanism.

The steady flow mechanism can be divided into the external and internal flow. In the external flow, the vibration mechanism is vortex induced vibration, acoustic resonance and fluid-elastic vibration. The unsteady flow can be divided into pulsating flow, turbulent flow and sudden change in flow. In unsteady flow, the vibration mechanisms of the pulsating flow are forced vibration and acoustically induced vibration. In the turbulent flow, the vibration mechanism is the random vibration. Finally, the sudden change in flow is due to pressure pulsation.

According to Kaneko *et al.* [17], the vibration in steady flows is the most common scenario. It occurs due to the mutual interaction between the fluid and structure which leads to the vibration amplitudes to increase. In the unsteady flow, the turbulence is the primary source of structural vibration [17].

According to Miwa, Mori and Hibiki [19], the two-phase flow vibration mechanisms are considerably different from the single-phase case, due to complex interactions between the phase and the phase change in heat transfer case. Kaneko *et al.* [17] classify the two-phase FIV into bubble-induced vibration, thermal-hydraulic vibration with phase change and vibration of piping by the two-phase flow [17]. The bubble induced vibration occurs due to the bubbles, with various shapes and sizes. They induce fluctuations, sloshing and disturbances within the flow fields [19]. The thermal-hydraulic vibration with phase change is associated with the fluid phase change due to heat transfer. Miwa, Mori and Hibiki [19] mention that the boiling and condensation are highly unstable and has oscillatory behaviour. In vibration of piping, the FIV is due to oscillating fluid flow, and when the flow velocity surpasses a critical value [17].

Vidal and Rodriguez [21] mention that the most of studies done in FIV and 2-FIV are from the nuclear industry. In 2-FIV case, most of the studies are related to cross-flow and axial-flow. In these cases, the 2-FIV studies are associated with heat-exchangers and steam generators in the nuclear industry. These fields are considerably more active with recent developments, as can be seen in Pettigrew and Taylor [22], Pettigrew *et al.* [14], Sasakawa, Serizawa and Kawara [25], Païdoussis [26], Khushnood *et al.* [27], Kanizawa, Oliveira and Ribatski [28], Sadek, Mohany and Hassan [29], Jiang *et al.* [30] and Shaaban and Mohany [31]. On the other hand, due to the relatively low velocities of the two-phase flow in nuclear industry, the 2-FIV in pipes are not relevant to this industry [21, 14].

2.1.2 FIV in pipes

Pipes system are broadly used to carry fluids in many different industrial fields, ranging from oil and nuclear industries to biological engineering systems [32]. Thus, the piping vibration is a relevant subject to the industry in general. According to Kaneko *et al.* [32], the research on stability and vibration of pipe carrying fluid started in the 1950s to design of pipelines carrying oil. Since then, the instabilities phenomena from pipes conveying single-phase flows has been studied in many works, and the dynamic characteristics are now well understood. Moreover, it is known that the pipe dynamics are highly sensitive to flow velocity and support conditions [32]. According to Sinir and Demir [33], the studies in dynamics and vibrations of pipes conveying fluid have seen a growth in last years. However, those studies are mainly focused on the fluid-structure interaction, and the dynamics of pipes under single-phase flows in different flow conditions as presented in Gorman, Reese and Zhang [34], Ozöz [35], Lee and Chung [36], Li *et al.* [37], Ni, Zhang and Wang [38] and Li, Liu and Kong [39].

Although the pipe-conveying-fluid dynamics it is well known, to date, the FIV and 2-FIV in

pipes have considerably less research. Furthermore, when compared to FIV, the 2-FIV case has even less information available, with very few research performed on liquid-gas two-phase flow-induced vibration. In 2-FIV case, there are also a few works that study pipe elbows subjected to two-phase flows such as in Riverin and Pettigrew [24] and Giraudeau, Mureithi and Pettigrew [40]. There is also a few studies in pipe elbows subject to single-phase flows such as in Tian *et al.* [41].

According to Vidal and Rodriguez [21], relevant information of single-phase and two-phase flows can be obtained by analysing the vibration of a structure subjected to those flows. Thus, it is possible to indirectly measure the flows features that otherwise are difficult or unknown. The use of vibration signal in attempt to characterise the flow inside the pipe has received attention and more research efforts in the past decades. One of the first works on this topic is presented by Evans, Blotter and Stephens [42]. The authors investigated the possibility of developing a single-phase flow-rate measurement technique by merely using the standard deviation of the vibration signal of an accelerometer attached to the pipe surface. The results presented by Evans, Blotter and Stephens [42] show a quadratic relationship between the signal standard deviation and the flow rate.

Later, Gama *et al.* [43], similarly to Evans, Blotter and Stephens [42], also used an accelerometer placed on the surface of a U-pipe to correlate the vibration signal with the flow properties. However, differently from Evans, Blotter and Stephens [42], the authors measured the vibration signal of liquid-gas two-phase flow and tried to correlate it with the flow mixture velocity using the RMS of the vibration signal. Furthermore, Gama *et al.* [43] used the variation of the second natural frequency to correlate with the GVF.

In a more recent study and also with two-phase flow, Hua *et al.* [44] used a machine learning algorithm based on *support vectorial machines* (SVM) to elaborate a classifier that can identify the two-phase flow pattern, by merely measuring the vibration signal of a horizontal pipe with an accelerometer. The authors used the signal power spectral density associated with wavelet packet transform to reduce the problem of dimensionality. The authors were able to identify the flow pattern correctly with $93.3\,\%$ of accuracy. However, as a supervised machine learning algorithm, the proposed algorithm requires data to be trained. Vidal and Rodriguez [21] mention that the Hua *et al.* [44] work was remarkable progress in the ability to extract flow features from the vibration signal.

Later, Geng, Ren and Hua [45] developed an analytical relationship between the standard deviation and the Lockhart-Martinelli parameter. Then, the authors used the ratio between the standard deviation of the vibration signal of a horizontal pipe subjected to different two-phase flow and a single-phase gas flow, to correlate it with the Lockhart-Martinelli parameter and the gas mass fraction. Similarly to Hua *et al.* [44], Geng, Ren and Hua [45] used the entropy of the energy of the wavelet packet transform, to correlate the vibration signal with the two-phase flow pattern. They were able to classify with reasonable accuracy the stratified and slug flow, but the annular presented no relationship.

Later, Ortiz-Vidal, Rodriguez and Mureithi [16] performed a series of experiments in horizontal two-phase flow with a tri-axial accelerometer placed on the surface of a straight pipe. The authors only measured the vibration in two axes. Then, the authors used a dimensionless spectrum, to contour the frequency shift due to the flow velocity, in attempt to detect the flow pattern by using the transversal accelerometers. They also presented the standard deviation of the vibration signal with the Mandhane, Gregory and Aziz [46] flow pattern map for a horizontal pipe. They found that the variance of the vibration signal and mixture Reynolds number has a quadratic relationship for GVFs lower than $25\,\%$ and higher than $95\,\%$.

In the most recent work, Ortiz-Vidal, Mureithi and Rodriguez [15] presented a comprehensive analytical formulation for horizontal pipes subjected to two-phase flow. The authors also validated their formulations experimentally with an in-depth discussion on the nature of the flow excitation and parameters. One of the analytical formulations derived, differently from previous works, correlates the standard deviation of the vibration signal with the shear velocity. They corroborated their formulations with experiments which presented a solid relationship. The other analytical formulation presented, correlates the peak-frequency with the GVF by using the hydrodynamic mass of the two-phase flow. They predicted the peak-frequency analytically and posteriorly validated it experimentally.

3 Theory

This chapter presents a brief overview of the theory used in this study. Thereunto, this chapter is divided into six sections. The first section gives an overview of signals. The second outlines the signal processing tools used in this study. The third section gives a brief review of the two time-frequency analysis tools. The fourth brief presents the correlation between signals. The fifth presents the peak detection algorithm used in this work. Finally, the sixth section presents the characteristics of two-phase flows.

3.1 Signals

This section gives a brief overview of signals concepts and outlines their main characteristics.

3.1.1 Signals concepts

According to Shin [47], the observed data that represents a physical phenomenon is referred to as a time history or a signal. A signal can be classified as analog, discrete time, or digital. The analog signal is continuous in time and represents the time-dependent phenomenon behaviour. In the discrete time signals, the information about the phenomenon is only available at discrete points of time. It is commonly a result of inherent or imposed sampling procedure of a continuous variable. As a result, the discrete time signal is characterised to be composed of a finite sequence of numbers equally spaced in time [47, 48, 49].

A digital signal is mainly used when the data acquisition and processing are performed digitally, using a digital computer. The digital signal is not only discrete in time as a discrete time signal, but also discrete in its magnitude. The magnitude discretisation procedure is known as quantisation. It assigns a single number to represent a range of magnitude of a continuous signal [48].

Furthermore, a signal can be characterised by its behaviour along the time. If it does not change in time, it is a static signal otherwise it is a dynamic signal. However, if the phenomenon being observed does vary in time, but in an extremely slow manner when compared with processes that it interacts, the signal can be considered a static signal [48, 47].

The dynamic signal, on the other hand, is by definition a time-dependent signal. It is in general classified as deterministic or random. The deterministic signal can be divided into periodic or non-periodic where the periodic signal can be classified as sinusoidal or complex periodic. The non-periodic signal is classified as almost periodic or transient. Finally, the random signal is divided into stationary or non-stationary [47, 48, 49].

The deterministic signal predictably varies in time, and its values are wholly specified at any given time. On the other hand, the non-deterministic signal has a behaviour that cannot be predicted precisely. Moreover, it does not have a discernible pattern of repetition. In general non-deterministic signals can be described by their statistical characteristics. Thus the usual approach to analysing them are probabilistic and statistical methods [47, 48, 49].

Shin [47] argue that the fundamental difference is whether the signal is random or deterministic, once the methods used to analyse these type of signals are considerably different. Shin [47] further points out that a real-world signal is in general mixed and therefore, the signal type is not apparent, and the classification is not straightforward. In these cases, some prior knowledge of the system or signal is extremely helpful in selecting the proper method. Moreover, Shin [47] also mentions that in many cases the signal classification might be debatable and that it is common to model the signals as a mixture of deterministic and non-deterministic signals. Finally, Shin [47] emphasise, that any assumption or prior knowledge can also be a source of misleading results.

3.1.2 Deterministic signal

As the word periodic suggest, a periodic signal is defined as those whose its waveform strictly repeats at regular time intervals. The most straightforward example of a periodic signal is a sinusoidal signal. However, Shin [47] points out that in reality, generate or measure a genuinely periodic signal is complicate, even if the signal and system are carefully controlled. Shin [47] also mentions that even the called periodic signals generated by signal generators are not utterly periodic due to accuracy and noise. Therefore, in practice, it is arduous to get a genuinely periodic signal, and the most practical examples are in fact almost periodic signals. The almost periodic signal is that signal that looks like a periodic signal but if carefully analysed it is not. Both periodic and almost periodic can be investigated with Fourier series.

According to Shin [47], a transient signal can be generalised as a signal which has the following property $x(t) = 0$ when $t \to \pm\infty$. Thus, the transient signals are analysed using the Fourier transform [47, 49].

3.1.3 Non-deterministic signal

A non-deterministic signal is considered stationary when its statistical properties do not change under a shift of time, thus, its average and variance must be constant. Moreover, the probability of given points, for instance x_1 and x_2, at a certain time, t_1 and t_2, must be only a function of the time difference, $t_2 - t_1$, and does not depend of individual times, t_1 and t_2. Finally, the probability density function must be invariant under a shift of time. In case that a certain signal satisfies only the first two criteria, the signal is called stationary, and if it meets all criteria, it is called completely stationary. Otherwise the signal is considered non-stationary [47].

3.2 Signal processing

This section provides a brief review of the signal processing tools used in this work. The first subsection presents the main principles of the frequency analysis tool used. The second subsection introduces the Hilbert transform. The third subsection introduces concepts of digital filters.The fourth subsection briefly introduces the root mean squared (RMS) formula and usage. In order to keep this work organised, the Section 3.3 outlines the time-frequency tools used, and the Section 3.4 presents the correlation functions.

3.2.1 Fourier transform

In general, the concepts of frequency and amplitude can be understood intuitively by observing and analysing periodic motions and even periodic or almost periodic signals. In this context, one of the simplest and the most basic periodic function are the trigonometric functions sine and cosine. Despite being a trigonometric function, they are widely used to describe a dynamic system. These behaviours can be described by differential equations which have not only those trigonometric functions as a solution, but in some instances an additive composition of them [48, 47].

Thus, in the cases where the signal can be classified as periodic or almost periodic with a known function form, the Fourier Series can be used to analyse them. Once, the main Fourier Series characteristics are to represent a signal with an additive composition of sine and cosine functions of appropriate amplitudes, frequencies and phase. The Fourier series in its complex form is presented in Equation 3.1, where T is the period of the function, t is the time, n is a positive integer,

$$x(t) = \sum_{n=-\infty}^{+\infty} c_n \, e^{j2\pi nt/T} \quad \text{with} \quad c_n = \frac{1}{T} \int_0^T x(t) \, e^{-j2\pi nt/T} \, dt. \tag{3.1}$$

However, as mentioned by Figliola and Beasley [48], in the most practical measurements, the signals functional form is unknown. Therefore, despite being able to express any function as a composition of sine and cosine functions, its usage is limited when it comes to measured signal. Nevertheless, the Fourier analysis can be extended to non-periodic phenomena and thus, this expanded form can be used to decompose a generic signal into a composition of sine and cosine functions. The Fourier analysis is extended by changing the discrete summation, as shown in Equation 3.1, by a continuous summation, integral. This continuous summation is called Fourier integral or Fourier transform. It is given by

$$X(f) = \int_{-\infty}^{+\infty} x(t) \, e^{-j2\pi ft} \, dt \, , \tag{3.2}$$

and, its inverse form is given by

$$x(t) = \int_{-\infty}^{+\infty} X(f)\, e^{j2\pi ft}\, df, \tag{3.3}$$

where f is the frequency.

Despite the capability to analyse non-periodic signals with unknown functions, the Fourier transform is limited to continuous signals. Thus, there is an approximation to the Fourier transform for use on a discrete data, and it is called discrete Fourier transform (DFT). It is given by

$$Y(f_k) = \frac{2}{N} \sum_{r=0}^{N-1} y(r\delta t)\, e^{-j2\pi rk/N} \quad \text{with} \quad k = 0, 1, 2, \ldots, \left(\frac{N}{2} - 1\right), \tag{3.4}$$

$$f_k = k\delta f \quad \text{and} \quad \delta f = 1/N\delta t,$$

where the δt is the time discretisation, δf the frequency resolution and N the number of samples.

According to Figliola and Beasley [48], the DFT formula presented in Equation 3.4 is computationally expensive, where the computational cost increases at a rate that is proportional to N^2. Thus, this method is highly inefficient computationally and impracticable as the N increases. Then, a fast algorithm for computing the DFT was developed by Cooley and Tukey [50]. It is known as fast Fourier Transform (FFT).

3.2.2 Hilbert transform

Differently, from the Fourier transform the Hilbert transform does not change the signal domain. Thus the Hilbert transform of a time signal is another signal in time domain. A real and causal signal has unique relationships between its real and imaginary parts of the Fourier transform. These relationships is commonly known as Hilbert transform relationships [51, 52]. Hence, the Hilbert transform is defined as follows

$$H\{x(t)\} = \frac{1}{\pi} \int_{-\infty}^{+\infty} x(\tau) \frac{1}{t - \tau}\, d\tau, \tag{3.5}$$

where τ is the translation in time and t is the time. The Hilbert transform can also be expressed using the convolution notation, which is presented below

$$H\{x(t)\} = x(t) \ * \ \frac{1}{\pi\, t}. \tag{3.6}$$

The use of Hilbert transform enables the calculation of the analytical signal, which is a complex time signal whose the real part is the original signal and the imaginary part is the signal Hilbert transform [47]. Thus, the analytic signal is defined as

$$x_a(t) = x(t) + jH\{x(t)\}, \tag{3.7}$$

it can also be expressed as

$$x_a(t) = A_x(t)e^{j\phi_x(t)}, \tag{3.8}$$

where $A_x(t) = \sqrt{x^2(t) + H\{x(t)\}^2}$ and $\phi_x(t) = tan^{-1}(x(t)/H\{x(t)\})$.

As stated by Shin [47], in sound and vibration engineering, the Hilbert transform is commonly used to demodulate or modulate the signal amplitude and envelope analysis, where the demodulation refers to a technique that extracts the modulating components. The author also mentions that the envelope analysis can be used to early detect machine fault. In this case, the fault may generate a series of burst signals at regular interval. These burst signals decay rapidly and have relatively small energy. Therefore, the Fourier transform may be a proper tool to reveal the repetition frequency of bursts. Nonetheless, it may be possible to detect those frequencies components by analysing the signal envelope [47].

3.2.3 Digital filter

In general, filters are a specific and relevant class of linear time-invariant systems, where the term frequency-selective filter means that a system that passes only a specific set of frequencies components and entirely rejects all others. Thus, in a broader context, any system that modifies a specific frequency component can be considered a filter [51]. In the filter context, there are the digital filters that, according to Smith [53], are mainly used for two general purposes which are the separation of signals that have been combined and the restoration of a signal that has been distorted in some way.

The signal separation is required when a particular signal is contaminated with some interference, noise or other signals. The signal restoration is used when a signal has been distorted somehow [53]. Both digital and analog filters can be used for the tasks mentioned above. However, a digital filter can achieve a considerably better result. It is one of the main reasons why digital filters have become popular [53].

According to Smith [53], the Chebyshev filters can be used to separate one band of frequencies from another, and they are suitable for many applications. One of their main characteristics is their speed, which can be more than an order faster than other filters with higher performance such as the windowed-sinc filter. In this context, any filter that allows ripples in the frequency response of the stop band in order to enable a quick frequency roll-off is denominated the Chebyshev filter [53]. The filters with no ripple in the frequency response is a specific case of Chebyshev filter, and it is called maximally flat or Butterworth filter.

The Chebyshev filter design process consists mainly in determining four parameters, a high-pass or low-pass or even a high and low-pass response, the cutoff frequency or the cutoff frequencies, for the band-pass filter, the percent ripple in the passband and finally the number of poles or the filter order. In Butterworth filters, the ripple percentage is zero.

3.2.4 Root mean squared

As mentioned by Figliola and Beasley [48], the mean value of a dynamic signal does not provide any indication of the amount of variation. On the other hand, the root mean squared (RMS) of a signal in some cases can contain additional physical significance. For instance, in direct current (DC) the root mean squared can indicate if the signal contains no DC component or if the DC component has been subtracted from a particular signal. Moreover, the RMS value of a signal having a zero mean is a measurement of the magnitude of the signal fluctuations.

The RMS discrete formula is given as follows, where N is the number of samples and y_k, a point of a signal at the position k,

$$y_{RMS} = \sqrt{\frac{1}{N}\sum_{k=0}^{N-1} y_k^2}. \tag{3.9}$$

3.3 Time-frequency analisys

This section gives a brief review of the two time-frequency analysis tools used in this work, the short time Fourier transform (STFT) and Wavelet transform. Moreover, it mentions the primary motivations to use a time-frequency analysis instead of the standard frequency domain analysis.

Newland [54] mentions that one of the disadvantages of Fourier analysis is that the frequency information can only be extracted for the complete duration of a signal, once the Fourier integral extends from $-\infty$ to $+\infty$. Thus, the frequencies amplitudes are an average over the whole length of the signal. Also, if the signal has a temporary phenomenon that occurs at a specific point in time, it will contribute to Fourier transform calculation but the information of when it occurred will be lost.

The disadvantages of the Fourier transform analysis in determining localised frequency events can be overcome by decomposing the signal over elementary functions that are well concentrated in time and frequency. This decomposition in time and frequency is called time-frequency analysis. In this context, the short time Fourier transform and wavelet transform are two major classes of time-frequency decomposition [55, 54, 56]. However, the measurement of the frequency variation in time is affected by the uncertainty principle of Gabor [56].

According to MacLennan [57], Dennis Gabor is known as the father of holography, due to his development of its theory in 1947. However, in 1946, Gabor published his theory of communication, which served as a basis for representation and processing of information in vision and other sensory modalities. In his theory, Gabor was the first to realise that the uncertainty principle applies to information and signal processing [58]. Gabor proved his uncertainty principle by applying the same mathematical apparatus used in the Heisenberg derivation of the uncertainty principle in quantum mechanics, which is a consequence of the classical Cauchy-Schwartz inequality [57, 58].

According to MacLennan [57] and Mallat [56], the uncertainty principle of Gabor states that the energy spread of a function and its Fourier transform cannot be simultaneously arbitrarily small. In practical terms, it can be observed that the 'spread' of a signal and its Fourier transform are inversely proportional. Thus, the more spread the function is in time, the more defined it is in the frequency domain, and vice versa in Fourier transform. In the context of one dimension signal, the uncertainty principle can be noted as the Fourier transform relies upon an infinite superposition of nonlocal signals to represent a local signal. Hence, it depends on enormous cancellation to represent a local superposition [57]. In mathematical terms, the general Gabor uncertainty principle is given as

$$\Delta f \, \Delta t \geq 1. \tag{3.10}$$

where Δf is the error in measuring the frequency and Δt is the duration of the measurement [57].

According to Proakis [52], the energy of signal E can be defined as

$$E = \int_{-\infty}^{+\infty} |x(t)|^2 \, dt, \tag{3.11}$$

where $x(t)$ is the signal. The energy of a discrete signal $x(n)$ is defined as

$$E = \sum_{n=-\infty}^{\infty} |x(n)|^2. \tag{3.12}$$

Moreover, the energy of a signal can be finite or infinite. If E is finite, $x(t)$ is called energy signal. In case of infinite energy signals, Proakis [52] states that many signals that has infinite energy has a finite average power. The average power of a signal P is defined as

$$P = \lim_{T \to \infty} \frac{1}{2T} \int_{-T}^{T} |x(t)|^2 \, dt, \tag{3.13}$$

where $x(t)$ is the signal and T is the signal interval. The power of a discrete signal $x(n)$ is defined as

$$P = \lim_{N \to \infty} \frac{1}{2N+1} \sum_{-N}^{N} |x(n)|^2, \tag{3.14}$$

where N is the number of samples. If P of a signal is finite and nonzero, the signal is called power signal.

In the context of Fourier transform, according to Smith [53] the time and frequency domain representations of a signal are equivalent and must have the same energy. This relationship is called theorem of Parseval and it is expressed as

$$\int_{-\infty}^{+\infty} |x(t)|^2 \, dt = \frac{1}{2\pi} \int_{-\infty}^{+\infty} |X(f)|^2 \, df, \tag{3.15}$$

where f is the frequency and $X(f)$ denotes the Fourier transform of $x(t)$. Moreover, Mallat [56] states that there is no unique definition of time-frequency energy density.

Thus, with the Parseval theorem stated above and the energy and power of a signal defined in equations 3.11 and 3.13, it is possible to obtain the energy or power of each frequency. The spectrum of the energy of the frequencies is called energy spectral density (ESD), and the spectrum of the power of each frequency is called power spectrum (PS). Moreover, for non-deterministic stationary signals, the signal energy is defined as the power spectrum density (PSD), which is obtained similarly to the power spectrum, but the frequency resolution of Fourier Transform divides it.

3.3.1 Short time Fourier transform

The STFT is also called windowed Fourier transform. It was introduced in 1946 by Gabor in attempt to measure the 'frequency variation' of sounds. Then, Gabor showed that the time-frequency decomposition are closely related to the way we perceive sounds. Moreover, by using this decomposition, Gabor was able to detect import structures in speech and music recordings, where the time evolution of spectral components could be analysed. Thus, Gabor demonstrated the importance of time-frequency analysis [56]. The STFT is obtained by translating in time (τ) and frequency (f) a time window (g), the window function is given by

$$g_{\tau f}(t) = g(t - \tau) \, e^{-j \, 2\pi f \, t}. \tag{3.16}$$

Thus, the windowed Fourier transform defined by Gabor is given by

$$S(\tau, f) = \int_{-\infty}^{+\infty} x(t) \, g_{\tau,f}(t) \, dt = \int_{-\infty}^{+\infty} x(t) \, g(t - \tau) \, e^{-j2\pi f t} \, dt. \tag{3.17}$$

Mallat [56] mentions that the energy density of a STFT is called a spectogram and can be defined as

$$E(\tau, f) = |S(\tau, f)|^2. \tag{3.18}$$

The time and frequency resolutions of a STFT is directly related to the spread of the window in time and frequency which are defined by the user [56]. Thus, the STFT results can be significantly different according to the used window size used. The window size may affect the ability to identify a ephemeral phenomenon. Therefore, it is crucial to select a proper window size [55].

3.3.2 Wavelet transform

According to Gao and Yan [59], several individuals have contributed to advancing the state of research in wavelets, as it is called today. However, the major advancement in the field is attributed to Jean Morlet who, before the wavelet transform development, developed and implemented a technique of scaling and shifting a window when analysing acoustic echoes [59]. Morlet called the waveform resulting from stretching and squeezing a window function as 'Wavelet'. Thus, Morlet and Grossman, basing on Morlet previous analysis, developed the concept that a signal can be transformed into the form of a wavelet and then transformed back into its original form without information loss [59].

According to Newland [55], the wavelet transform provides a valuable method of generating time-frequency maps that allows the non-stationary and transient phenomena to be analysed and studied. The wavelet transform decomposes a signal into short waves which are called wavelet ($\psi(t)$). According to Torrence and Compo [60] and Newland [55], a function is 'admissible' as a wavelet when it has zero mean, it is localised both in time and frequency domain, and $\psi(t) \to 0$ when $t \to \pm\infty$, thus

$$\int_{-\infty}^{+\infty} \psi(t)\, dt = 0. \tag{3.19}$$

The wavelet coefficients are defined by the correlation function of a wavelet function ($\psi(t)$) translating in time (τ) and the signal being studied ($x(t)$). It is given as follows

$$a_{\psi}(t) = \int_{-\infty}^{+\infty} x(\tau)\psi(t-\tau)\, d\tau. \tag{3.20}$$

The a_{ψ} coefficient provides information of how the shape of the wavelet $\psi(t)$ correlates with the signal $x(t)$ in a certain time. Hence, when $x(t)$ correlates with $\psi(t)$, the a_{ψ} value will be large and otherwise it will be small [55, 56]. Thus, by stretching or scaling the wavelet function, it is possible to obtain more information about the signal. The wavelet function with a scale parameter s and translated by τ is given as

$$\psi_{\tau,s}(t) = \frac{1}{\sqrt{s}}\, \psi\left(\frac{t-\tau}{s}\right). \tag{3.21}$$

Finally, the wavelet transform of $x(t)$ at the scale s and position τ is given by

$$W(\tau, s) = \int_{-\infty}^{+\infty} x(t)\, \frac{1}{\sqrt{s}}\, \psi^*\left(\frac{t-\tau}{s}\right)\, dt, \tag{3.22}$$

where ψ^* denotes the complex conjugate of ψ.

A commonly used wavelet is the Morlet wavelet. It is composed by a sinusoidal wave multiplied by a Gaussian window. The Morlet wavelet $\psi_m(t)$ is given as

$$\psi_m(t) = c\, e^{-\sigma^2 t^2}\, e^{j2\pi\, f_0 t}, \tag{3.23}$$

where t is the time, c is a positive and constant parameter to ensure the admissibility of the wavelet. According to Nikolaou and Antoniadis [61], the c constant is typically chosen by

$$c = \frac{\sigma}{\sqrt{\pi}}. \tag{3.24}$$

Thus, the Fourier transform of the Morlet wavelet defined in Equation 3.23 with the constant c defined in Equation 3.24 is given as

$$\Psi(f) = \Psi^*(f) = e^{-(\pi^2/\sigma^2)(f-f_0)^2}. \tag{3.25}$$

The $\Psi^*(f)$ is the complex conjugate of $\Psi(f)$. As can be observed in Equation 3.25, the Morlet wavelet has the shape of a Gaussian window in the frequency domain, where f_0 is the central frequency, and σ determine the width. Thus, the parameter σ balances the width of the wavelet window in the time and frequency domain [61].

Similarly to the STFT, the local time-frequency energy density in the wavelet transform is given by

$$E(\tau, f) = |W(\tau, f)|^2. \tag{3.26}$$

3.4 Correlations

The correlation is a mathematical operation that resembles convolution. However, the objective to perform a correlation between two signals is to measure the degree of similarity between them and thus extract some desired information that depends on the application [52, 47]. The correlation function applied to the same signal is a specific case denoted as autocorrelation. Hence, it is possible to measure the degree of similarity of the signal at different times [47]. Proakis [52] mentions that the correlation of a signal is usually used in radar, sonar, digital communications and other areas of engineering.

The correlation of a discrete and real signal $x(n)$ and $y(n)$ is a sequence $r_{x,y}(l)$, which is defined by

$$r_{x,y}(l) = \sum_{-\infty}^{+\infty} x(n)\, y(n-l), \quad l = 0, \pm 1, \pm 2, \ldots, \tag{3.27}$$

and $x(n) = y(n)$ in the autocorrelation case. The term l is the time shift or lag parameter, and the order of subscripts x and y indicates the direction in which one signal is shifted. It is also possible to change this order, and thus the correlation can be defined as

$$r_{y,x} = \sum_{-\infty}^{+\infty} y(n)\, x(n-l), \quad l = 0, \pm 1, \pm 2, \ldots, \tag{3.28}$$

However, as stated by Proakis [52], comparing the equations 3.27 and 3.28 it is possible to conclude that

$$r_{x,y}(l) = r_{y,x}(-l). \tag{3.29}$$

3.4.1 Cross correlation

An important property of autocorrelation mentioned by Proakis [52] is that the autocorrelation of a signal attains its maximum value at zero lag. This result is coherent with the notion that a certain signal matches perfectly with itself at zero lag. Extending this interpretation to the cross-correlation, two different signals $x(n)$ and $y(n)$ delayed m samples one from the other, will have the maximum correlation coefficient when the delay (l) of the correlation matches with the signal delay. This property is applied to various practical problems in estimating time delay in a system [47].

Proakis [52] mentions that if any or both of the signals involved in the cross-correlation are scaled, the shape of the cross-correlation sequence will not change, only its amplitudes are scaled correspondingly. In certain applications, it may be desirable to normalize the cross-correlation sequence.

3.4.2 Pearson correlation

The variance (σ^2) of a random variable X with N values of a stochastic process with mean μ is given by

$$\sigma^2(X) = \frac{1}{N}\sum_{n=1}^{N}(X(n) - \mu)^2. \tag{3.30}$$

However, as mentioned by Shin [47] a simple generalization of the Equation 3.30 results in an equation that is similar to the autocorrelation function presented previously

$$C_{X,X}(l) = \frac{1}{N}\sum_{n=1}^{N}(X(n) - \mu)(X(n-l) - \mu), \tag{3.31}$$

where the l is a sample or time shift. The Equation 3.31 is called autocovariance function and the difference between the autocorrelation function is that the signal is subtracted by its mean. In the case that there are two random variables X and Y of a stochastic process, similarly to the cross-correlation, there is the cross-covariance which is given by

$$C_{X,Y}(l) = \frac{1}{N}\sum_{n=1}^{N}(X(n) - \mu_X)(Y(n-l) - \mu_Y). \tag{3.32}$$

In this context, there is the Pearson correlation (ρ) which is given by

$$\rho = \frac{C_{X,Y}(l)}{\sqrt{\sigma^2(X)\,\sigma^2(Y)}}, \tag{3.33}$$

where X and Y are random variables of a stochastic process.

3.5 Automatic multiscale-based peak detection

The peak detection is relatively straightforward in noise-free signals where their behaviour and characteristics are well defined. In most of those cases, the only use of the first and second derivative coupled with a manually tuned threshold is sufficient to detect the signal peaks with reasonable accuracy. However, in most practical applications and signal processing, it is required to identify peaks in signals which are noisy with fluctuations that do not necessarily correspond to the desired phenomenon. A vast number of algorithms using different approaches and techniques were developed to address challenges that the practical applications have.

As mentioned by Scholkmann, Boss and Wolf [62], a crucial issue of the peak detection algorithms available is that the more widely applicable, the more free parameters have to be set to be used. On the other hand, the algorithms with lower free parameters are application specific. Besides, the noise in the signals is a challenging case for many peak detection algorithms available [62]. Thus, Scholkmann, Boss and Wolf [62] developed an algorithm based on a multiscale technique to detect peaks in noisy periodic or quasi-periodic signals. It does not have any free parameters. The authors called it automatic multiscale-based peak detection (AMPD).

The AMPD algorithm has 9 steps. Considering a discrete signal $x(n)$ of length N and $L = \lceil N/2 \rceil - 1$, where $\lceil y \rceil$ means the nearest integer greater than y, the steps are

1. Detrend the signal;
2. Generate a random matrix $\mathbf{M} \in \mathbb{R}^{L \times N}$;
3. Set a window of length k, which is given by $w_k = 2k \quad \text{where} \quad k = 1, 2, 3, \ldots, L$;
4. The matrix elements are update as follows

$$m_{k,i} = \begin{cases} 0, & x_{i-1} > x_{i-k-1} \quad and \quad x_{i-1} > x_{i+k-1} \\ m_{k,i}, & \text{otherwise} \end{cases} \tag{3.34}$$

$$\text{where} \quad i = k+2, \ldots, N-k+1 \ ;$$

5. Perform a row-wise summation

$$g_k = \sum_{i=1}^{L} m_{k,i} \ ; \tag{3.35}$$

6. Return to the step 3 until $k = L$;

7. Get the position of lowest element of g, λ;

8. Calculates the column wise standard deviation as follows

$$\sigma_i = \frac{1}{\lambda}\sum_{k=1}^{\lambda}\left[\left(m_{k,i} - \frac{1}{\lambda}\sum_{k=1}^{\lambda} m_{k,i}\right)^2\right]^{\frac{1}{2}}, \quad \text{where} \quad i = 1, 2, 3, \ldots, N \; ; \tag{3.36}$$

9. Finally, the peaks are where $\sigma = 0$.

3.6 Two-phase flow

3.6.1 General aspects of two-phase flows

As mentioned by Shoham [2], the hydrodynamics of single-phase flow in pipes is well understood nowadays. The heat transfer process and the relationships between the pressure drop and flow rate for single-flow pipelines can be determined straightforwardly. However, the addition of a phase to the flow in the pipe increases the flow complexity dramatically, and the relationships and process mentioned before are no longer straightforward and well understood. Then, the flow is considered a two-phase flow. The two-phase flows, for instance, can be comprised of liquid-solid, liquid-gas, liquid-liquid, and solid-gas. In this work the two-phase flow considered is the liquid-gas two-phase flow in pipes.

Shoham [2] states that the main difference between single-phase and liquid-gas two-phase flow is the presence of flow patterns or flow regimes. In this case, the flow pattern refers to a geometrical distribution of each phase in the pipe, that the liquid and gas flowing simultaneously in a pipe can arrange themselves. The phases arrangement can be in a much different manner along the pipe that the phases interfaces differ enormously. It results in utterly different flow characteristics, such as phases velocities and percentage of the phases in a specific section of the pipe. Thus, to characterise them, it is required a large number of flow variables which, according to Shoham [2], almost the double when compared with the single-phase flow.

The increase of the flow complexity is particularly substantial for liquid-gas flows, where the compression of the gas phase is significant. Shoham [2] mentions that in those systems, the experimental, numerical simulation and exact solution approaches are either impractical or too complicated. In this context, according to Shoham [2], the flow pattern determination is crucial in two-phase flow analysis. Once, all the process variables of the developed models of the two-phase flows are strongly dependent on the current flow pattern.

Most of the developed models does not comprehend all flow patterns of the liquid-gas flows. However, two-phase models range from analytical to experimental approaches. They have reasonable accuracy but for a limited or a broad set of pipe configurations and a specific flow pattern. Moreover, Shoham [2] states that in the past there was no consensus about the

flow patterns, due to the phenomenon complexity and visual determination of the flow pattern. Nevertheless, the current trend is to define a minimal, but meaningful, set of flow patterns.

3.6.2 Flow patterns and their main characteristics

As this work focuses on upward liquid-gas two-phase flows, a discussion of other two-phase flow pattern falls outside the scope of this work. Thus, this section will give only an overview of liquid-gas flow patterns, where the upward vertical and sharply inclined flow will be emphasised. Therefore, throughout this work, the use of the term 'flow pattern' will refer to two-phase liquid-gas flow pattern and 'two-phase' flow refer to two-phase liquid-gas flow.

A specific flow pattern condition is bounded to a set of system variables such as operational parameters, gas and liquid flow rates; geometric variables, pipe inclination angle and diameter; the presence of any upstream or pipework such as bend, valves, T-junctions; physical properties, gas and liquid densities, viscosities and surface tension. On the other hand, the design variables such as pressure drop, liquid holdup[1], heat and mass transfer coefficients have a strong dependence on the existing flow pattern. Moreover, the flow patterns are usually defined for either one inclination or a narrow range of inclination angles [2, 1].

The vertical and near-vertical flow has five flow patterns. In this case, the flow patterns are more symmetrical around the pipe axis and less dominated by gravity. Thus, the flow patterns are bubble flow, slug flow, churn flow, annular flow and dispersed bubble flow [2].

Low liquid rates characterise the bubble flow. The gas-phase is dispersed into small discrete bubbles that move upward in a zigzag motion in a liquid phase. The bubbles distribution is approximately homogeneous throughout the pipe cross-section. One of its characteristics is the slippage between the gas and liquid phase which results in large values of liquid holdup [2].

The alternate flow of liquid and gas characterises the slug flow. The called slugs of liquid fill the entire pipe cross section area and separate the bullet shape gas pockets called 'Taylor bubble'. The 'Taylor bubble' has an almost equal diameter of the pipe and between it and the pipe, there is a thin downward liquid layer. At the end the of 'Taylor bubble' the liquid film penetrates into the following liquid slug creating a mixing zone aerated by small gas bubbles. The flow in slug flow regime consists of successive liquid slugs and 'Taylor bubbles' [2]. Moreover, Rodrigues and Morales [63] mentions that in the slug flows, flow structures repeat randomly in space and time.

The oscillatory motion of the liquid-phase characterises the churn flow. It is similar to the slug flow but with no clear boundaries between the two phases. It occurs at higher gas flow rates, where the liquid slugs become shorter and frothy. The gas phase blows the liquid slugs, which breaks falling downwards and merging with the next liquid slug. Consequently, the 'Taylor bubble' gets more distorted and the churning occurs [2].

The annular flow occurs at very high gas flow rates. One of its main characteristics is that the gas-phase flows in a core of high velocity, which may contain entrained liquid droplets. On

[1]The amount of liquid, in percentage, in a given cross-section.

the other hand, the liquid flows slowly around the pipe wall. As a result of the high-velocity difference between the phases and therefore, high interfacial shear stress, the annular flow has wavy interfacial structure. The liquid film thickness around the pipe wall is approximately constant [2].

The dispersed-bubble flow occurs in high liquid flow rates where the gas phase is dispersed in the liquid phase as small bubbles. In this flow pattern, the liquid phase carries the gas bubbles, and therefore, there is no slippage between the phases [2].

The Figure 3.1 illustrates the flow patterns of vertical and near vertical pipes [2].

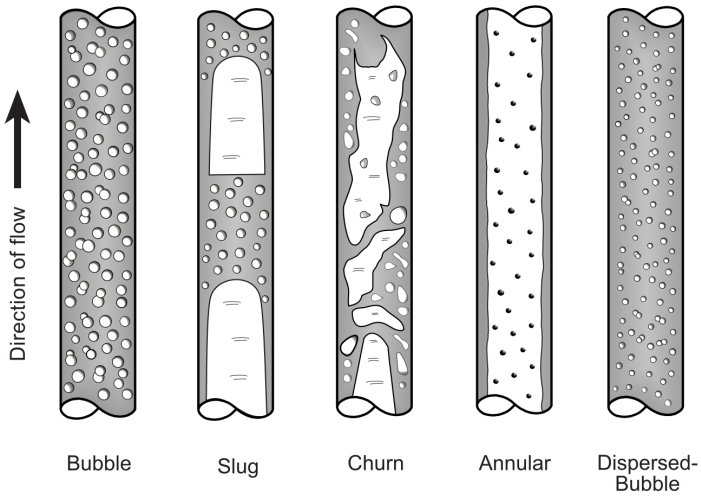

Figure 3.1: Flow patterns in vertical and near vertical pipes [2].

3.6.3 General two-phase flow properties

This section briefly outlines the main two-phase flow variables and properties that will be used in this work.

The mass flow in $\mathrm{kg\,s^{-1}}$ are defined as

$$\begin{aligned} &W_L = \text{liquid mass flow rate,} \\ &W_G = \text{gas mass flow rate,} \\ &W = \text{total mass flow rate} \quad \text{where} \quad W = W_L + W_G. \end{aligned} \tag{3.37}$$

The volumetric flow in $\mathrm{m^3\,s^{-1}}$ are defined as

$$\begin{aligned} &q_L = \text{liquid volumetric flow rate,} \\ &q_G = \text{gas volumetric flow rate,} \\ &q = \text{total volumetric flow rate} \quad \text{where} \quad q = q_L + q_G. \end{aligned} \tag{3.38}$$

The fraction of volume element occupied by the gas-phase is called gas void fraction (GVF) and it is represented by α and it is dimensionless. On the other hand, the volume element occupied by the liquid-phase is called liquid holdup and it is represented by H_L.

The phase volumetric flow rate per unit area is called superficial velocity. It is the velocity if only a phase of the flow was flowing alone in the pipe [2]. The superficial velocities are defined in $\mathrm{m\,s^{-1}}$ as

$$v_{SL} = \frac{q_L}{A_p} \quad \text{and} \quad v_{SG} = \frac{q_G}{A_p}, \tag{3.39}$$

where A_P is area of the pipe cross-section and the subscripts L and G refers to the liquid and gas phase respectively.

The total volumetric flow rate per unit area is called mixture velocity and it is defined in $\mathrm{m\,s^{-1}}$ as

$$v_M = \frac{q_L + q_G}{A_p} = v_{SL} + v_{SG}. \tag{3.40}$$

As each phase occupies a different portion of the pipe cross-section, the actual velocities of each phase are defined in $\mathrm{m\,s^{-1}}$ as

$$v_L = \frac{v_{SL}}{1-\alpha}, \quad \text{and} \quad v_G = \frac{v_{SG}}{\alpha}, \tag{3.41}$$

where α is the GVF.

The two-phase flow properties can be expressed as a weighted average of the phase properties where the weight is the GVF. Thus, considering ρ as the specific mass and μ the viscosity, they are given as

$$\begin{aligned} \rho_M &= \rho_L(1-\alpha) + \rho_G\alpha, \\ \mu_M &= \mu_L(1-\alpha) + \mu_G\alpha. \end{aligned} \tag{3.42}$$

The Reynolds number using the homogeneous non-slip model, where d is the pipe diameter, can be expressed as

$$Re_M = \frac{\rho_M v_M d}{\mu_M}. \tag{3.43}$$

3.6.4 Slug flow specific properties

Rodrigues and Morales [63] states that the first study in slug flows was the work of Wallis [64]. The author developed a model that considers a periodical development of a unit cell through the pipe. Next, Dukler and Hubbard [65] and Taitel and Barnea [66] developed predictive models based on the flow hydrodynamics. These models only predict the slug unit cell characteristics,

and then they generalise to the pipe [63]. Rodrigues and Morales [63] mention that those models ignore the flow intermittency and are called steady-state models. Furthermore, those models have more unknown variables than equations, and they require closure relationships that are usually obtained experimentally [63].

As described before, the slug flow is characterised by alternate flow of liquid and gas, where the slug of liquid fills the entire pipe cross section area and separates the bullet shape gas pockets called 'Taylor bubble'. In this context, the Figure 3.2 shows a schematic description of the current physical model for slug flow. It shows a slug unit with the total length of L_v that contains two main regions called liquid slug body, L_S, and the 'Taylor bubble' behind the slug, L_F.

Circling the 'Taylor bubble', there is a liquid film of h_{Fe} thickness. It has a velocity that decreases from its maximum (V_{LTB}), at the front of the 'Taylor bubble', to its minimum (V_{LTBe}), at the beginning of the liquid slug body. The 'Taylor bubble' has a translational velocity (V_{TB}), which is the interface velocity, and the gas velocity inside it, V_{GTB}. Finally, the liquid and gas velocities inside the liquid slug body are the V_{LLS} and V_{GLS} respectively. Shoham [2] sates that in general the velocity distribution is $V_{TB} > V_{GTB} > V_{GLS} > V_{LLS} > V_{LTB}$.

Furthermore, as can be observed in Figure 3.2, the two main regions of the slug flow can have considerably different GVF. In the liquid slug body, there is gas entrained in the form of small bubbles, while the 'Taylor bubble' has a large gas pocket. Therefore, the liquid holdup is H_{LLS} and H_{LTB} for the liquid slug body and 'Taylor bubble' respectively.

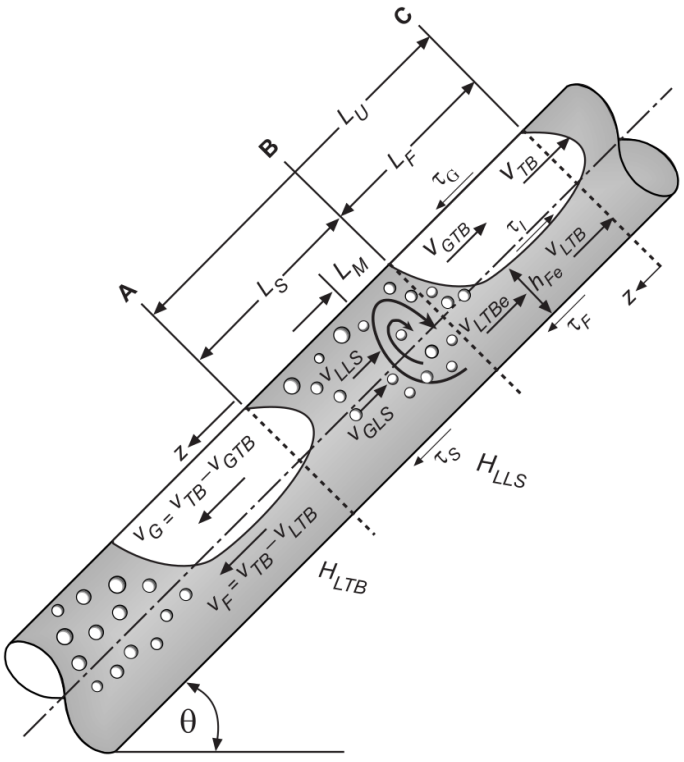

Figure 3.2: Physical model for slug flow [2].

3.6.5 Closure relationships

According to Shoham [2], the Dukler and Hubbard [65] model requires two closure relationships, the liquid holdup in the slug body, H_{LLS}, and the slug frequency, v_s. On the other hand, Taitel and Barnea [66] model requires not only the H_{LLS} and the v_s, or the liquid slug body, L_S , but also the translational velocity of the 'Taylor bubble', V_{TB}, and the velocity of the small bubbles in the liquid slug, V_{GLS}.

Translational velocity

Rodrigues and Morales [63] state that the Nicklin, Wilkes and Davidson [67] were the first to study the 'Taylor bubble', or elongated bubble, motion within a flowing liquid. Nicklin, Wilkes and Davidson [67] calculated the bubble velocity as a linear superposition of the velocity of the elongated bubble in stagnant liquid with the influence of the moving liquid. Thus, they proposed the following model

$$V_{TB} = C_0 v_m + C_1 \sqrt{g\, d}, \tag{3.44}$$

where C_0 is a constant that measures the influence of mixture velocity in an elongated bubble, C_1 is a constant to evaluate the drift velocity and g is the gravity. Therefore, the drift velocity can be obtained by

$$v_D = C_1 \sqrt{g\, d}. \tag{3.45}$$

Rodrigues and Morales [63] mention that in early studies with one bubble rising in stagnant liquid the value of C_1 proposed was 0.328. Next, through experiments in vertical turbulent flow Nicklin, Wilkes and Davidson [67] established the value of C_1 as 0.351 and the C_0 value as 1.2. Besides, since the work of Nicklin, Wilkes and Davidson [67] the C_0 is considered a function of the mixture Reynolds number, the Froude number and Eötvös number.

After Nicklin, Wilkes and Davidson [67] work, different authors proposed correlations to obtain the 'Taylor bubble' velocity, some only valid for horizontal flow and others for horizontal and vertical flow. These studies focus on obtaining a more accurate value of the C_0 and C_1 constant by taking into account the effects of the mixture Reynolds number, Froude number and the pipe inclination. Moreover, Rodrigues and Morales [63] did a comparative study of the accuracy of the closure relationships, which includes the correlations to obtain the C_0 and C_1.

As this work is focused on vertical flow, only the models for vertical flow were considered. After Nicklin, Wilkes and Davidson [67], Bendiksen [68] proposed the following model to obtain C_0 and C_1

$$C_0 = \begin{cases} 1.05 + 0.15\, sin(\theta)^2 & \text{if } Fr_l < 3.5, \\ 1.2 & \text{if } Fr_l \geq 3.5, \end{cases} \tag{3.46}$$

$$C_1 = \begin{cases} 0.54\,sin(\theta) + 0.35\,sin(\theta) & \text{if } Fr_l < 3.5, \\ 0.35\,sin(\theta) & \text{if } Fr_l \geq 3.5, \end{cases}$$

where θ is the pipe inclination angle and Fr_l is given by

$$Fr_l = \frac{v_{sl}}{\sqrt{g\,d}}. \tag{3.47}$$

Later, Dukler, Moalem Maron and Brauner [69] proposed that the value of C_0 should be 1.225 for horizontal and vertical flows. Then, Théron [70] proposed the following model

$$C_0 = 1.3 - \frac{0.23}{\Gamma} + 0.13\,sin(\theta)^2, \tag{3.48}$$

$$C_1 = \left(-0.5 + \frac{0.8}{\Gamma}\right)\,cos(\theta) + 0.35\,sin(\theta),$$

where Γ is given by

$$\Gamma = 1 + \frac{Fr_l}{Fr_{crit}}\,cos(\theta) \quad \text{where} \quad Fr_{crit} = 3.5. \tag{3.49}$$

Finally, there is the model proposed by Petalas and Aziz [71] that is given by

$$C_0 = \frac{1.64 + 0.12\,sin(\theta)}{Re_M}. \tag{3.50}$$

As mentioned above, Rodrigues and Morales [63] did a comparative study of the accuracy of the closure relationships. They considered different gases, liquids, pipe diameters and viscosities. They found that the majority of the models have relative errors of $\pm 20\,\%$. Moreover, they stated that Dukler and Hubbard [65] model has high errors for high viscosities. Besides, they found that the Bendiksen [68] correlation error decreases when the viscosity increases.

Slug frequency

According to Rodrigues and Morales [63], the slug frequency is defined as the reciprocal of the time taken by a 'Taylor bubble' to travel a unit cell distance. Therefore, it is given by

$$v_s = \frac{V_{TB}}{L_F + L_S}. \tag{3.51}$$

Rodrigues and Morales [63] state that there are many models to predict the slug frequency. They are usually a function of flow parameters such as superficial gas and liquid velocities, or they can be a function of geometric parameters and fluid properties. However, most of the models are based on experimental data [2, 63]. Moreover, Shoham [2] stated that a mechanistic model to predict the slug frequency was developed, but it is complex and requires a numerical solution of an unsteady-state conservation equation of mass and momentum by finite difference scheme, which is expensive computationally.

Despite the different models presented by Rodrigues and Morales [63] and Shoham [2] to obtain the slug frequency, those models are all for horizontal flow. As this work is focused on vertical flows, it was researched for slug frequency correlations for vertical flow, and it was not found. Nevertheless, it was found a study of the characteristics of slug flow in a vertical riser [72].

Abdulkadir *et al.* [72] presented the results of a series of experiments on a vertical riser of $67\,\mathrm{mm}$ of an air-silicone slug flow with different superficial velocities. The study was conducted using an electrical capacitance tomography. Abdulkadir *et al.* [72] found that the slug frequency increase with the increase of the liquid superficial velocity. Furthermore, the authors mentioned that for lower liquid superficial velocities, the slug frequency slightly increased with the increase of the gas superficial velocity. Besides, they found that at the higher liquid superficial velocities, the slug frequency slightly decreased and then increased when the gas superficial velocity was increased.

4 Experimental apparatus and tests procedures

This chapter describes the experimental apparatus used to perform the experiments together with the tests procedures. Thereunto, this chapter is divided into seven sections. The first section gives an overview of the experimental assembly. The second section presents details of the process variable instrumentation used. The third section details the vibration instrumentation and the criteria used to place them. The fourth section outlines the visualisation apparatus. The fifth section details the data acquisition system and the supervisory program developed. The sixth section gives an overview of the experimental procedure used. Finally, the last section outlines the procedure used to define the test matrix.

4.1 Experimental assembly

This section describes the experimental assembly and its main components. Despite mentioning the instrumentation used, they will be detailed in the Section 4.2.

The experimental apparatus required to perform the proposed vibration analysis was assembled in the Experimental Laboratory of Petroleum Kelsen Valente Serra (LABPETRO) at the Centre for Petroleum Studies (CEPETRO), which is located at the University of Campinas. The experimental apparatus piping and pump were already mounted from a previous work. Thus, to meet this work requirements it was performed a few adaptations on it. The fast-closing system was adjusted and the new instrumentation mounting, wiring, calibration and the experimental apparatus commissioning were performed as part of this work. The Figure 4.1 presents the experimental apparatus schematics.

As can be seen in the Figure 4.1, the experimental assembly comprises of three distinct flow lines, a liquid, a gas and a two-phase. They have diameters of approximately $77.9\,\mathrm{mm}$, $12.5\,\mathrm{mm}$ and $52.5\,\mathrm{mm}$ respectively. The liquid and two-phase lines are *SCH-40* pipes. The liquid line starts at the separator tank of $1.5\,\mathrm{m}^3$ placed on the top of the LABPETRO building. Then, a pump placed on the ground floor, approximately $13.4\,\mathrm{m}$ below the tank, pumps the liquid. Also, on the ground floor, there is an air supply which feeds the experimental assembly gas line. Finally, the gas is injected into the flow through a nozzle. Thus, downstream of the nozzle, the flow becomes two-phase, and it is where the two-phase flow line starts.

As shown in the Figure 4.1, the liquid line starts at the separator tank. Then, the liquid goes to a progressive cavity pump driven by a three-phase AC motor controlled by a variable-frequency drive (*SY-101*). Next, the liquid can pass or not through a bypass line, controlled by a manual globe valve. The bypass line connects the pump outlet to its inlet. Then, the liquid pass through a Coriolis mass flowmeter (*FT-101*). Finally, the liquid arrives at the two-phase flow line. The

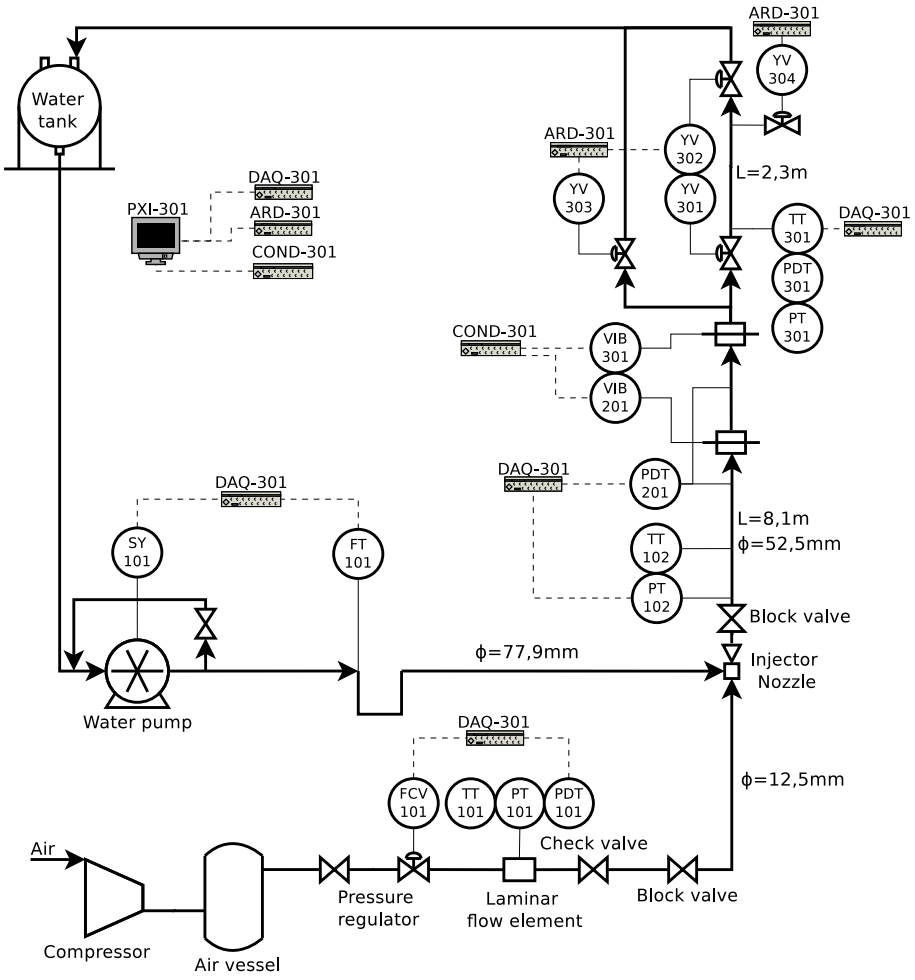

Figure 4.1: Experimental assembly schematics assembled at LABPETRO.

Figure 4.2 shows liquid line and Figure 4.3 shows the separator tank.

The pumping setup can achieve mass flow from $17.5\,\mathrm{kg/min}$ up to $325\,\mathrm{kg/min}$. However, due to the bypass line, lower mass flow rates can be obtained by adjusting the bypass line valve. The Table 4.1 presents the details of the equipment mentioned above.

Table 4.1: Liquid line components.

Name	Component	Manufacturer	Characteristics
	Motor	WEG	Three phase AC 220/380/440 V; 59.8/34.6/29.9 A; 18.5 HP; 1165 RPM
SY-101	Variable-frequency drive	WEG	Model CFW090030T; Three phase AC 380/480 V
	Cavity pump	Netzsch	Model NM053; $10\,\mathrm{m^3\,h}$ to $21\,\mathrm{m^3\,h}$
FT-101	Coriolis flow-meter	Metroval	Model RHM40 - 3FS1PN

As mentioned previously, the gas line is feed by an air supply. In a simplified way, shown in Figure 4.1, the air supply consists of an air compressor that feeds a compressed air vessel which

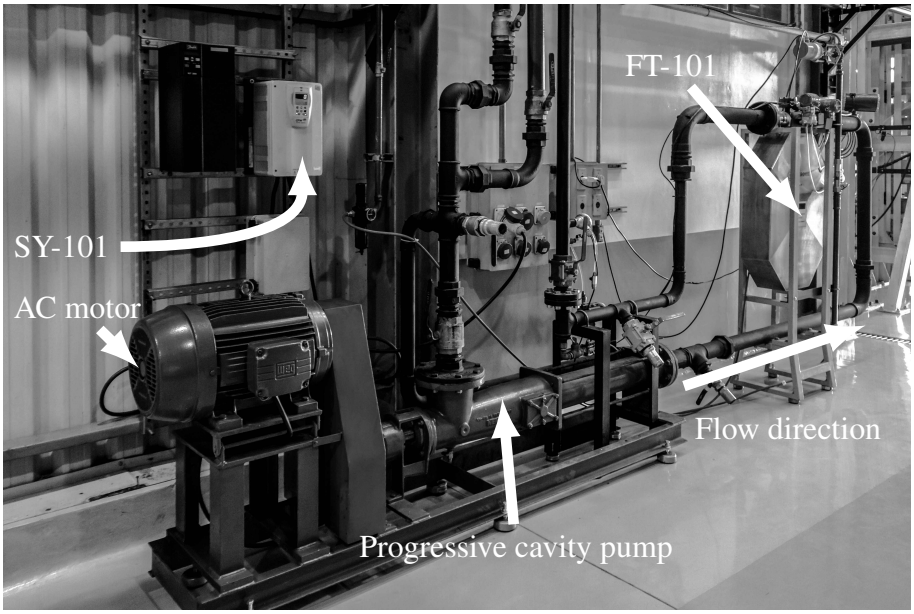

Figure 4.2: Assembled liquid line.

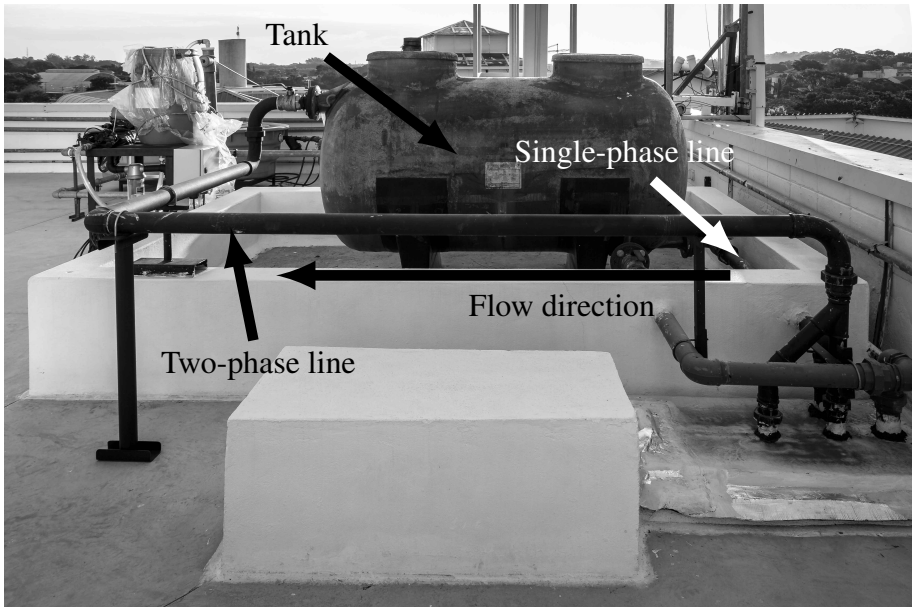

Figure 4.3: Separator tank.

feeds the gas line. Thus, with the air supply, the gas line starts with a manual pressure regulator valve. It regulates the gas line pressure to be a pre-set, being able to keep the gas line pressure constant despite small pressure fluctuations of the air supply. Then, the gas passes through a flow control valve (*FCV-101*) used to control the gas flow in the gas line remotely.

Next, the gas passes through a laminar flow element. It is composed of a temperature transmitter (*TT-101*), a pressure transmitter (*PT-101*) and a differential pressure transmitter (*PDT-101*). Therefore, it is possible to calculate the mass flow. Next, the gas passes through a check valve and then through a block valve.

Finally, the gas is injected through a nozzle in the two-phase line. The nozzle was machined

in brass. It has an internal diameter of $14\,\mathrm{mm}$ and with a length of $150\,\mathrm{mm}$. It contains six columns with 15 holes with a diameter of $2\,\mathrm{mm}$ each. The Table 4.2 presents the details of the gas line apparatus. The 'X' in the component name means that the specifications are also valid for the others instruments. The Figure 4.4 presents the gas flow line.

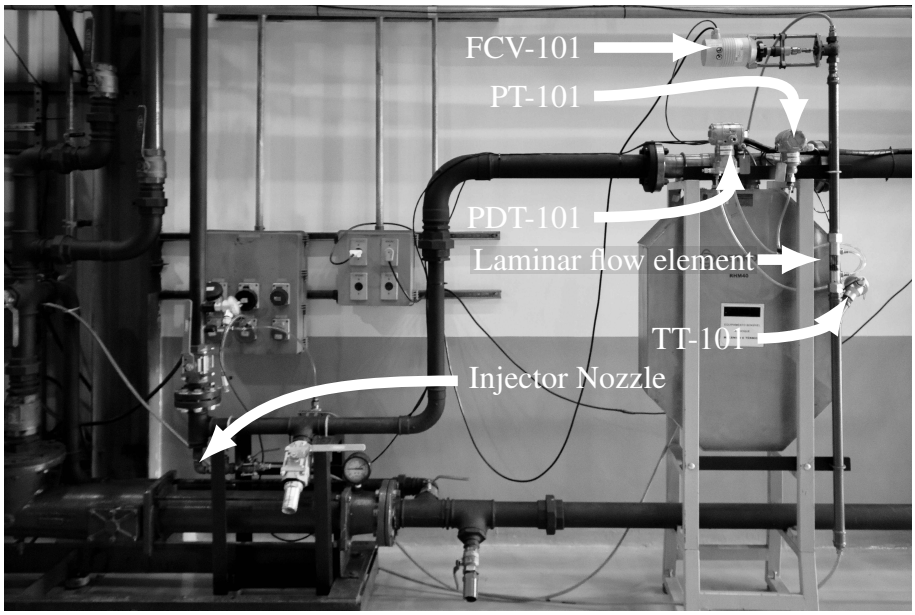

Figure 4.4: Assembled gas line.

Table 4.2: Gas and two-phase line components.

Name	Component	Manufacturer	Characteristics
	Compressor	Ingersoll-Rand	Model SSR-HP50 SE; operational pressure $9.6\,\mathrm{bar}$; capacity $348.3\,\mathrm{m^3\,h^{-1}}$
	Laminar flow element	Meriam	Model 50MW20
FCV-101	Gas valve	Hora	Model BR225RGA; actuating time $6\,\mathrm{s\,mm^{-1}}$; power supply $230\,\mathrm{V}$; input signal $4\,\mathrm{mA}$ to $20\,\mathrm{mA}$
PT-10X	Pressure transmitter	Rosemount	Model 2051TG3A2B21AQA
PDT-101	Differential pressure transmitter	Rosemount	Model 2051CD1A22A1AQA

Downstream of the nozzle, just after the mixture point, it was installed a temperature and pressure transmitter, *TT-102* and *PT-102* respectively. Then, the first vibration measurement station (*VIB-201*) was placed after $7\,\mathrm{m}$ from the mixture point. Thus, it has a length-diameter ratio of 127 while Hewitt, Delhaye and Zuber [73] recommends the ratio of straight pipe length with its diameter of at least 120, to ensure that the two-phase flow is fully developed. Subsequently, a second vibration measurement station (*VIB-301*) was placed $1.5\,\mathrm{m}$ from the first station.

After the second vibration measurement station (*VIB-301*), it was placed a fast-closing system made up of three pneumatic valves and a solenoid valve, between two pneumatic valves there is a $2.3\,\mathrm{m}$ of straight pipe. This system is responsible to perform an independent gas void fraction (GVF) measurement. It is capable to measure GVF from $6.2\,\%$ to $93.8\,\%$. Moreover, the fast-closing system was automated by controlling the pneumatic and solenoid valves with relays, which are controlled by an open-source electronics platform known as Arduino (*ARD-301*). Thus, it establishes serial communication with the supervisory program which sends the control signals.

Furthermore, the fast-closing system incorporates a temperature and a pressure transmitter, *TT-301* and *PT-301* respectively. They are used to estimate the flow properties next to the second vibration station (*VIB-301*). The pressure transmitter *PT-301* is also used to estimate the height of liquid trapped in the fast-closing system. Thus, knowing the height of liquid, it is possible to calculate the GVF. Moreover, it was mounted a visualisation section in the fast-closing system to enable the flow visualisation and consequently the flow filming. It was placed approximately $1.4\,\mathrm{m}$ after the first pneumatic valve of the fast-closing system.

Finally, after the fast-closing system, the two-phase flow goes to the separator tank, where the gas is separated from the liquid. The Figure 4.5 shows two-phase line and the Figure 4.6 presents the fast-closing system.

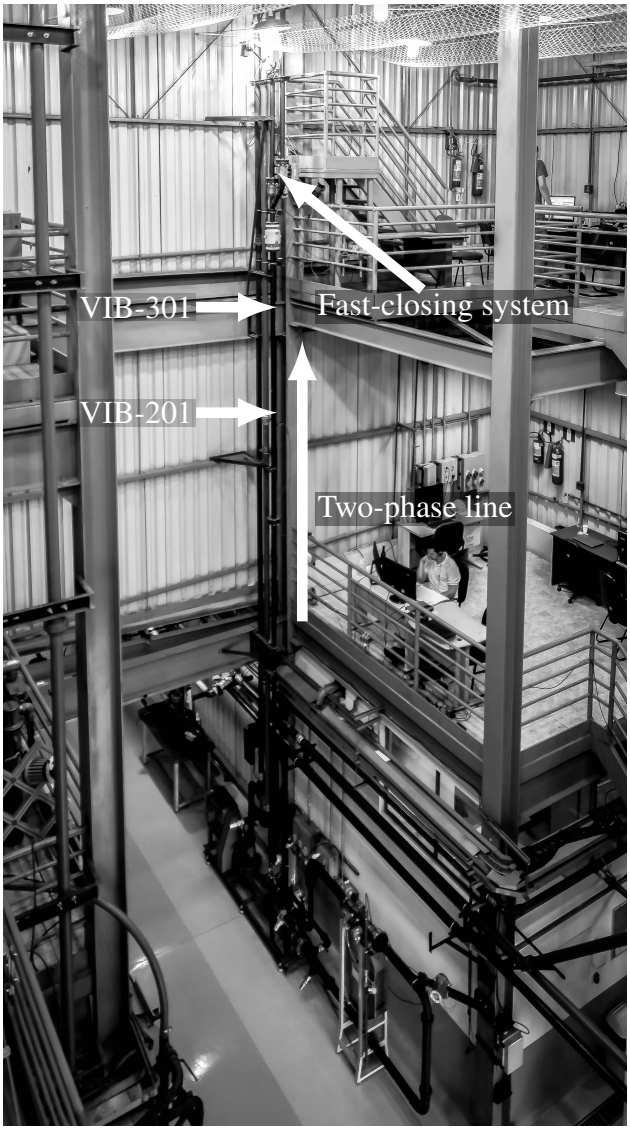

Figure 4.5: Assembled two-phase line.

Figure 4.6: Fast-closing system.

4.2 General instrumentation

The Section 4.1 described the three distinct lines with their instrumentation that composes the experimental assembly. In addition, it was mentioned the purpose of them but without specifying the instrumentation. This section focuses on listing the variables that the experimental assembly is capable to measure and the process variables instrumentation specifications.

The processes variables measured were acquired with a sample rate of $10\,\mathrm{kHz}$. This sample rate is Nyquist frequency of the highest frequency of the frequency range of the instrumentation used. Despite the sample rate be the Nyquist frequency of the highest frequency of the instrumentation, the process variables were used to calculate the flow average properties of the acquisition. Finally, the instrumentation specifications are shown in Table 4.3. The 'X' in the components name means that the specifications are also valid for the others instruments.

Table 4.3: Instrumentation specifications.

Name	Component	Range	Accuracy	Output
FT-101	Liquid flowmeter	90 to $900\,\mathrm{kg/min}$	$\pm 0.5\,\%$	4 to $20\,\mathrm{mA}$
PT-10X	Pressure transmitter	0 to $1000\,\mathrm{kPa}$	$\pm 0.065\,\%$	4 to $20\,\mathrm{mA}$
PT-301	Pressure transmitter	0.1 to $48\,\mathrm{kPa}$	$\pm 0.04\,\%$	4 to $20\,\mathrm{mA}$
TT-X0X	Temperature transmitter (PT-100)	-50 to $200\,^{\circ}\mathrm{C}$	$\pm 0.05\,^{\circ}\mathrm{C}$	4 to $20\,\mathrm{mA}$
PDT-101	Differential pressure transmitter	0 to $2\,\mathrm{kPa}$	$\pm 0.065\,\%$	4 to $20\,\mathrm{mA}$

4.3 Vibration instrumentation

The Section 4.1 outlined the vibration measurement by mentioning that two vibration measurement stations were used (*VIB-201* and *VIB-301*). The vibration measurement station is composed of two uniaxial accelerometers. Thus, in total it was used four accelerometers. They require that their signal must be conditioned to generate signals that are detectable by the analog-to-digital converter used. Thus, it was used a signal conditioner (*COND-301*) model *482A05* from the manufacturer *PCB*. It conditions up to four accelerometers at once. The signals acquired were stored and post-processed in a different computer using the programming language *Python*. A simplified version of the *Python* codes used can be found in Appendix A. The schematics of the vibration measurement is presented in Figure 4.7.

All the four transducers used are uniaxial accelerometers model *PCB 35368* from the same manufacturer of the signal conditioner. They have a nominal sensitivity of $100\,\mathrm{mV\,g^{-1}}$ and a frequency range of $2\,\mathrm{Hz}$ to $10\,000\,\mathrm{Hz}$. Thus, the sample rate employed was $60\,\mathrm{kHz}$, which is three times higher than the Nyquist frequency of the highest frequency from the transducers

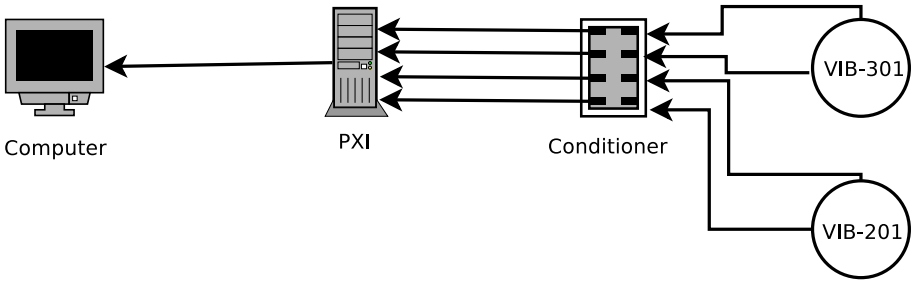

Figure 4.7: Vibration measurement schematics.

frequency range. The transducers sensitivity and uncertainty from the manufacturer calibration are presented in Table 4.4.

The transducers were placed perpendicular to each other concerning the pipe centre as shown in Figure 4.9 and Figure 4.8, in order to measure the pipe lateral vibration. The first digit of the transducer name refers to the vibration measurement station, where the 0 means the *VIB-201* and the 1 means the *VIB-301*. The second digit means the angle. Finally, The analog-to-digital converter used will be more detailed in Section 4.5.

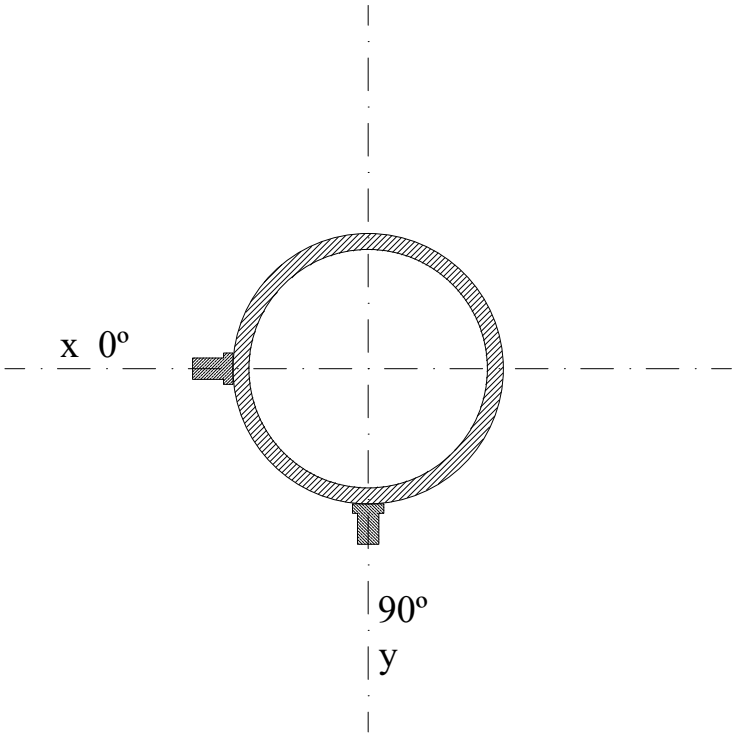

Figure 4.8: Accelerometers positioning.

One of the criteria used to position the vibration measurement stations was to place one of them as close as possible to the fast-closing system. Once, it has a set of instrumentation that is capable of determining a set of flow properties. A second criterion was that the flow must be fully developed according to Hewitt, Delhaye and Zuber [73] criterion. Another criterion was that the stations must be placed in a different structural condition of the pipe, for instance near

Figure 4.9: Accelerometers positioning.

Table 4.4: Accelerometers specifications.

Name	Manufacturer	Model	Frequency range	Voltage Sensitivity
0-0	PCB	353B68	2 to 10 000 Hz	$97.9\,\mathrm{mV/g}$
0-90	PCB	353B68	2 to 10 000 Hz	$97.4\,\mathrm{mV/g}$
1-0	PCB	353B68	2 to 10 000 Hz	$103.7\,\mathrm{mV/g}$
1-90	PCB	353B68	2 to 10 000 Hz	$96.5\,\mathrm{mV/g}$

and far of couplings and supports.

As near the fast-closing system, there are a few supports and couplings. This position satisfies all the established criteria. Therefore, a vibration measurement station was placed there (*VIB-301*). Then, approximately $1.5\,\mathrm{m}$ below it, the second vibration measurement station was placed (*VIB-201*). It satisfies the criteria to be placed in a fully developed flow position and the criteria to be placed in a different structural condition of the first station. Once, this position is

relatively far from any couplings and supports.

Once the accelerometers used are uniaxial, two accelerometers were used in each vibration measurement station to measure the transverse vibrations (x, y axis). They were placed perpendicular to each other about the centre of the pipe. Finally, due to the experimental assembly and accelerometers available, it was not possible to evaluate the pipe vibration in the axial direction (z axis).

4.4 Visualisation apparatus

The visualisation section consists of a $500\,\mathrm{mm}$ glass pipe with the same diameter of the two-phase line, which enables the visualisation of the flow inside the pipe. The visualisation section is shown in Figure 4.6. Furthermore, the flow was recorded using a high-speed camera. The camera employed was a *Phantom VEO 640* of the *Vision Research Inc.* manufacturer. It is capable to record up to 1400 frames-per-second (fps) at its maximum resolution of $2560 \times 1600\,\mathrm{pixels}$. The highest frame rate is $290\,000\,\mathrm{fps}$ at $128 \times 4\,\mathrm{pixels}$ and the lower exposure time is $1\,\mu\mathrm{s}$ [74].

The camera used, incorporates a $25.6 \times 16\,\mathrm{mm}$ CMOS monochromatic sensor and $72\,\mathrm{GB}$ of internal RAM. Thus, it can record up to $8.5\,\mathrm{s}$ at the maximum resolution and frame rate. Different image and movie formats can be used to store the acquired data. In the first tests, the camera was set-up to save every frame in a *JPEG* image. However, due to the recorded time and fps used, it was difficult to handle and manage the large number of files generated. Hence, after some tests with the camera software options, it was found that the most convenient way to store the data was in a *AVI* file (movie extension). The software used to do the post-processing is capable of retrieving each film frame separately.

As mentioned by Monte Verde [75], the fps and the exposure time are one of the most critical settings in high-speed filming. To maximise the area covered by the camera and remove unnecessary parts of the recording the resolution of $512 \times 1600\,\mathrm{pixels}$ was chosen. At this resolution the camera can capture up to $1400\,\mathrm{fps}$, however, due to the flow velocities tested and after some tests, it was found that the frame rate of $250\,\mathrm{fps}$ was enough to capture the desired phenomenon reasonably. The image acquired was posteriorly rescaled to $256 \times 800\,\mathrm{pixels}$ with the camera software, this reduction is intended to decrease the output file size without lose too much valuable information.

Another essential feature to acquire sharp images is the depth of field. The depth of field is the distance of the camera focal plane where the objects are acceptably sharp. The depth of field is directly related to the lens aperture, where with lower apertures it is possible to get greater depth of field, however, as the aperture gets smaller more light is required. As the camera is fixed and so the distance between the camera and visualisation section, the exposure time and the aperture were set by balancing them while the focus was maintained. It was tried to get smaller exposure time and smaller aperture. Thus, after some tests the exposure time set was $30\,\mu\mathrm{s}$ and the aperture, $f/2.8$.

The light source utilized was a 24 LED lamp, model *MultiLED LT High Power 24 LED* from the *GS Vitec* manufacturer. It has in total $7700\,\mathrm{lm}$.

4.5 Data acquisition system

As seen in the previous sections, the instrumentation used has different characteristics, for instance, the signal incoming from the pressure and temperature transmitters are DC ranging from $4\,\mathrm{mA}$ to $20\,\mathrm{mA}$, while the signal incoming from the accelerometers are voltage signal ranging from $-24\,\mathrm{V}$ to $24\,\mathrm{V}$. Moreover, both the variable-frequency drive (*SY-101*) and the flow control valve (*FCV-101*) requires a signal to be generated ranging from $4\,\mathrm{mA}$ to $20\,\mathrm{mA}$.

One of the apparatus employed to acquire and generate the required signals was an acquisition system model *cDAQ NI-9178* (*DAQ-301*) from the manufacturer *National Instruments*. Moreover, to acquire the $4\,\mathrm{mA}$ to $20\,\mathrm{mA}$ signal, it was used an acquisition module model *NI-9203* from the same manufacturer. This module has eight channels, with 16-bit resolution, a range of $\pm 20\,\mathrm{mA}$ and maximum of $200\,\mathrm{kHz}$. Furthermore, the signal ranging from $4\,\mathrm{mA}$ to $20\,\mathrm{mA}$ was generated using an output module model *NI-9265* from the same manufacturer. This module has four channels, with 16-bit resolution, a range of $0\,\mathrm{mA}$ to $20\,\mathrm{mA}$ and maximum of $100\,\mathrm{kHz}$. All of these modules were mounted in the previously mentioned acquisition system.

The vibration signal was acquired using the *PXI* oscilloscope board *NI-5105* from the manufacturer *National Instruments*. It has 8 channels, with 12-bit resolution, a range of $-30\,\mathrm{V}$ to $30\,\mathrm{V}$ and maximum of $60\,\mathrm{MHz}$. This board is mounted in the *PXI* chassi model *PXIe-1071* (*PXI-301*). Moreover, the *cDAQ NI-9178* is connected through an USB connection to this chassi. As all instrumentation is connected to it, the *PXIe-1071* also executes the supervisory program, which was developed as part of this work.

All the acquisition, signal generation and control routines of the *SY-101* and *FCV-101* were elaborated using the programming language G, the programming language of the *National Instruments* software *LabVIEW* ®. Moreover, as commented in the Section 4.1, the supervisory developed also controls a set of relays that control the fast-closing system. It was elaborated a simple fuzzy controller to control the *SY-101* and *FCV-101*. The controller input is the liquid and gas mass flow, and its output is a control signal in mA to the variable-frequency drive and the flow control valve.

Furthermore, it was also implemented in the supervisory program the calculation of a few flow properties near to the second vibration station, such as liquid and gas superficial velocities and homogeneous GVF. The flow pattern was also estimated using the model proposed by Taitel, Bornea and Dukler [76]. They are calculated by acquiring 5000 points from the instrumentation filtered by a digital low-pass Butterworth filter of second order. Then, the average is taken from filtered signal, and finally, the properties are calculated using the average of the filtered signal. The data displayed in the supervisory program also uses the average of the filtered signal.

Finally, the acquisition loop of the experimental procedure, which will be described in the

next section, was automated. Therefore, all the points measured will rigorously follow the same experimental procedure and timing. The supervisory program also triggers the camera as it starts to acquire the vibration signal. It guarantees that the vibration and the camera record are synchronised.

A few safety measures were also embedded in the supervisory such as critical pressure in the *PT-102* and *PT-101*, fast-closing system status check and RAM check. Those measurements ensure that the experimental apparatus is working safely.

4.6 Experimental procedure

An experimental procedure was elaborated to perform the measurements, its flowchart is presented in the Figure 4.10 and detailed below:

1. Check if the stop valves of the liquid, gas and two-phase lines are open;
2. Turn on the following devices, the variable-frequency drive (*SY-101*), the gas flow control valve (*FCV-101*), the liquid mass flowmeter (*FT-101*), the acquisition system (*DAQ-301*), the vibration signal conditioner (*COND-301*) and finally the computer (*PXI-301*);
3. Regulates the gas line pressure;
4. Start the supervisory program;
5. Set the desired gas and liquid mass flow as the fuzzy controller input and wait for it to stabilise at the desired setpoints. If the stationary error is higher than the acceptable, a manual fine tuning is performed. Furthermore, if the desired liquid mass flow is lower than the pump lower limit, it is inputted a signal to stop the *SY-101*, and the bypass line valve is opened until the desired liquid mass is achieved;
6. Wait for the liquid and gas flow to stabilise. The stabilisation was determined by evaluating the relative standard deviation of the last $20\,\mathrm{s}$ of the liquid and gas mass flow measurements. If the relative standard deviation is lower than $0.8\,\%$ the flow is considered stabilised. This value was set after observing the visualisation section and the process variables at different conditions. In this case, the measurements are the average of the filtered signal mentioned in the Section 4.5;
7. Acquire and store data from the installed instrumentation for $30\,\mathrm{s}$. This time was determined experimentally to ensure that several unit cells of the slug flow could be recorded;
8. Trigger the fast-closing system;
9. Wait $20\,\mathrm{s}$ to ensure that the gas phase separates from the liquid phase and open the relief valve;

10. Wait 15 s for the *PT-301* reading to stabilize;
11. Measure the *PT-301* and then calculate the GVF and store it;
12. Close the relief valve and trigger the fast-closing system to close the bypass line and open the main line;
13. Return to the item 5 to perform a new measurement.

The waiting times mentioned above were determined experimentally.

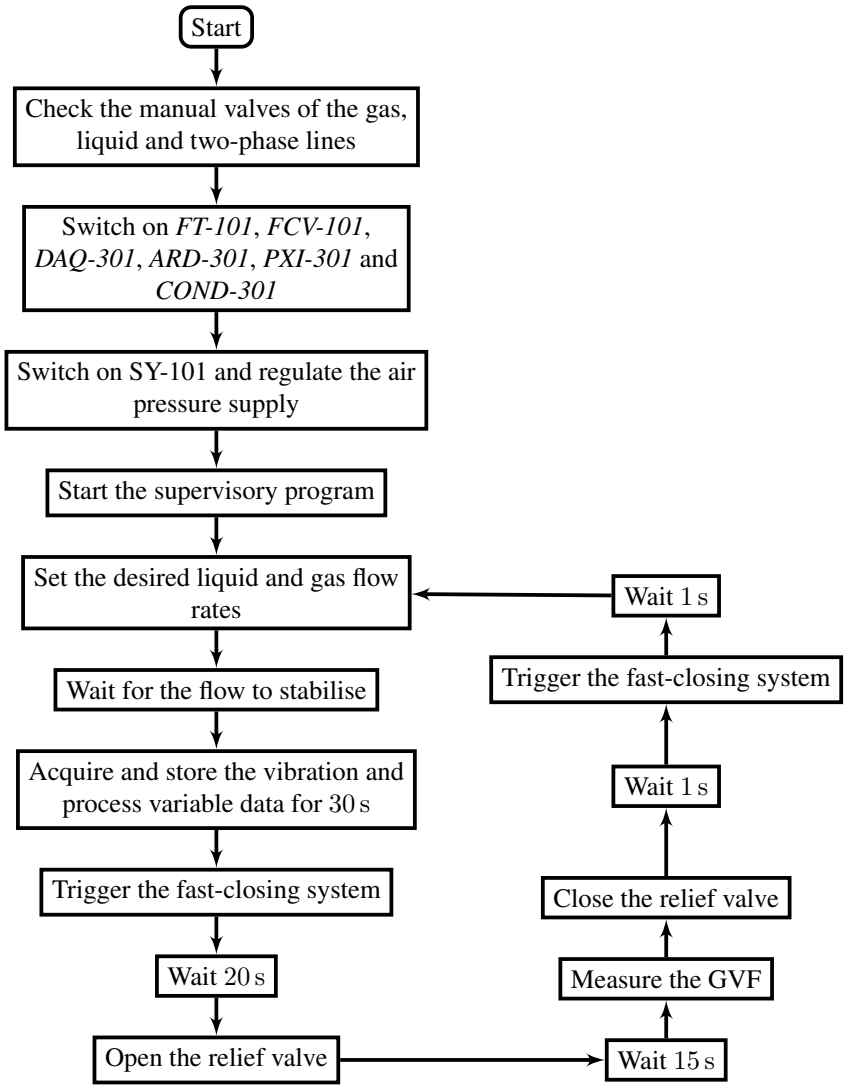

Figure 4.10: Experimental procedure flowchart.

4.7 Test matrix

Initially, a series of preliminary tests were performed on the bench to define its limits. First, it was determined the maximum liquid superficial velocity without gas by manually inputting a

control signal of $20\,\mathrm{mA}$ to the *SY-101*. Then, keeping the liquid superficial velocity, a similar control signal was manually inputted into the *FCV-101*. Hence, both maximum superficial velocities were set.

Once set the maximum superficial velocities, the test matrix was elaborated considering those limits and a homogeneous distribution of the flow pattern of the experimental points according to the model proposed by Taitel, Bornea and Dukler [76]. Thus, it was determined a set of 36 experimental points, and for each point, it was performed four repetitions to evaluate their repeatability. Therefore, a total of 144 measurements were performed. Those points were measured by fixing a liquid flow rate and increasing or decreasing the gas flow rate up to 6 points. After the measurement of the fourth repetition of the sixth point, the liquid flow rate is increased. The test matrix as a function of the liquid and gas superficial velocities is presented in the Figure 4.11. The uncertainty analysis and error propagation for each transducer and calculated two-phase flow property are presented in Appendix B.

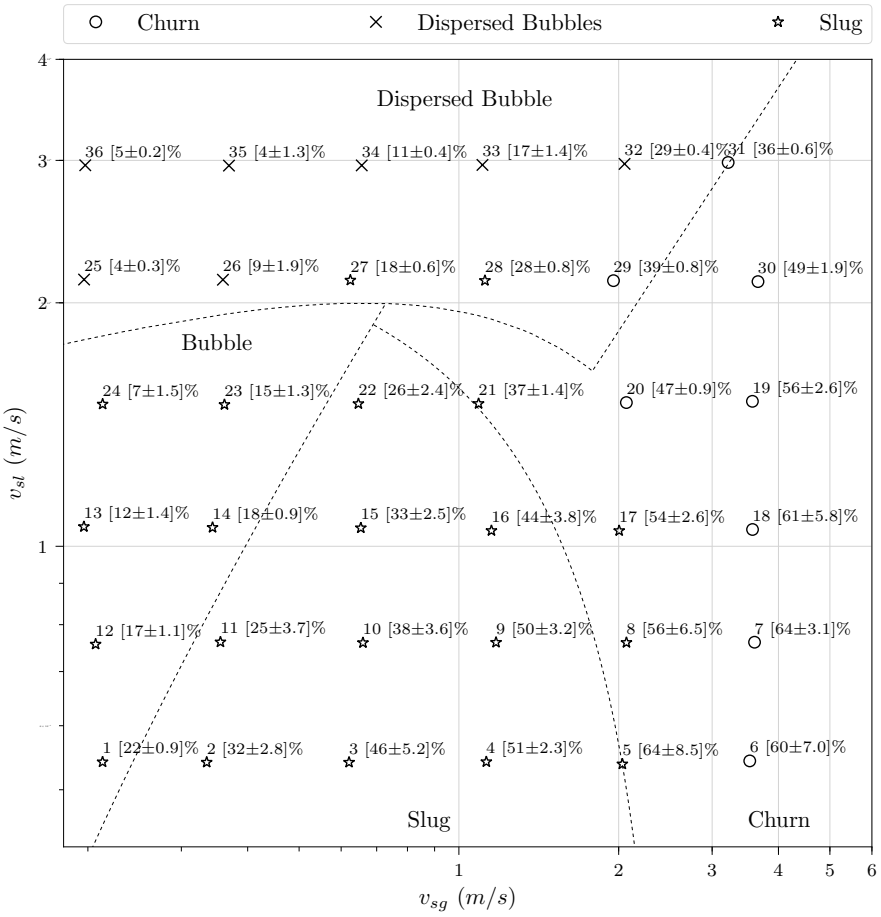

Figure 4.11: Test matrix as function of the liquid and gas superficial velocities.

In the Figure 4.11 the first number above the symbols represents the point number. The number inside the brackets are the GVF measured by the fast-closing system followed by its standard deviation along the four repetitions. The dashed lines are the lines that delimit the different flow patterns according to the model proposed by Taitel, Bornea and Dukler

[76]. Finally, the points symbols represent the flow pattern classified visually by analysing the camera recordings for each point. The Figure 4.12 shows the observed flow patterns and their classifications determined visually. The subfigures 4.12a, 4.12b and 4.12c shows the slug flow, churn flow and dispersed bubbles respectively.

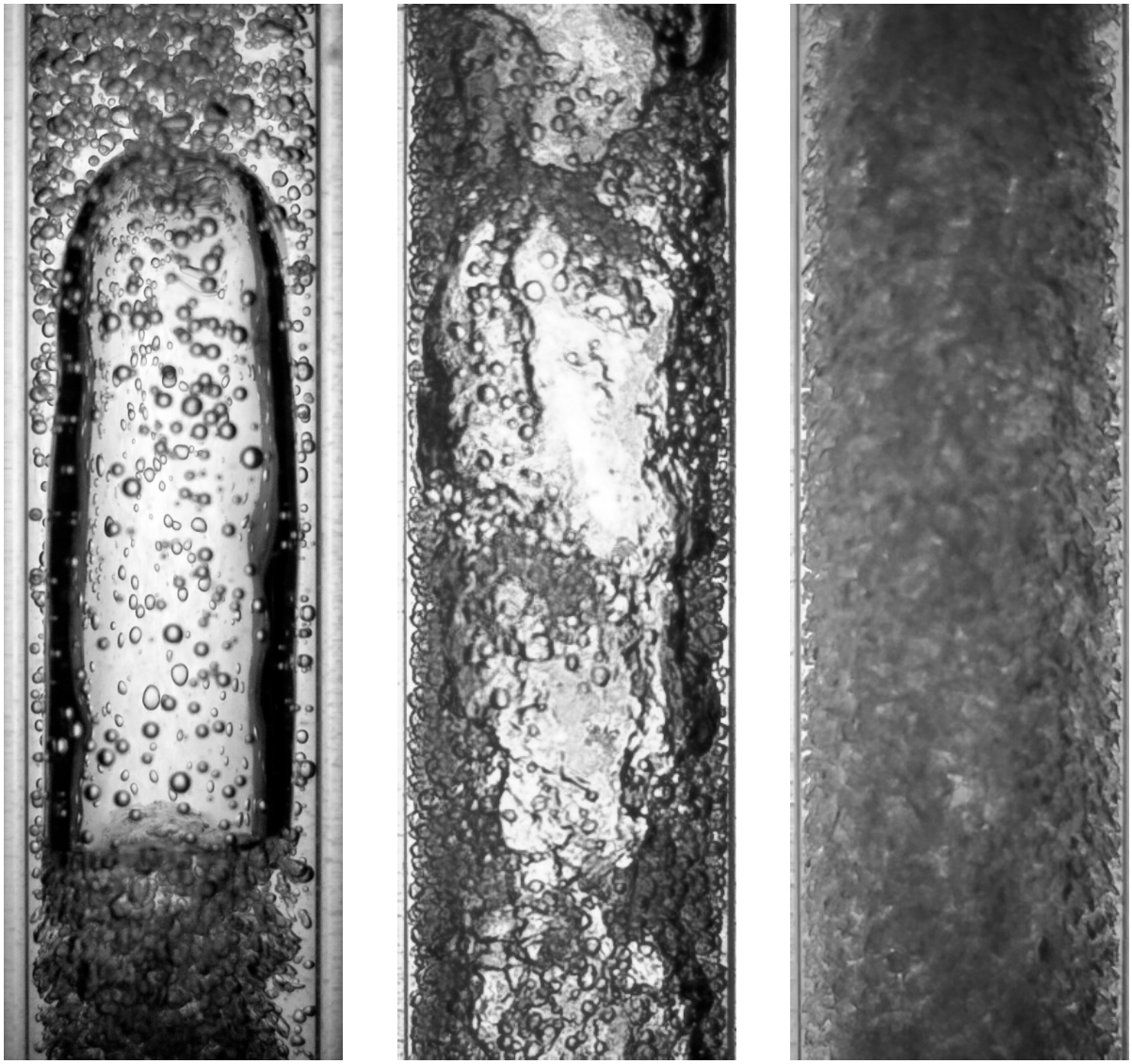

(a) Slug. (b) Churn. (c) Dispersed bubbles.

Figure 4.12: Observed flow patterns and their visual classification.

It is important to note that the acquisitions 25, 35 and 36 presented a GVF lower than the lower limit of the measurement system. Therefore, the GVF values of those points are not reliable. Additionally, it is undoubtedly observable in the Figure 4.11 that the flow pattern classified visually, in general, agrees with the Taitel, Bornea and Dukler [76] model, but the acquisitions 27, 28, 29 and 31, which are located near the transition lines.

5 Results

This chapter presents the results obtained by analysing the data acquired as discussed in Section 4, with the tools and concepts presented in Section 3. Thereunto, this chapter is divided into five sections. The first section uses the Fourier transform to analyse the vibration signal. The second section uses the time-frequency tools presented in Section 3.3 to analyse the vibration signal. The third section uses the energy of a given frequency band to draw some analysis. In the fourth section the vibration signal is filtered with a digital Butterworth filter, and then the Hilbert transform is used. Section five presents some correlations of the envelope of the vibration signal with the two-phase flow properties.

Important to mention that during the data importation from the stored data, it was observed that it was missing some information, solely, about the acquisition 13 in the saved file. Therefore, this acquisition will be not used during the analysis in this chapter. Thus, the total of points will be of 140 instead of 144.

5.1 Frequency domain analysis

A usual approach used to analyse the vibration signal is to perform the analysis in the frequency domain. In this context, the frequency domain analysis was used by Ortiz-Vidal, Mureithi and Rodriguez [15], Ortiz-Vidal, Rodriguez and Mureithi [16], Geng, Ren and Hua [45] and Hua *et al.* [44]. Thus, as an initial study, the FFT of the acquired vibration signal was taken. This frequency domain analysis aims to verify if, similarly to the PSD obtained by Hua *et al.* [44] and Geng, Ren and Hua [45], the spectrum for vertical upward flow also has such different spectrum between the different flow patterns. Thus, in this analysis, the focus was to identify subtle differences in the spectrum across the different flow patterns.

As described in Section 4.3, the accelerometer used has a frequency range of $2\,\mathrm{Hz}$ to $10\,000\,\mathrm{Hz}$ and the sample rate employed was $60\,\mathrm{kHz}$. Therefore, it is possible to obtain the frequencies up to $30\,\mathrm{kHz}$ with the Fourier transform. However, the frequency band over $10\,\mathrm{kHz}$ was neglected due to the transducer frequency range.

It was measured in total 140 points. Therefore, it is impracticable to analyse all of them in this work. Thus, the repetition 1 of the acquisitions 1, 6 and 25 were selected. The criteria for selecting the acquisitions were the flow pattern and the liquid and gas velocities. As mentioned, in the Section 2.1.1 and 2.1.2 the studies found a clear relationship between the flow velocities and the vibration signal, where higher flow rates translates to higher vibration amplitudes. Thus, cases with lower velocities are a limitation in this work. Therefore, the acquisitions 1, 6 and 25 are the slug, churn, and dispersed bubbles flow patterns with the lower velocities. Moreover, the

flow turbulence also has a relationship, where higher turbulence also tends to translate to higher vibration amplitudes.

In the single-phase flow, the flow turbulence is associated with its Reynolds number. On the other hand, due to the complex interactions between the phases of two-phase flow, it is challenging to establish criteria that measure the turbulence in two-phase flow accurately. In this context, there is the mixture Reynolds number, presented in Equation 3.43. It tries to account the turbulence in two-phase flows but with a non-slip condition between the phases. The non-slip condition assumption is valid in dispersed bubbles flows where the slippage between the phases are negligible.

Nevertheless, this work does not aim to measure the turbulence accurately either use it to calculate a property, but to quantify it, to get a notion of the flow turbulence and perform some analysis. Furthermore, as mentioned before, Ortiz-Vidal, Rodriguez and Mureithi [16] found a quadratic relationship between the mixture Reynolds number and the vibration signal variance. The quadratic fit does not present a reasonable fit for GVF higher than $25\,\%$. However, it is clear the existence of a trend where higher mixture Reynolds number translates to a higher variance of the vibration signal.

Then, the mixture Reynolds number for each acquisition and repetition was calculated using the homogeneous GVF. The mean of the mixture Reynolds number with its standard deviation across the repetition is shown in Figure 5.1. The symbols indicate the flow pattern and the bars the standard deviation. It is important to note that due the low standard deviation between the repetitions the bars are in some cases are inside the flow pattern symbol.

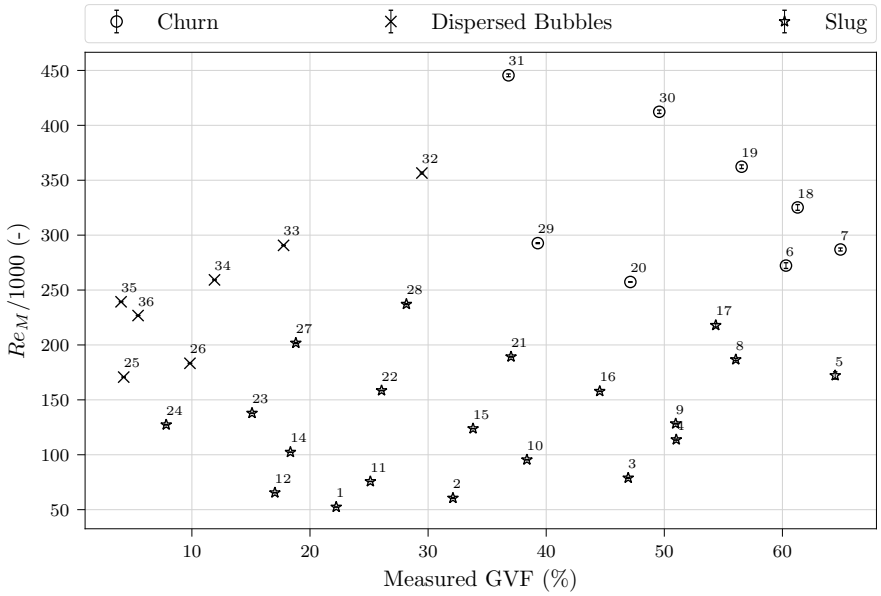

Figure 5.1: Average and standard deviation of the mixture Reynolds number as function of the measured GVF.

Finally, to calculate the Fourier transform of the vibration signal, it was used a Hanning window to reduce the leakage effect. Then, the Fourier transform of the selected acquisitions

using the FFT algorithm are shown in Figure 5.2.

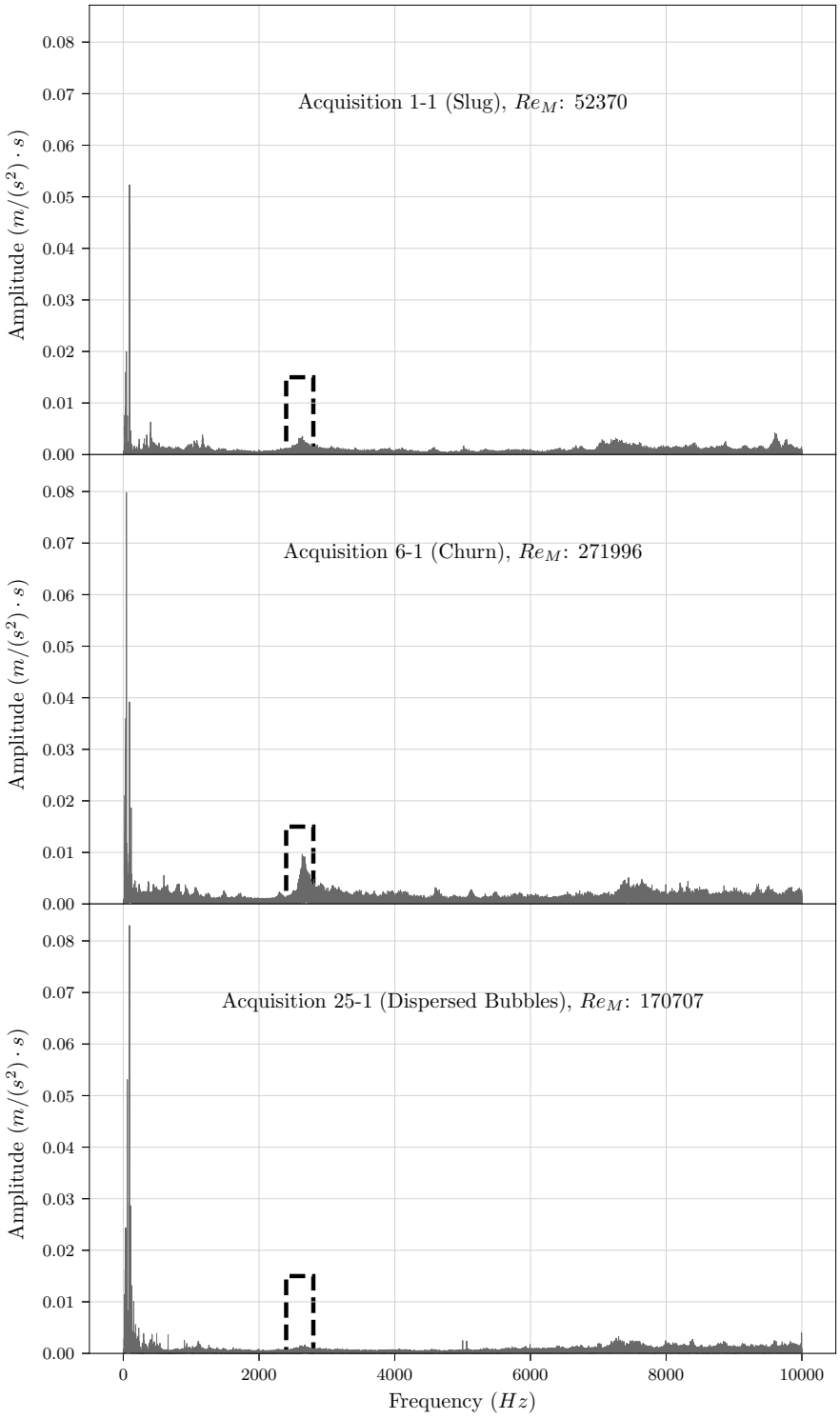

Figure 5.2: FFT of the repetition 1 of the acquisitions 1, 6 and 25.

Analysing the vibration spectrum of the selected acquisitions presented in Figure 5.2, it is easy to see that for higher mixture Reynolds number, higher are the frequencies amplitudes. This is in good agreement with the presented by Ortiz-Vidal, Rodriguez and Mureithi [16], Ortiz-Vidal, Mureithi and Rodriguez [15], Geng, Ren and Hua [45] and Hua *et al.* [44]. However,

carefully analysing the spectrum, it possible to note some key differences between them. In the acquisition 25, the higher spectrum amplitudes are concentrated in lower frequencies from around $10\,\mathrm{Hz}$ to $250\,\mathrm{Hz}$. In the acquisition 6 it is observable that the higher amplitudes are now concentrated from around $40\,\mathrm{Hz}$ to $120\,\mathrm{Hz}$. It is also perceptible an amplitude increase of all frequencies. This increase is consistent with the stated by Ortiz-Vidal, Rodriguez and Mureithi [16], Ortiz-Vidal, Mureithi and Rodriguez [15] and Blevins [20], where they mention that pressure fluctuations due to turbulence excite the pipe system in a broad range of frequencies. Therefore, for underdamped modes it is expected that the structural response increases in and near the resonance frequencies. In the acquisition 6 spectrum, it is also noticeable considerably high amplitudes at the frequency band of $2400\,\mathrm{Hz}$ to $2800\,\mathrm{Hz}$. The frequency band of $2400\,\mathrm{Hz}$ to $2800\,\mathrm{Hz}$ is highlighted with a dashed black rectangle in Figure 5.2 for the three acquisitions.

Investigating the acquisition 1 spectrum, it is perceptible that it is somewhat similar to the acquisition 6. Likewise the acquisition 6, the higher frequencies are located around $40\,\mathrm{Hz}$ to $120\,\mathrm{Hz}$, while at the same time it is noticeable a slight increase of the amplitudes in the frequency band of $2400\,\mathrm{Hz}$ to $2800\,\mathrm{Hz}$. On the other hand, analysing the amplitudes of the frequency band of $2400\,\mathrm{Hz}$ to $2800\,\mathrm{Hz}$ of the acquisition 25, there is no noticeable increase in the frequencies amplitude in and near this band.

By contrasting the amplitude increase in the frequency band mentioned above with the mixture Reynolds number presented in Figure 5.1. It is noticeable that the mixture Reynolds number of acquisition 25 is higher than the acquisition 1, while the acquisition 25 does not present an increase of the amplitudes near the highlighted frequency band. Therefore, the structural excitation mechanism presented in the acquisitions 1 and 6 seems to be different to the acquisition 25. On the other hand, the flow pattern of the acquisitions 1 and 6 are known to have an oscillatory passage of a significant amount of liquid, liquid slugs, and then gas, 'Taylor bubble', where just after the 'Taylor bubble' there is a highly turbulent zone.

The amplitude increase in the highlighted frequency band was also observed in the others 137 points. It was observed that as the mixture Reynolds number increases, the amplitude of the frequency band increased, at the same time as the acquisition approached the dispersed bubbles, it decreased. This frequency band increased mostly in flow patterns that are characterised to have an oscillatory momentum flux and to have a highly turbulent zone just after the gas pocket passage, and therefore, there is a significant variation of turbulence along the flow. Finally, as the amplitude of the vibration is associated with the fluid turbulence, and the slug and churn flow does not have a 'constant' turbulence, it is possible to infer that the structural excitation mechanism in a pipe subjected to those patterns is slightly different to the dispersed bubble case, where the primary excitation cause is transient.

As mentioned in Section 3.3, the Fourier transform is not appropriate to analyse cases where there is a temporary phenomenon. Thus, the analysis of the vibration signal using time-frequency analysis are desirable, particularly, in the slug and churn flow pattern cases.

5.2 Time-frequency Analysis

As suggested in Section 5.1, the analysis in frequency domain points to a transient phenomenon that is particularly prominent in the frequency band of $2400\,\mathrm{Hz}$ to $2800\,\mathrm{Hz}$. Thus, time-frequency analysis (TFA) may be preferable to the detriment of frequency domain analysis only. Among the various TFA techniques, this work focused on the short-time Fourier transform and wavelet transform. To be able to contrast the frequency spectrum with the TFA output, the acquisitions subjected to the TFA were the same of the Section 5.1. However, as the wavelet transform keeps the time resolution, the analysis of the $30\,\mathrm{s}$ of measurement is not practicable due to the computational resources required. Thus, the TFA analysis was performed over $10\,\mathrm{s}$ of measurement.

5.2.1 Short time Fourier transform

In general, the STFT requires at least three parameters to be set. They are the window size, the number of points to overlap between the windows and the window function. The flow filming was used to determine the window size, where it was observed the duration of the highly turbulent zone after the 'Taylor bubble'. After analysing different cases, from the slowest to the fastest ones, it was determined the window time of $5\,\mathrm{ms}$ which results in 3000 samples. The overlap between the windows was set to be the half of the window size or $2.5\,\mathrm{ms}$ or 1500 samples. Finally, the window function used was the same of the frequency domain analysis due to the same reasons.

The STFT for the three selected acquisitions were computed, and they are shown in Figure 5.3. The three spectrograms presented use the same logarithm scale. In the grayscale used, the points with higher amplitudes are darker, and the points with lower amplitudes are the lighter points. Moreover, the grayscale was adjusted to emphasise the frequencies from $2400\,\mathrm{Hz}$ to $2800\,\mathrm{Hz}$. A dashed black rectangle in all spectrograms highlights this frequency band.

Analysing the vibration spectrogram of the acquisition 25 presented in Figure 5.3, it is noticeable that the lower frequencies amplitudes are considerably higher than the others in all-time analysed. This observation is compatible with the observed in Section 5.1. It is evident that in the spectrogram of the acquisition 25 there is no significant change in the frequencies amplitudes along the time. It suggests that there is no significant turbulence difference along the flow in the case of dispersed bubbles flow. This conclusion is in good agreement with the non-slip condition case that is valid for dispersed bubbles flow pattern. In the homogeneous model, the two-phase flow is considered as a single-phase flow of a fluid with properties obtained by weighting the phases properties with the GVF. Thus, there are no complex interactions between the phases that may result in a significant turbulence change along the time.

Moreover, it is perceptible that in general, the spectrogram of the acquisition 6 is darker than the acquisition 1 and 25. This observation is consistent with the observed and discussed in the

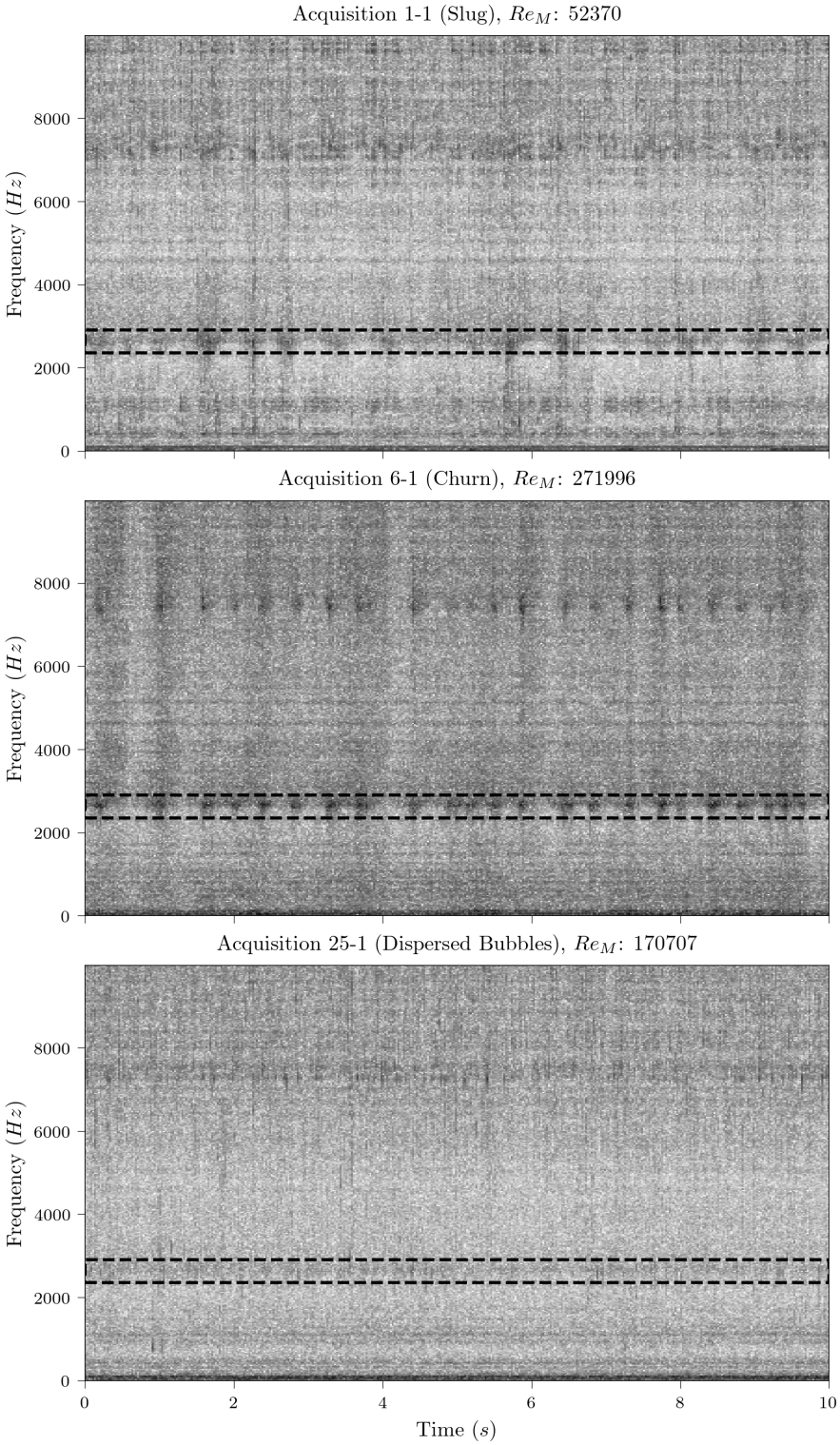

Figure 5.3: STFT of 10 s of the repetition 1 of the acquisitions 1, 6 and 25.

Section 5.1, where the increase of the mixture Reynolds number increased all amplitudes of the spectrum, particularly in the acquisition 6.

Analysing the vibration spectrogram of the acquisitions 1 and 6 presented in Figure 5.3, it is perceptible that, in the highlighted frequency bands, there is a temporal variation of the amp-

litudes. Moreover, despite this temporal amplitude variation be more evident in the highlighted frequency band, it is observable, particularly in the acquisition 6 case, that the amplitude of the spectrum increased at the same time that the selected band also increased. It supports the mentioned in Section 5.1, where it was assumed that the high amplitudes in the frequencies from $2400\,\mathrm{Hz}$ to $2800\,\mathrm{Hz}$ observed in the acquisitions 1 and 6 were due to the turbulence variance along the flow in slug and churn flow patterns. Moreover, this observation is in complete agreement with the stated by Ortiz-Vidal, Rodriguez and Mureithi [16], Ortiz-Vidal, Mureithi and Rodriguez [15] and Blevins [20], where the pressure fluctuations due to turbulence excite the pipe system in a wide range of frequencies. Consequently, for underdamped modes it is expected that the structural response increases in and near the resonance frequencies. Thus, the most pronounced increase in amplitude in the highlighted region indicates that there is at least one resonance frequency in this frequency band. However, it is required further investigation to be sure about this affirmation.

The temporal variation of the amplitude of the highlighted band was also observed in the other 137 points. Similarly to the observed in the Section 5.1, the amplitude variation increased as the mixture Reynolds number increased, at the same that it decreased when the point approached the dispersed bubble flow pattern. It was also observed in the slug flow case that, in general, the points of the first column of the test matrix and the acquisition 23 and its repetitions, presented the lowest temporal amplitude variation. The acquisition 23 is near the bubbles to dispersed bubbles transition according to Taitel, Bornea and Dukler [76] criterion.

Moreover, despite the points of the first column that have been classified as slug flow, according to the Taitel, Bornea and Dukler [76] criteria, those points are classified as bubbles, which means that those points may be located in a transition region between the bubbles and slug flow. Thus, the lower temporal variation of the amplitudes is correlated to the beginning of the bubble coalescence. Thus, lower turbulence levels are expected at the end of the 'Taylor bubble'.

To observe the temporal amplitude variation of the vibration in the highlighted frequency band, the vibration signal was filtered. It was allowed only frequencies inside the highlighted frequency band. The characteristics of the filter used will be discussed in Section 5.4. Moreover, it was difficult to synchronise the vibration signal with the flow filming with the transducers positioning described in Section 4.3. Thus, a different transducer positioning was used. It will be discussed in Section 5.6.

The Figure 5.4 presents the filtered vibration signal next to the flow image. The liquid and gas superficial velocities are approximately the same of the acquisition 1. To facilitate comparing the image with the filtered vibration signal, the Y-axis is the time axis, and the X-axis is the vibration amplitude. Moreover, the Y-axis limits of the filtered vibration signal were set by estimating the 'Taylor bubble' velocity, V_{TB}, with the flow filming.

As can be observed in Figure 5.4, there is a significant increase in the vibration signal amplitude just after the 'Taylor bubble' passage, region *R2*. Then, in region *R3* it is perceptible that turbulent region after the 'Taylor bubble' has amplitudes lower than the amplitudes immediately

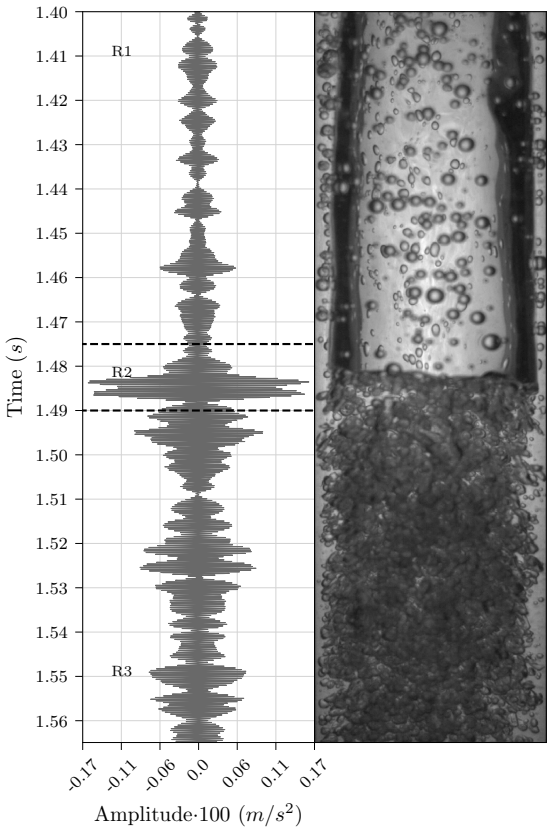

Figure 5.4: Filtered vibration signal synchronised with the flow image.

after the 'Taylor bubble', but it has higher amplitudes than the region *R1*, which was during the 'Taylor bubble' passage. As the amplitude of the vibration is associated with the fluid turbulence, these observations are in agreement and enforce the mentioned above, where it was stated that the slug and churn flow does not have 'constant' turbulence.

As the turbulence at the end of the 'Taylor bubble' is significant to be detected by measuring the pipe vibration, the simple detection of the amplitude peaks of the highlighted frequency band is enough to quantify the number of 'Taylor bubbles' that has passed. Also, it is possible to calculate the slug frequency, which is a parameter used in mechanistic models to determine other parameters of the slug flow. Furthermore, if a high attenuation of the highlighted frequency is observed along the pipe, it will be possible to estimate the V_{GTB} of slug flow by using the cross-correlation with the two vibration measurement station.

5.2.2 Wavelet transform

The STFT is more appropriate than the Fourier transform to analyse transient phenomena. However, due to the uncertainty principle of Gabor, with the Fourier transform it is not possible to get high resolution both in time and frequency. The higher is the frequency resolution the lower is the time resolution. Therefore, the wavelet transform is preferable. Once, by adjusting it, it is possible to get higher time and frequency resolution than the STFT.

The wavelet transform of the selected acquisitions was calculated by using a Morlet wavelet of frequency of $20\,\mathrm{Hz}$. The results are shown in Figure 5.5. Similarly to the Section 5.2.1, the three spectrograms presented uses the same logarithm scale. In the grayscale used, the points with higher amplitudes are darker, and the points with lower amplitudes are the lighter points. Moreover, the grayscale was adjusted to emphasise the frequencies from $2400\,\mathrm{Hz}$ to $2800\,\mathrm{Hz}$. Once the analysis on the frequency domain pointed to a transient phenomenon that is particularly prominent in the frequency band of $2400\,\mathrm{Hz}$ to $2800\,\mathrm{Hz}$. A dashed black rectangle in all spectrograms highlights this frequency band.

As can be seen in Figure 5.5, the spectrograms calculated with the wavelet transform are similar to the calculated with the STFT. The amplitude variation along the time of the frequencies from $2400\,\mathrm{Hz}$ to $2800\,\mathrm{Hz}$ for the acquisitions 1 and 6, can also be observed. Also, in the acquisition 25 the amplitude of the selected frequency band did not present any noticeable and significant variation in time. However, carefully observing the higher frequencies, it is possible to note that the wavelet frequency used was not appropriate to them. Thus, to analyse the highlighted frequency band it will be necessary to adjust the wavelet frequency, which will be discussed in the Section 5.3.

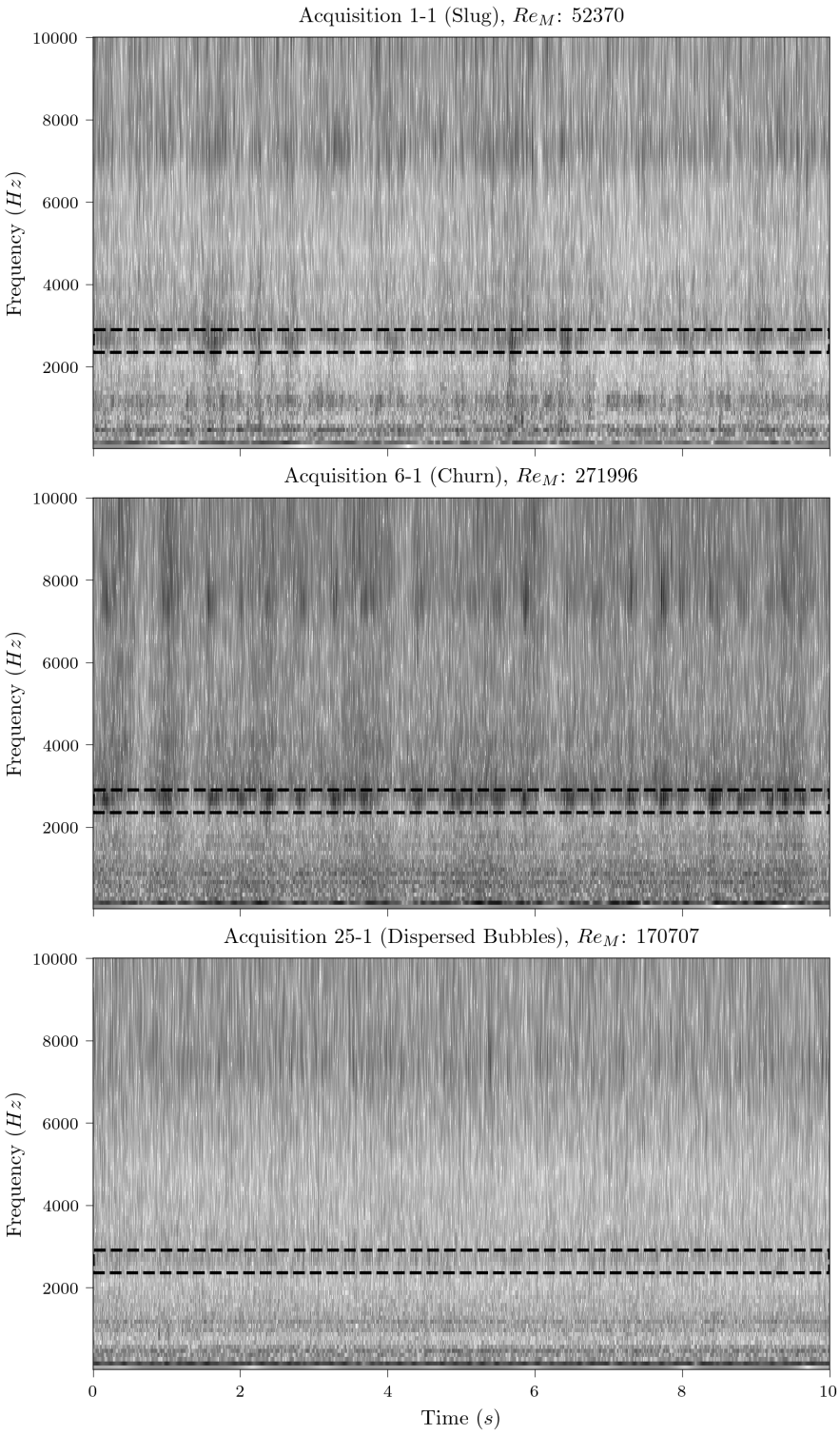

Figure 5.5: Wavelet transform of 10 s of the repetition 1 of the acquisitions 1, 6 and 25.

5.3 Signal energy

In Section 5.2.1, it was mentioned that with detection of the peaks of the frequency band of 2400 Hz to 2800 Hz, it would be possible to detect the 'Taylor bubble' passage and determine other flow properties. However, the peak detection using the spectrogram is impracticable due to

the resolution required and the computational resources available. The main issue is related to the RAM memory available, once the wavelet transform requires to store a matrix $\mathbf{W} \in \mathbb{R}^{F \times N}$, where F is number of frequencies to be calculated and N is the signal length. Thus, as the sample rate and/or the acquisition time increases, the memory required to store the spectrogram increases dramatically. Besides, the peak detection algorithm may require to temporary store processed matrices with similar dimensions, which requires even more RAM memory.

Moreover, the spectrogram use may result in wrong peak detection due to other frequencies that also changes in time, and the most of the algorithms available to detect peaks are for one-dimensional case. Thus, to avoid the possibility to detect frequency peak outside the frequency band of interest, to be able to use simpler algorithms to detect peaks and to reduce the computational cost, the energy of the frequency band of interest was used.

The Section 3.3.2 stated that the energy density, $E(\tau, f)$, in the wavelet transform is given by

$$E(\tau, f) = |W(\tau, f)|^2, \tag{5.1}$$

where f is the frequency. Thus, the energy density for a given frequency band from f_1 to f_2, for the time instant τ, can be written as

$$E(\tau) = \int_{f_1}^{f_2} |W(\tau, f)|^2 \, df. \tag{5.2}$$

Finally, for a frequency discretization k, the Equation 5.2 can be written as

$$E(\tau) = \sum_{k=1}^{f_2 - f_1} |W(\tau, f_{f_1+k})|^2. \tag{5.3}$$

As mentioned in Section 5.2.2, the frequency of the wavelet function was not appropriate to describe the higher frequencies. Therefore, in this case, the frequency of the Morlet wavelet function was adjusted to $200\,\mathrm{Hz}$. It was obtained by manually balancing the wavelet spread in frequency domain and time domain to obtain a reasonable time resolution. Then, the wavelet transform for the band of interest of the vibration signal of the selected acquisitions were calculated. Finally, it was used the Equation 5.3 to calculate the energy of the band of interest. The spectrogram and the energy of the band of interest are shown in Figures 5.6 and 5.7. The Figure 5.6 is the acquisition 1 case and the Figure 5.7 is the acquisition 6 case.

Similarly to the Section 5.2.1, the two spectrograms presented in Figures 5.6 and 5.7 uses logarithm scale. In the grayscale used, the points with higher amplitudes are darker, and the points with lower amplitudes are the lighter points.

Analysing the Figure 5.6 and 5.7, it is clear the relationship between the spectrogram and the signal energy. The darker vertical lines in the spectrogram translate into higher peaks in the signal energy. Furthermore, the signal energy highlights the observed in Section 5.2. It is clear, particularly in acquisition 6, that there is an amplitude variation of the selected band along the time. In addition, it is noticeable that the number of peaks in Figure 5.7 are higher than the

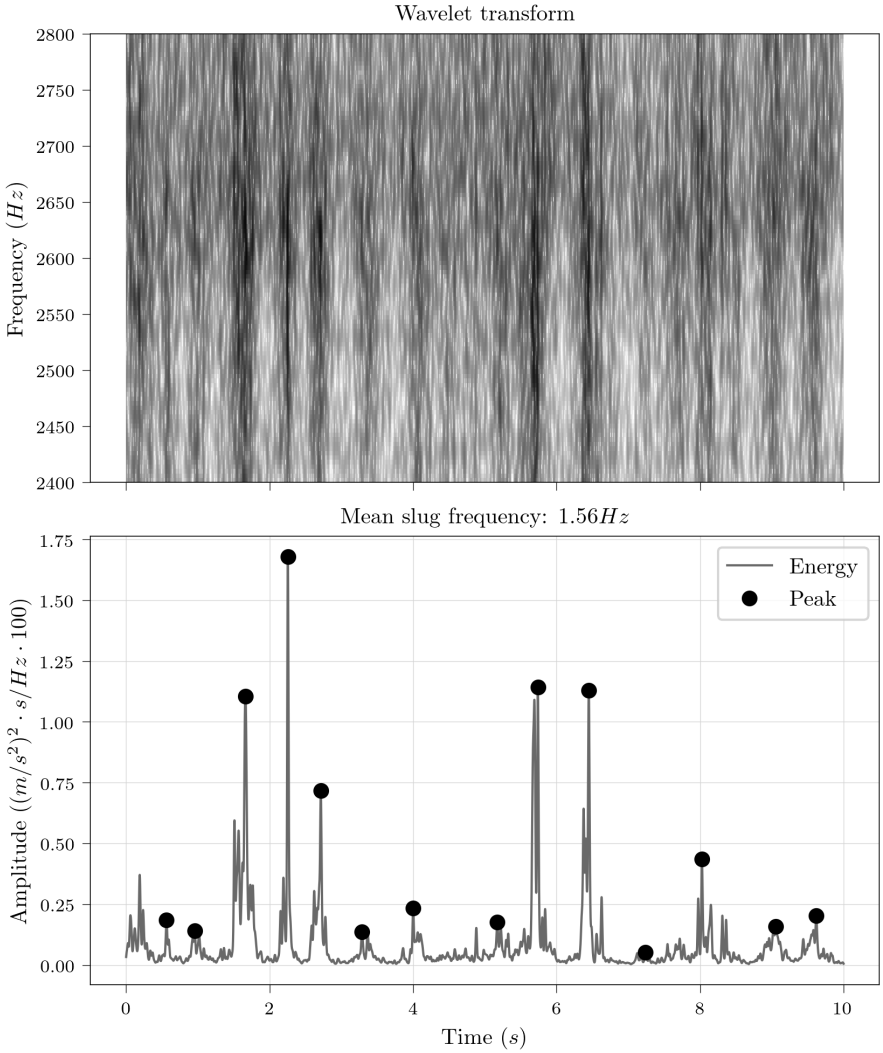

Figure 5.6: Wavelet transform of 10 s of the band of interest of the repetition 1 of the acquisition 1 (slug) with the signal energy calculated with Equation 5.3.

presented in Figure 5.6. This difference is consistent with the experiments, once the gas velocity of the acquisition 6 is higher than the acquisition 1.

However, it is perceptible a substantial difference in the energy amplitudes, when comparing the signal energy from the acquisition 1 with the acquisition 6. Moreover, it is possible to note in Figure 5.6, that the turbulent zone behind the 'Taylor bubble' does not have a significant effect when compared with other structural excitation mechanisms. Once, there are some regions with considerable energy that, when compared with the wavelet transform, it is not possible to identify a clear increase in all spectrum. For instance, the energy peak near the fifth second in Figure 5.6. Thus, with the turbulence reduction, it will be more difficult to discern the turbulence generated by the 'Taylor bubble' passage from other structural excitation. It is in agreement with the mentioned in Section 5.2.1, where it was observed that for the points classified as slug flow in the first column of the test matrix, the amplitude variation decreases.

It was tried a wide variety of approaches to detect the peaks in the signal energy. They were

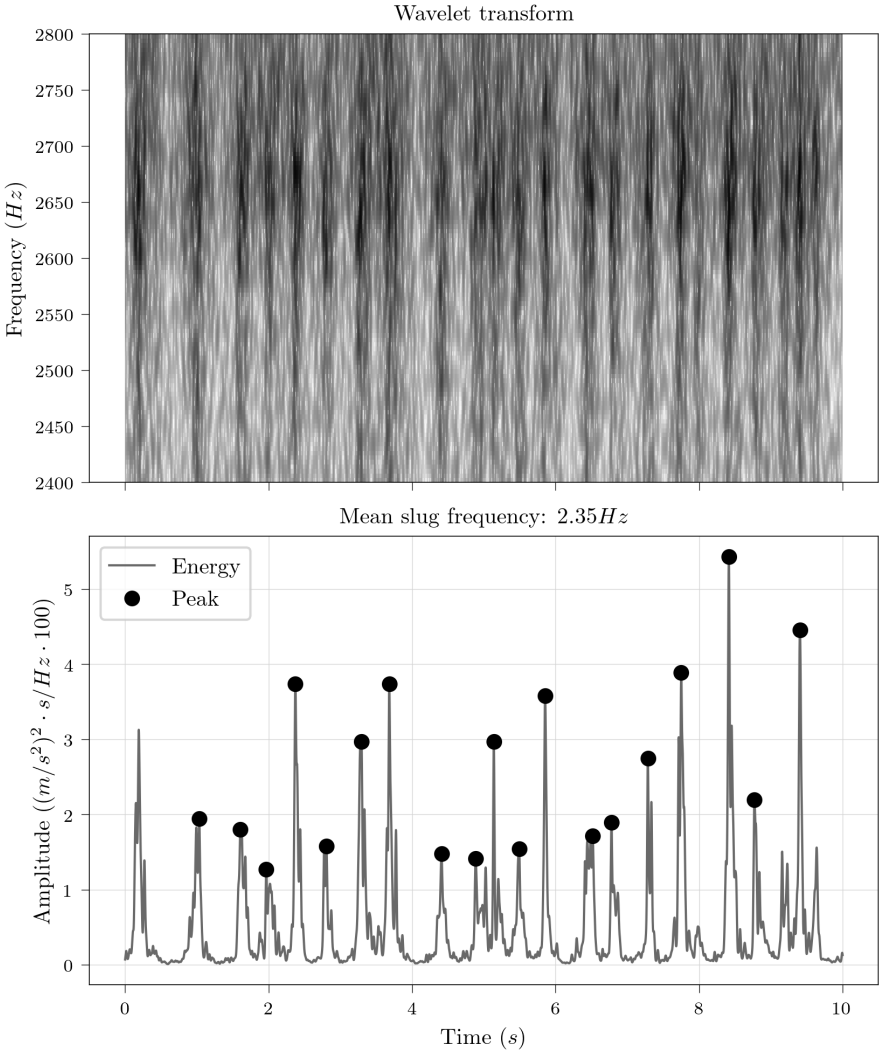

Figure 5.7: Wavelet transform of $10\,\mathrm{s}$ of the band of interest of the repetition 1 of the acquisition 6 (churn) with the signal energy calculated with Equation 5.3.

a threshold, statistical analysis to detect outliers with the signal standard deviation and with the median absolute deviation. It was also tried algorithms that establish a threshold and exclude the peaks that have a short duration. However, none of them presented a reasonable overall performance. Some of them worked reasonably well for some instances but failed for others. It was observed that the energy amplitude varied dramatically across the same flow pattern and between flow patterns. Finally, after some research and tests in different cases, the algorithm mentioned in Section 3.5 presented a satisfactory performance.

Thus, using the algorithm mentioned in Section 3.5, it was possible to detect the peaks highlighted as a black dot in Figures 5.6 and 5.7. Finally, the mean frequency was obtained by calculating the average of the reciprocal value of each time interval of the detected peaks. It is given by

$$f_{mean} = \frac{1}{N-1} \sum_{k=1}^{N-1} \frac{1}{dt_k}, \tag{5.4}$$

where N is the number of peaks detected and dt_k is time interval of two detected peaks in sequence. The mean frequency are shown in Figures 5.6 and 5.7.

5.4 Time analysis

As observed in Section 5.3, the signal energy varied dramatically in the presence of the highly turbulent region behind the 'Taylor bubble'. As this variation is significant, particularly in the acquisition 6, it is relevant to analyse the signal in the time domain. In the following analysis, it was used a digital pass-band filter to analyse the signal in time domain. The cut-off frequencies are 2400 Hz and 2800 Hz, which is the same as used in the previous sections. The filter used was a Butterworth filter of second order.

The time domain analysis was restricted to the first 10 s of measurement, to be able to easily compare the results with the presented in Sections 5.2 and 5.3. The filtered vibration signal for repetition 1 of the acquisitions 1 and 6 are presented as a grey line in Figure 5.8 and 5.9 respectively. Furthermore, the amplitudes of both figures were set to be the same, to be easier to compare them.

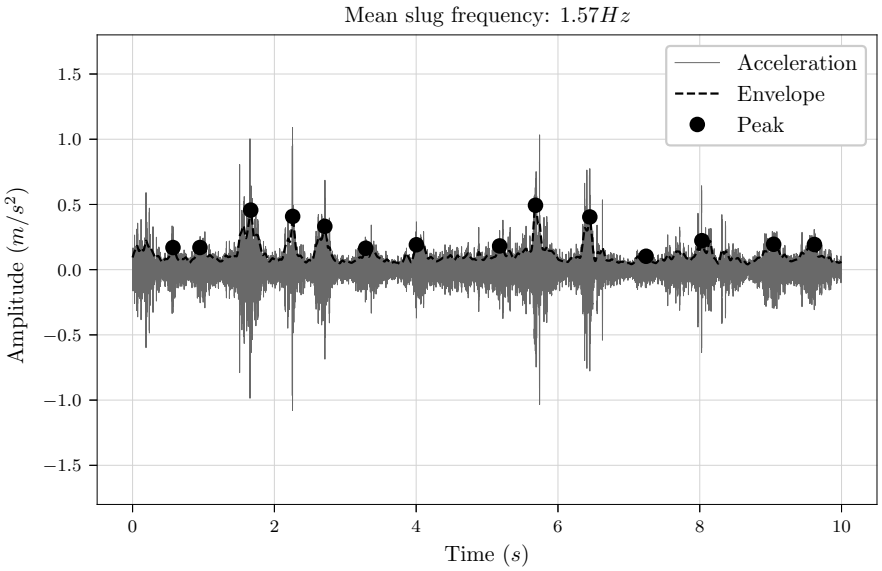

Figure 5.8: 10 s of the filtered vibration signal in the band of interest of the repetition 1 of the acquisition 1 and the filtered modulus of the Hilbert transform of the signal.

Similarly to the signal energy presented in Section 5.3, the peaks in the filtered vibration signal is easily observable in Figures 5.8 and 5.9. Moreover, comparing the peaks of the filtered signal, Figures 5.8 and 5.9, with the signal energy, Figures 5.6 and 5.7, it is noticeable a relationship between them. The peaks found in the filtered signal can also be observed in the

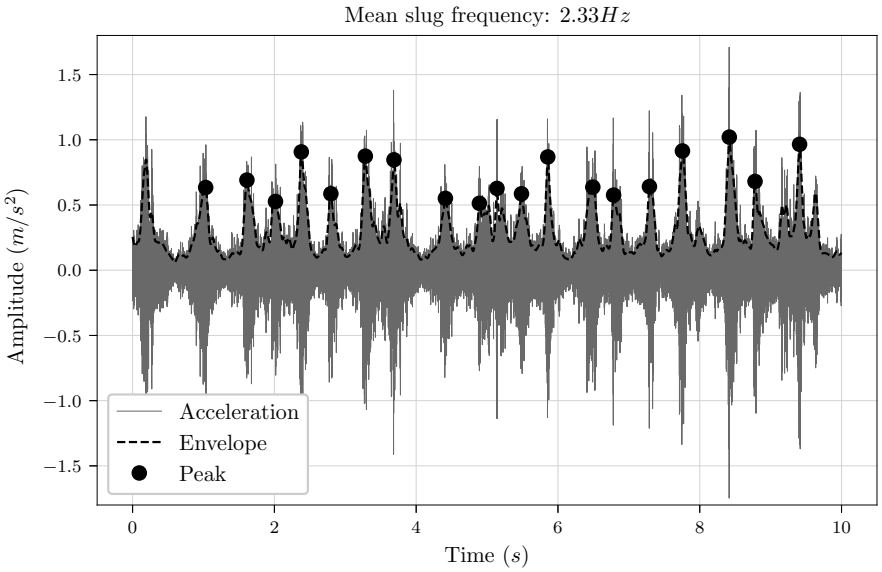

Figure 5.9: 10 s of the filtered vibration signal in the band of interest of the repetition 1 of the acquisition 6 and the filtered modulus of the Hilbert transform of the signal.

signal energy, which was expected. It is perceptible that in a peak of the filtered signal there is a high variation of the amplitudes. Not only in the peaks but also between the peaks, there are some isolated amplitude peaks. This noisy signal poses a problem to peak detection algorithms, which will be challenging to obtain not only peaks with higher amplitudes but peaks with its surroundings with high amplitude. Thus, the usage of the signal envelope may be preferable.

As stated in Section 3.2.2, the signal envelope can be obtained by calculating the modulus of the Hilbert transform. However, by solely using the modulus of the Hilbert transform will be not sufficient. Once, the high amplitude variation of the signal, even in the prominent peaks, will result in a 'noisy' envelope. Thus, to detect exclusively the peaks that have its surroundings also high, the modulus of the Hilbert transform was filtered by a low-pass Butterworth filter of second order. The cut-off frequency was set to 12 Hz by taking account that the peaks are related to the slug frequency. Thus, it is not expected high frequencies. Finally, the cut-off frequency was fine tuned by visually adjusting the filtered envelope to describe the amplitude increase without high oscillations.

However, the Butterworth filter generates a phase shift in the filtered signal. This effect is undesired, once the peak location in time means when the 'Taylor bubble' has passed. Thus, to remove phase shift, the already filtered modulus of the Hilbert transform was flipped and then filtered again by the same low-pass Butterworth filter. Therefore, the modulus of the Hilbert transform of the filtered signal was filtered twice, once forward and once backwards. The envelope of the signal obtained by this procedure are shown as a dashed black line in Figures 5.8 and 5.9.

As the filtered envelope are similar to the signal energy, the observations of the Section 5.3 are in most part extensible to the envelope case. For instance, it is perceptible that the acquisition

6 has considerably higher amplitudes than the acquisition 1. Besides, it is observable, that the turbulent region behind the 'Taylor bubble' is not significantly higher than other structural excitation mechanisms.

The peak detection algorithm used does not require any adjustment or tuning to be able to detect the peaks sucessfully. Thus, with the filtered envelope it was possible to use the peak detection algorithm to detect the peaks, and then compare with the detected with the signal energy. The peaks detected are shown as black dots in Figures 5.8 and 5.9 for the acquisitions 1 and 6 respectively.

In general, the peak detection in both acquisitions was similar for the signal energy and filtered envelope. Furthermore, carefully analysing the filtered vibration signal and the signal energy, it is perceptible a peak around the $5\,\mathrm{s}$ which in both cases the peak detection algorithm did not detected. However, it is noticeable that this peak shape is relatively different from others, where its surroundings are not high. Also, analysing the spectrum, it is not perceptible an increase in all frequencies. Thus, this peak may be correlated with other excitation phenomena rather than the pressure fluctuation.

Once detected the peaks locations in the filtered envelope, the mean slug frequency was calculated as in Section 5.3. The mean slug frequency are shown in Figures 5.8 and 5.9. Contrasting the mean slug frequencies calculated using the filtered envelope with the signal energy, it is observable that for the acquisitions 1 and 6 the mean frequency is not equal. In both acquisitions the difference was of $0.01\,\mathrm{Hz}$ and $0.02\,\mathrm{Hz}$ respectively. In the acquisition 1 the envelope resulted in a higher frequency and the acquisition 6 the envelope resulted in a lower frequency. As the same peaks were detected in both cases, the low number of peaks and their slight position difference, resulted in the difference observed.

As observed and highlighted in the previous sections, the acquisition 25 does not present a distinct activity in the frequency band of $2400\,\mathrm{Hz}$ to $2800\,\mathrm{Hz}$. Therefore, the analysis in the time domain for the acquisition 25, as in the acquisitions 1 and 6, does not result in meaningful analysis. Thus, the same procedure done for the acquisitions 1 and 6 was done in the acquisition 25, to demonstrate that the results of the analysis performed in this section does not present any clear meaning for the acquisition 25. The results are shown in Figure 5.10.

As can be seen in Figure 5.10, there is no significant changes in the filtered signal, which agrees with the observed in Section 5.2. The filtered envelope presents small oscillations along the time. Finally, the peaks detected does not present any clear meaning.

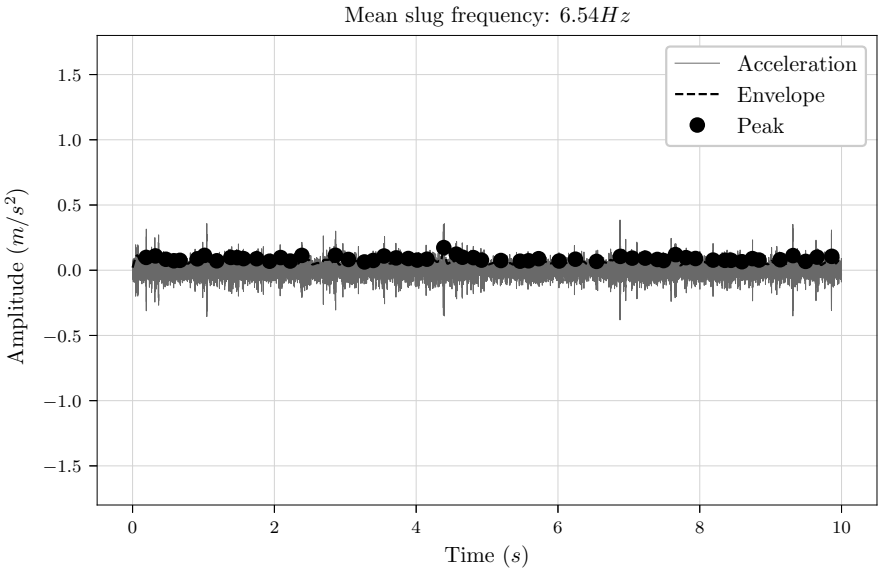

Figure 5.10: $10\,\mathrm{s}$ of the filtered vibration signal in the band of interest of the repetition 1 of the acquisition 25 and the filtered Hilbert transform of the signal.

5.5 Envelope

This section presents the two-phase flow properties calculated by merely using the envelope of the vibration signal, calculated as described in Section 5.4. The subsection 5.5.1 presents the calculation of the slug frequency. The subsection 5.5.2 presents the calculation of the V_{GTB} of the slug flow. The subsection 5.5.3 correlates envelope with the gas void fraction. The subsection 5.5.4 correlates envelope with the flow pattern.

The procedure starts by filtering the vibration signal used with a second order pass-band Butterworth digital filter, and then the modulus of the Hilbert transform of the filtered vibration signal is calculated. The obtained modulus of the Hilbert transform is then low-pass filtered twice, once forward and once backwards, to remove the phase shift of the second order Butterworth digital filter used. The cut-off frequencies of the band-pass filter are $2400\,\mathrm{Hz}$ and $2800\,\mathrm{Hz}$. The cut-off frequency of the low-pass filter is $12\,\mathrm{Hz}$. This procedure and the cut-off frequencies were used in all acquisitions and its repetitions in the following subsections unless otherwise specified. Therefore, the term ‘envelope’ will be used as a synonym of the signal envelope resulting from the described procedure unless otherwise specified.

5.5.1 Slug frequency

The Section 5.4 applied the peak detection algorithm presented in Section 3.5 in the envelope of the acquisitions 1, 6 and 25, to detect the pipe structural response due to an increase in the pressure fluctuation caused by highly turbulent region after the ‘Taylor bubble’. Therefore, it was possible to detect the ‘Taylor bubble’ passage. Finally, by detecting the ‘Taylor bubble’, it was calculated the mean slug frequency by taking the average of the frequencies calculated by

each time interval of the detected ‘Taylor bubbles’. The same procedure was used but for the 30 s of all acquisition and repetitions, including the dispersed bubbles. The dispersed bubble cases were included to analyse the technique behaviour in those cases.

Furthermore, as the vibration measurements were taken at two different points of the pipe, by the vibration measurement station *VIB-201* and *VIB-301*, it is possible to calculate the mean slug frequency separately for each station. Finally, to assess the technique robustness, the slug frequency was averaged between the repetitions of each acquisition, and then it was calculated the standard deviation of the slug frequencies calculated. The averaged mean slug frequency, dot, with its standard deviation, bars, for each acquisition of the station *VIB-201* are presented in Figure 5.11 and for the station *VIB-301* are presented in Figure 5.12. The dashed line refers to the averaged mean slug frequency of the other vibration measurement station respectively. The flow pattern is indicated by the symbols.

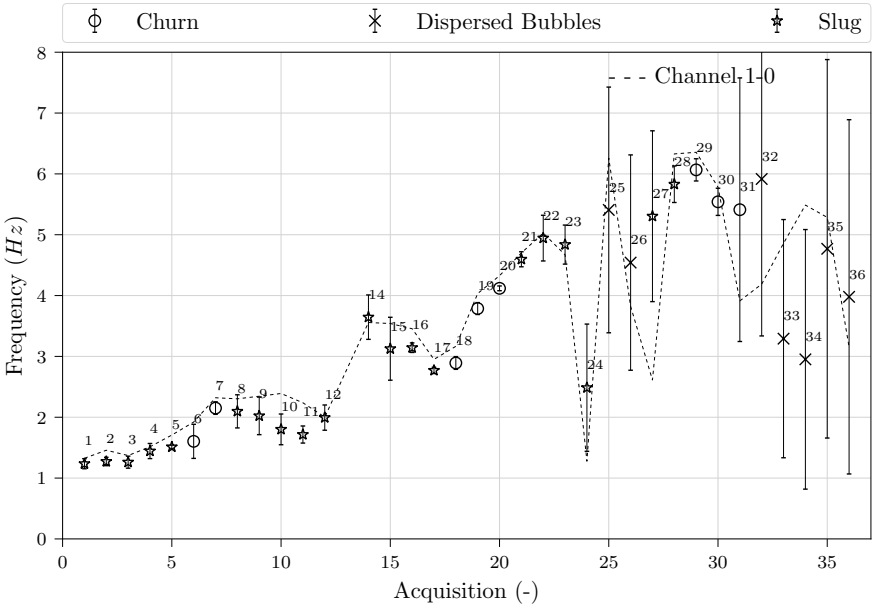

Figure 5.11: Averaged mean slug frequency of the vibration measurement station *VIB-201*, using the channel 0-0.

In general, it can be observed in Figures 5.11 and 5.12, that for both measurement stations the acquisitions from 1 to 22 and the acquisition 28 and 29, presented a considerably low standard deviation between the repetitions. It means that the proposed technique was able to detect the peaks over the different repetitions consistently. However, it is noticeable that for all dispersed bubbles cases, in both measurement stations, the standard deviations were considerably high. This result reinforces the mentioned in Section 5.4, that this technique does not present a clear meaning for the dispersed bubble bubbles flow pattern. On the other hand, the standard deviation between different measurements can be considered as way to detect if the flow pattern is dispersed bubble or not.

In contrast with the lower standard deviation in the acquisitions from 1 to 22, which contains

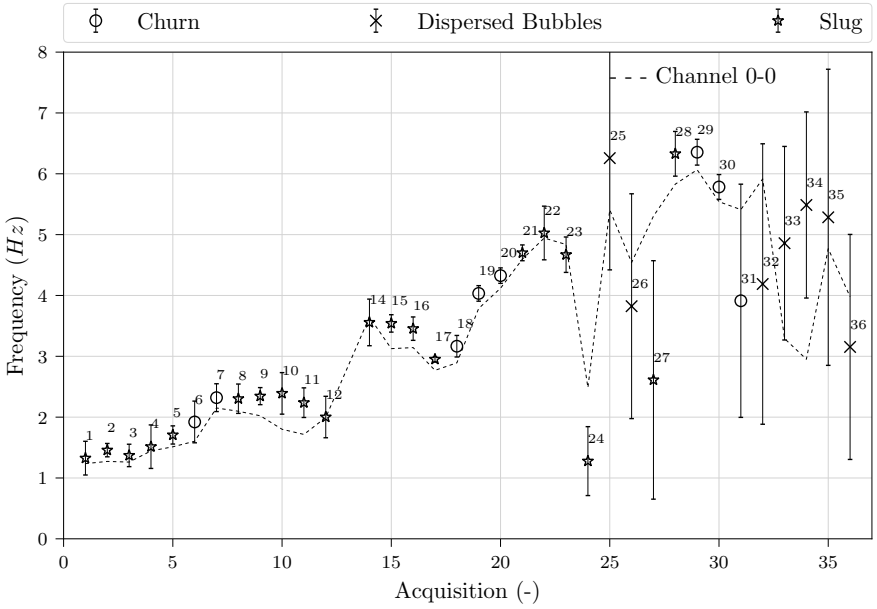

Figure 5.12: Averaged mean slug frequency of the vibration measurement station *VIB-301*, using the channel 1-0.

the solely churn and slug flow patterns, it is perceptible that for the acquisitions 24, 27 and 31, slug and churn flow patterns, the standard deviation of those acquisitions were considerably high. These acquisitions are near the transition region according to the Taitel, Bornea and Dukler [76] criteria. It is possible that this high standard deviation is due to the transition, where for instance for a specific repetition the 30 s it was more a dispersed bubble than a slug or churn flow. However, it is required further investigation to be sure about this affirmation and this will be treated as a limitation.

Analysing the dashed line in Figure 5.12, which is related to the averaged mean slug frequency in the vibration measurement station *VIB-201*, the low standard deviation cases are consistently above the respective point of the station *VIB-201*. This difference may be related to the gas-phase acceleration as the distance between the vibration measurement stations is considerable. Further, this acceleration may affect the velocity calculation which will be developed in the Section 5.5.2.

As mentioned in Section 3.6.5, many of the models available in the literature to predict the slug frequency cover only the horizontal flow, and most of them are based on experimental data. Therefore, it is not possible to use them to estimate the slug frequency of the acquisitions and compare them with the obtained using the peak detection algorithm. Also, in Section 3.6.5 it was mentioned the work of Abdulkadir *et al.* [72] also studied the slug frequency in vertical flows. The authors briefly described the effects of the superficial velocities of the gas and liquid on the slug frequency. Thus, it is presented in Figure 5.13 the averaged mean slug frequency obtained using the channel 1-0, dot, as function of the superficial gas velocity. The symbols are the flow pattern. Due to the high standard deviation, the dispersed bubble cases and the acquisitions 24, 27 and 31 were omitted. Moreover, there is a line for each liquid superficial velocity.

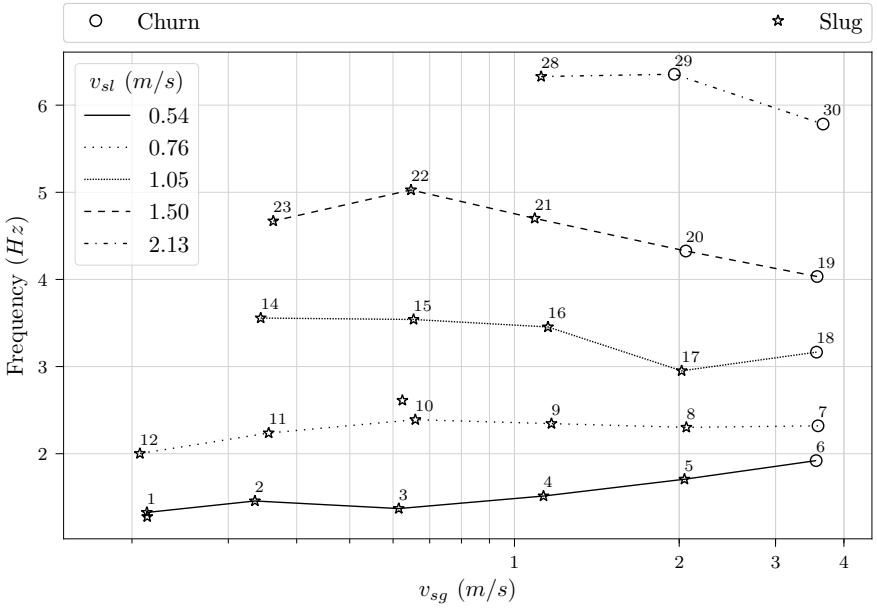

Figure 5.13: Measured slug frequency using the channel 1-0 as function of the gas superficial velocity.

Contrasting the observed by Abdulkadir *et al.* [72] with the Figure 5.13, it is noticeable that for the acquisition with low standard deviation, 1 to 23, the obtained is in agreement with the stated by Abdulkadir *et al.* [72]. The authors observed that for lower liquid superficial velocities the increase of the gas superficial velocity would cause a slight increase in the slug frequency. Thus, observing liquid superficial velocities of $0.54\,\mathrm{m\,s^{-1}}$ and $0.76\,\mathrm{m\,s^{-1}}$, it is perceptible that when the gas superficial velocity was increased the slug frequency also increased.

As mentioned in Section 3.6.5, Abdulkadir *et al.* [72] observed that the significant increase in the slug frequency was caused by the increase of the liquid superficial velocity. This observation is in complete agreement with the presented in Figure 5.13, where it is noticeable that increasing the liquid superficial velocity, the slug frequency increases significantly. It can be observed by the Y-axis offset between the different liquid superficial velocities lines.

Besides, Abdulkadir *et al.* [72] observed that for higher liquid superficial velocities, the slug frequency decreased and then increased as the gas superficial velocity was increased. This pattern is also observed in liquid superficial velocity of $1.05\,\mathrm{m\,s^{-1}}$, as shown in Figure 5.13. Moreover, for the liquid superficial velocities of $1.50\,\mathrm{m\,s^{-1}}$ and $2.13\,\mathrm{m\,s^{-1}}$, it is observable a decrease of the slug frequency with the increase of the gas superficial velocity.

However, analysing the acquisitions 22 and 23 in Figure 5.13, it is noticeable that with the increase of the gas superficial velocity the slug frequency also increased. Nevertheless, this behaviour may be related to the flow pattern transition. As can be observed in the test matrix in Figure 4.11, the acquisitions 22 and 23 are near the flow pattern transition. Besides, the acquisition 24, which was an acquisition with lower superficial gas velocity, presented a high standard deviation. Thus, this behaviour may be related to the flow pattern transition.

Finally, instead of assessing the slug frequency qualitatively as discussed previously. It was tried to extract the slug frequency from the recorded videos. The approach used was to detect the change in the image brightness and associate it with the slug frequency. The change in the image brightness due to the 'Taylor bubble' passage motivated it. However, the approach was successful only for a few acquisitions, with low gas and liquid superficial velocity. Due to the low number of acquisitions, the comparison with the peak detection approach would not result in meaningful analysis. Therefore, to assess the accuracy of the slug frequency obtained, it would be necessary other sensors that are capable of measuring the slug frequency and then compare.

5.5.2 Velocity estimation

It was mentioned in Section 5.2.1 that if the frequencies from $2400\,\mathrm{Hz}$ to $2800\,\mathrm{Hz}$ would have a high attenuation along the pipe, it would be possible to calculate the V_{GTB} of the slug flow through cross-correlation. The velocity V_{GTB} is highlighted in Figure 3.2 of Section 3.6.4. According to the discussed in Section 3.4.1, the cross-correlation can estimate the time delay between two signals. It gets the time delay whose the correlation of the signals is the highest. Thus, as the distance between of the two vibration measurement station is known, it is possible to calculate the indicated velocity.

As mentioned in Section 3.6.5, the V_{TB} is a closure relationship for the Taitel and Barnea [66] model. Thus, this is a valuable information to characterise the two-phase flow. Besides, the 'Taylor bubble' expansion and therefore the difference between the V_{TB} and V_{GTB} is not significant when compared to the V_{TB} order. Consequently, the V_{GTB} is approximately the V_{TB}. However, it was mentioned in Section 5.5.1 that the differences between the mean slug frequencies obtained by the two vibration measurement station were related to the gas-phase acceleration. Thus, despite the gas-phase acceleration observed, in this subsection the calculated velocity will be considered as the V_{TB}. Once there are a set of correlations, presented in Section 3.6.5, that can be used to obtain the V_{TB}. Therefore, in this subsection, they will be used to compare the calculated V_{TB} with the presented literature correlations and analyse if the acceleration observed influenced the results.

As mentioned in Section 5.4 and observed in Figures 5.8 and 5.9, the filtered vibration signal has high amplitude variations in the peaks regions, and even the peaks are considerably different from each other. Those variations pose a problem to use the peak detection algorithms and to contour it the envelope was calculated and then it was possible to detect the peaks successfully. Besides, those variations can also be a problem for the cross-correlation. It is possible that the highest correlation between the two vibration measurement station, be a delay whose a 'true' peak is correlated with 'undesired' peak, due to the correlation formula. An 'undesired' peak, for instance, is the single peak mentioned in the signal energy in Section 5.3, which differently from the other peaks had a solely high amplitude.

Thus, the cross-correlation between the two vibration measurement station was applied to the

envelope, not to the filtered vibration signal. Then, the envelope for the two measurement station of all the acquisitions and its corresponding repetitions were calculated. Once calculated the envelope, it was measured the time delay between the envelope of the two vibration measurement stations using the cross-correlation. Then, it was possible to determine the velocity. Similarly to the mean slug frequency in Section 5.5.1, the velocity was averaged between the acquisition repetitions and the standard deviation between the repetitions was also calculated. The results are presented in Figure 5.14, where the cross-correlation V_{TB} is presented as a function of the mixture velocity. The dots are the averaged calculated velocity, the bars are the standard deviation, and the symbols are the flow pattern. Finally, the dashed line is the mixture velocity.

Moreover, during the cross-correlation implementation, it was observed that in some cases the highest correlation point resulted in extremely high velocities, up to $50\,\mathrm{m\,s^{-1}}$, when compared to the velocities used. It is known that those velocities do not represent the reality. Thus, the highest correlation point was got from the delays interval that represents the velocity interval of $10\,\mathrm{m\,s^{-1}}$ to $0.1\,\mathrm{m\,s^{-1}}$ to avoid this error. The cross-correlation was applied to $30\,\mathrm{s}$ of measurement. To be able to analyse the behaviour of this technique along with all flow patterns, the Figure 5.14 also presents the results of the cross-correlation for the dispersed bubbles case. Despite the expected velocity to be obtained through cross-correlation in the slug and churn flow cases be the V_{TB}.

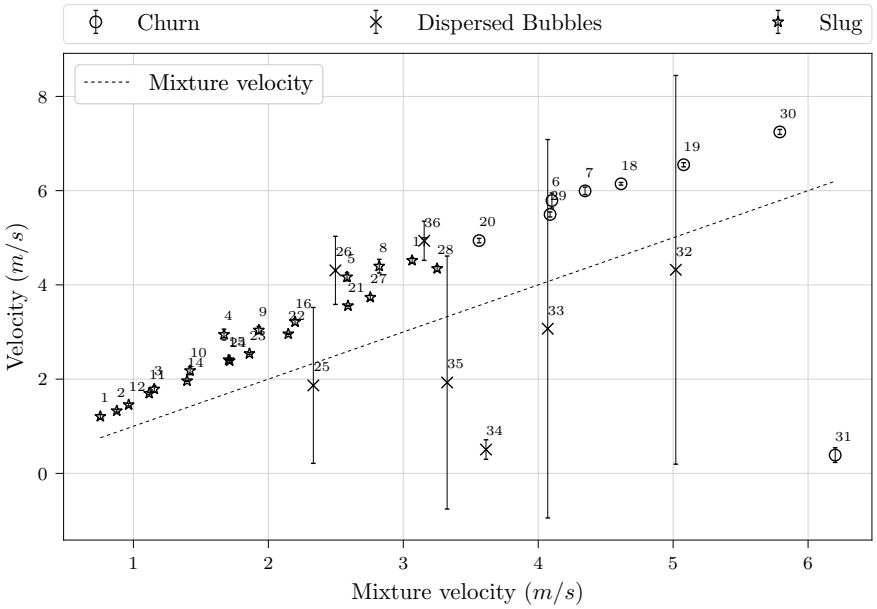

Figure 5.14: V_{TB} calculated with cross-correlation between the vibration measurement stations as function of the mixture velocity.

It is noticeable in Figure 5.14 that for the slug and churn flow cases, the standard deviation of calculated velocity between the repetitions of the acquisitions was relatively small. In some cases, the standard deviation bars are even smaller than the symbol, which is difficult to assess the standard deviation in those cases. It is relevant to observe that despite the acquisition 31 be classified as a churn flow and have a low standard deviation, the mean calculated velocity was of

$0.3879\,\mathrm{m\,s^{-1}}$ which is considerably different from the other churn flow cases.

Furthermore, it is perceptible that for most of the dispersed bubble cases, the standard deviation was considerably high. These results are in agreement with the observed in Section 5.4, where for the acquisition 25, the envelope presented did not have any distinct characteristic, just small oscillations. Thus, it is more difficult to align the signals. It can be addressed by changing the cut-off frequency of the low-pass filter of the modulus of the Hilbert transform.

However, another possible reason is the distance between the stations. As it is considerable, the flow may have changed between the stations and thus the structural response. Therefore, the cross-correlation between the signals leads to wrong results. Thus, by placing the vibration station closer to each other, it may be possible to estimate the flow velocity.

Differently, from the other churn flow cases, the acquisition 31 presented a value considerably different from the mixture velocity, dashed line. Furthermore, analysing the test matrix it is noticeable that according to the Taitel, Bornea and Dukler [76] criteria, this point would be classified as dispersed bubbles despite being classified visually as churn flow. Nevertheless, this acquisition is close to the transition region between churn flow to dispersed bubbles. Therefore, it is difficult to classify it correctly. Thus, it is not surprising that the results obtained were different from the other churn flow cases.

Similarly to the acquisition 31, the acquisition 34, a dispersed bubble case, also had a small standard deviation and a mean velocity close to the acquisition 31. In those cases, it is possible that due to the chosen cut-off frequency in the low-pass filter of the envelope, the absence of distinct signal characteristics and the velocity limits favoured obtaining a velocity that does not seem to match any of the two-phase flow velocities. Thus, it reinforces that this configuration of transducer distance and envelope cut-off frequency is not appropriate to analyse dispersed bubbles cases.

Despite presenting a systematic error in Y-axis, it is observable in Figure 5.14 that the calculated velocities, with low standard deviation, are consistent with the mixture velocity. However, as mentioned in Section 3.6.4, according to Shoham [2] the velocity distribution in slug flows are $V_{TB} > V_{GTB} > V_{GLS} > V_{LLS} > V_{LTB}$. Thus, as the calculated velocity is closer to the V_{TB}, it is expected that the calculated velocity is higher than the mixture velocity.

As mentioned above and presented in Section 3.6.5, there are different models in the literature that it is possible to estimate the V_{TB}. Therefore, it is more appropriate to compare the results of those models with the calculated V_{TB} with the envelope. As the results of the dispersed bubbles cases and the acquisition 31 pointed towards the idea that to obtain a meaningful result require a modification in the transducer positioning, the results of the dispersed bubbles cases will not be compared to any literature model or correlation. Therefore, in the next analysis in this subsection, the acquisitions with dispersed bubbles case will be not considered. The acquisition 31 will be maintained to show that the results obtained for this case does not represent the V_{TB} and enforce that this acquisition is in the flow pattern transition region.

Similarly, the both calculated velocity and the correlations velocity were averaged between

the acquisition repetitions and the standard deviation between the repetitions was also calculated. The 'Taylor bubble' velocity was calculated using the five correlations presented in Section 3.6.5.

The results are presented in Figure 5.15, where the cross-correlation V_{TB} is presented as a function of the different correlations. Thus, the X-axis is the V_{TB} calculated with literature correlations, and the Y-axis is V_{TB} calculated with the cross-correlation. The dashed lines are a $\pm 10\,\%$ relative error, and the spaced dashed lines are a $\pm 20\,\%$ relative error. The solid line is the identity function. The dots represent the averaged calculated velocity, and the symbols are the different correlations. The standard deviation deviation bars were omitted to be improve the graph readability and due to their small values. It is important to note that the Nicklin, Wilkes and Davidson [67], Bendiksen [68] and Théron [70] correlations presented similar values for all of the acquisitions and their symbols are overlapping.

The calculated velocities are presented in Appendix C.

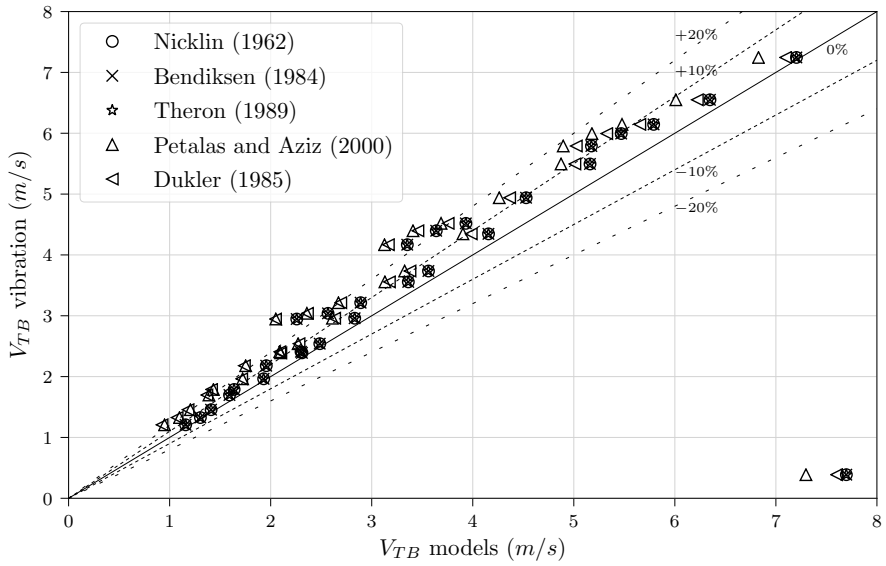

Figure 5.15: V_{TB} calculated with cross-correlation as function of the V_{TB} calculated with current available correlations in the literature.

In accordance with the observed previously in Figure 5.14, the velocity obtained for the acquisition 31 does not represent the V_{TB}. Once the value obtained was significantly different for all correlations and does not match with the expected. It was expected to be at least similar to the acquisition 30. Thus, this acquisition will be not considered in the following analysis.

It is noticeable in Figure 5.15 that in general, the obtained V_{TB} presented a reasonable accuracy, where they follow the trend of the V_{TB} calculated using the correlations. Once, when they increased the cross-correlation velocity also increased. Besides, the highest errors are from a few acquisitions with velocities near $3.5\,\mathrm{m\,s^{-1}}$ and $2\,\mathrm{m\,s^{-1}}$. These acquisitions and correlations presented errors higher than $20\,\%$, which is higher than the average error of the correlations, as stated in Section 3.6.5. It is also observable that the standard deviation between the repetitions for the different correlations were low, once their horizontal standard deviation bars in all cases

are difficult to distinguish and they are inside the correlations symbols.

It is perceptible in Figure 5.15 that when considering all correlations, in general, there is an slope error. The slope error can be better observed if the dashed line of $10\,\%$ were the identity line. In this case, most of the acquisitions and correlations would be inside of an envelope of error of $\pm 10\,\%$, and a few cases would have error higher than $\pm 20\,\%$. Moreover, the slope error can also be verified due to the error of all acquisitions and correlations be a 'positive' error. In other words, the cross-correlation velocity obtained velocities that are higher than the predicted velocities of the correlations.

It is notable in Figure 5.15 that the first three correlations, the correlation of Nicklin, Wilkes and Davidson [67], Bendiksen [68] and Théron [70] presented similar values for all of the acquisitions. Moreover, for those correlations the cross-correlation presented the lowest errors, where most of them have an error lower than $10\,\%$. Besides, 12 acquisitions or $44\,\%$ of the points presented errors lower than $5\,\%$. For instance, these acquisitions can be observed in Figure 5.15 with velocities near $1\,\mathrm{m\,s^{-1}}$, $2\,\mathrm{m\,s^{-1}}$ and $7\,\mathrm{m\,s^{-1}}$.

On the other hand, those three correlations presented only three acquisitions with an error higher than $20\,\%$, with errors of approximately $30.5\,\%$, $24.3\,\%$ and $20.8\,\%$. The cases with errors higher than $20\,\%$ are the same as mentioned previously. However, observing these cases, it is perceptible that for near velocities in the correlations, the cross-correlation presented errors from lower than $5\,\%$ and higher than $20\,\%$. As the standard deviation between the repetitions were low and it occurred for more than one case, to assess those points more accurately it is required, for instance, another technique that is also capable of measuring the V_{TB}. Thus, it would be possible to verify the results with more certainty.

It is perceptible in Figure 5.15 that the last two correlations, the correlation of Petalas and Aziz [71] and Dukler, Moalem Maron and Brauner [69] presented similar values for acquisitions with lower V_{TB} velocities, and as the velocity increased the difference also increased. It can be observed by comparing the velocity near $1\,\mathrm{m\,s^{-1}}$ and near $7\,\mathrm{m\,s^{-1}}$. In the first case, the symbols of these models are overlapping. In the second case, the symbols presented a reasonable difference. Moreover, for those correlations, the cross-correlation presented the highest errors, where most of them have an error higher than $10\,\%$.

In the correlations of Petalas and Aziz [71] and Dukler, Moalem Maron and Brauner [69] the previously mentioned slope error is more apparent. Besides, in these correlations, most of the acquisitions presented an error higher than $10\,\%$. Also, most of the points with the error higher than $20\,\%$ were from these correlations. If it were considered the dashed line of $10\,\%$ as the identity line for these correlations, all of the acquisitions would be inside an error of $\pm 20\,\%$, and most of them would have an error lower than $\pm 10\,\%$.

On the other hand, as mentioned above, in this subsection the V_{GTB} would be considered approximately the V_{TB}. Then, the velocity obtained by the cross-correlation would be considered the V_{TB} instead of the V_{GTB}, once there are many available correlations for the V_{TB}. Then, it would be possible to compare and contrast the results obtained by the cross-correlation with

the literature correlations. However, as mentioned above, the cross-correlation appears to have, an slope error, where the cross-correlation is, in most of the acquisitions and correlations, getting velocities systematically higher than the correlations. This difference is against what was assumed, once the expected was to be slightly lower or approximately equal to the V_{TB}. Thus, the difference may be

Moreover, as mentioned, for near velocities in the correlations model the cross-correlation obtained velocities dramatically different. Thus, although the correlations indicated that the cross-correlation is capable of measuring the V_{TB} with reasonable accuracy, it is required another measurement system that is also capable of measuring the V_{TB}, to be able to assess more accurately and investigate the possible issues of the proposed technique.

5.5.3 Gas void fraction correlation

To date, it was not found any study that correlates the envelope of a filtered vibration signal with the GVF of the two-phase flow. Thus, as an exploratory approach, a relationship was sought between the envelope and the GVF. As a start point, the first four statistical moments of the $30\,\mathrm{s}$ of measurement were tried. Then, it was found an apparent quadratic relationship between the standard deviation of the envelope and the GVF for the dispersed bubbles and churn flow.

For the slug flow, the relationship was not apparent as the other flow patterns. Therefore, after some adjustments in the envelope calculation, it was found that if the cut-off frequency of the low-pass filter of the modulus of the Hilbert transform were increased, the quadratic fit improved. Thus, adjusting the cut-off frequency, it was found that the cut-off frequency of $50\,\mathrm{Hz}$ presented the best quadratic fit.

As mentioned in Section 4.1, the fast-closing system has a limitation in the GVF that can be measured, which is from $6.2\,\%$ to $93.8\,\%$. Therefore, the acquisitions which presented GVF lower and higher than fast-closing system limits were removed due to reliability issues. These acquisitions will be not used to fit the curves. To fit the curves, it was used the mean of the GVF between the repetitions and the mean of the standard deviation of the envelope with the higher cut-off frequency between the repetitions. The usage of the mean instead of the values of each repetition is due to the high standard deviation of the GVF measured by the fast-closing system, particularly to the slug flow cases.

Despite to apparently be a quadratic fit, it was fitted the linear, quadratic, cubic, logarithm and exponential functions. However, the quadratic and cubic presented the highest and similar coefficient of determination, R^2. The coefficient of determination of the tested functions is presented in Table 5.1.

Table 5.1: R^2 of linear, quadratic, cubic, logarithm and exponential fits using the mean GVF.

Linear	Quadratic	Cubic	Logarithm	Exponential
0.78	0.93	0.93	0.89	0.64

Finally, in Figure 5.16 the quadratic trend is shown with the quadratic fit, dashed line. The dots are the acquisitions. The vertical bars are the standard deviation of the GVF measured along the repetitions. The horizontal bars are the standard deviation of the envelope standard deviation along the repetitions. The symbols are the flow pattern. The acquisition number is presented next to the dots. The R^2 and the curve coefficients for the fitted curve are also shown.

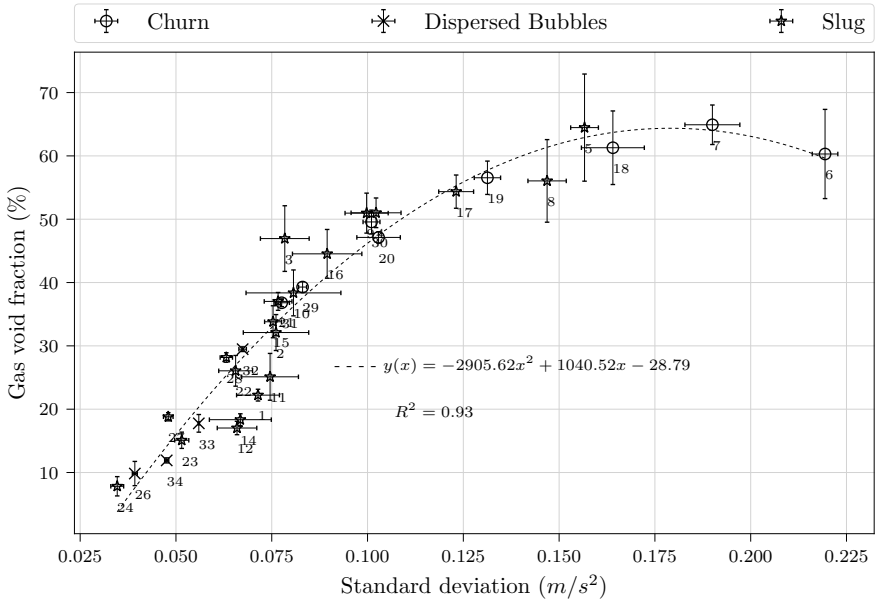

Figure 5.16: GVF as function of the standard deviation of the envelope with cut-off frequency of $50\,\mathrm{Hz}$.

The fit performance can be better observed in Figure 5.17, where the predicted GVF is presented as a function of the GVF measured. Thus, the X-axis is the measured GVF, and the Y-axis is the predicted GVF. The dashed lines are a $\pm 10\,\%$ error, and the spaced dashed lines are a $\pm 20\,\%$ error. The solid line is the identity function.

It is noticeable in Figure 5.17 that from the 32 points analysed only 8 presented an error higher than $\pm 20\,\%$. Moreover, seven of those points are acquisitions with slug flow and one of them is dispersed bubbles. However, this dispersed bubbles point and the acquisition 24 are relatively close to the identity function. In this case, the high percentage error occurs when the GVF values get smaller, where small quantitative errors translate to high percentage error. Contrasting the slug flows points that presented errors higher than $\pm 20\,\%$ with the Figure 5.16, it possible to note that those points presented are further from the fitted curve.

Furthermore, observing the standard deviation between the repetitions of the envelope standard deviation, in the Figure 5.16, of the points with the error higher than the $\pm 20\,\%$, observed in Figure 5.17, it is perceptible that they presented a high standard deviation. Moreover, by contrasting the points that presented a high standard deviation and error higher than $\pm 20\,\%$ with the mixture Reynolds number presented in Figure 5.1, it is noticeable that the points with high error and high standard deviation have the lowest mixture Reynolds number. Thus, it is

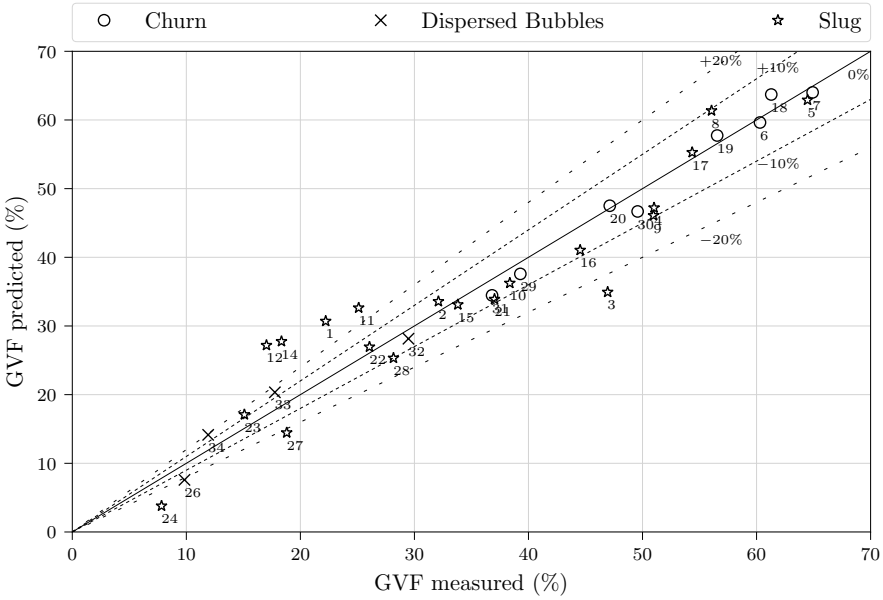

Figure 5.17: Predicted GVF as fucntion of the measured GVF.

possible that the relationship between the GVF and the standard deviation is more appropriate to higher mixture Reynolds number cases. Moreover, as can be seen in Figure 5.17, all churn flow acquisitions and most of the slug flow acquisitions, that the error was not higher than $\pm 20\,\%$, are inside the $\pm 10\,\%$ margin.

As the relationship between the GVF and the standard deviation is possibly more appropriate to higher mixture Reynolds number, to evaluate the fit performance, the acquisitions with mixture Reynolds number equal or lower than the mixture Reynolds number of the acquisition 14 were removed. The acquisitions removed according to this criterion were 1, 2, 3, 10, 11, 12 and 14. Thus, there are 25 acquisitions that have GVF from $6.2\,\%$ to $93.8\,\%$ and mixture Reynolds number higher than the acquisition 14.

Despite the number of acquisitions that meet the established criteria, 25 acquisitions, to fit a quadratic curve is required at least three points. However, fitting a quadratic curve with only three points may result in an overfitted model. It was used the mean of the GVF between the repetitions and the mean of the standard deviation of the envelope with the higher cut-off frequency between the repetitions to fit the curves. Therefore, it was determined to use six acquisitions to fit the model and the remaining 19 acquisitions used to evaluate the fit performance.

A curve fit is sensitive to data extrapolation. Thus, a set of criteria were established to select the acquisitions that would be used to fit the quadratic curve. The first criterion was the maximum and minimum values of the standard deviation of the envelope. By following this criterion the acquisitions 6 and 24 were selected. The second criterion was the maximum and minimum values of the GVF, which led to the choice of acquisitions 7 and 24.

The third criterion was the highest mixture Reynolds number. Then, the acquisition 31 was selected. The fourth criterion was the mid-point between the maximum and minimum of the

standard deviation of the envelope. Therefore, the acquisition 17 was selected. Finally, the acquisitions already selected were a slug and churn flow. Thus the sixth acquisition was set to be the acquisition 34, which is a dispersed bubble case. The acquisition 26 was also considered. However, it has a GVF and mixture Reynolds number close to the acquisition 24.

Finally, in Figure 5.18 the quadratic fit and the selected acquisitions are shown. The dots are the acquisitions. The vertical bars are the standard deviation of the GVF measured along the repetitions. The horizontal bars are the standard deviation of the envelope standard deviation along the repetitions. The symbols are the flow pattern. The acquisition number is presented next to the dots. The R^2 and the curve coefficients for the fitted curve are also shown.

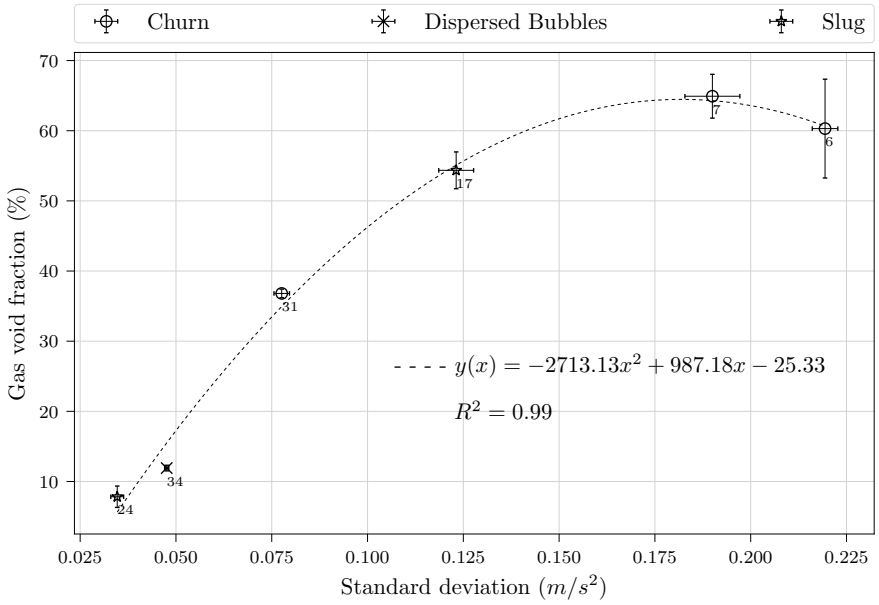

Figure 5.18: GVF as function of the standard deviation of the envelope with cut-off frequency of 50 Hz of the selected acquisitions.

As can be observed in Figure 5.18, the R^2 of the fitted curve increase dramatically. However, this increase need to be interpreted with caution as the number of points used to fit were low. Moreover, comparing polynomial coefficients presented in the Figure 5.16 and in the Figure 5.18, it is noticeable that the polynomial coefficients did not change considerably. Thus, it is expected a reasonable performance of this fit with the other acquisitions.

The GVF of the remaining 19 acquisitions were calculated using the quadratic fit presented in the Figure 5.18 to evaluate the performance of this fit. The calculated GVF is presented as a function of the GVF measured in Figure 5.19. Thus, the X-axis is the measured GVF, and the Y-axis is the predicted GVF. The dashed lines are a $\pm 10\,\%$ error, and the spaced dashed lines are a $\pm 20\,\%$ error. The solid line is the identity function.

It is noticeable in Figure 5.19 that all acquisitions presented an error lower than $\pm 20\,\%$. The acquisitions with higher error were the 23, 33 and 27 with errors of $18.99\,\%$, $17.61\,\%$ and $17.07\,\%$ respectively. The remaining acquisitions presented errors lower than $\pm 10\,\%$. The coefficient of

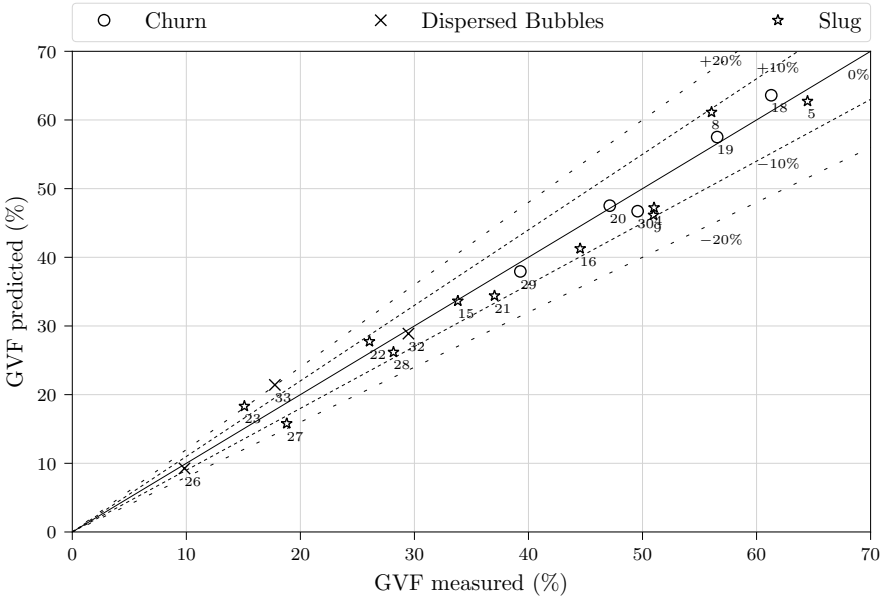

Figure 5.19: Predicted GVF as fucntion of the measured GVF of the selected acquisitions.

determination, R^2, obtained using the remaining acquisitions is 0.97. The performance of the quadratic fit indicates that the use of the acquisitions 6, 7, 17, 24, 31 and 34 was adequate. The effect of overfitting due to the small number of acquisitions used to fit was not significant. Once the points with a higher error also presented a high error when all the acquisitions were used to fit a quadratic curve. It can be observed by analysing the error of the acquisitions 23, 33 and 27 in Figure 5.17

Moreover, the quadratic fit performed reasonably well despite being fitted using a small number of acquisition, when the 'low' mixture Reynolds number acquisitions were removed. It enforces the observed previously, where it was mentioned that it was possible that the relationship between the GVF and standard deviation be appropriate to higher mixture Reynolds number cases. However, it is required a further study in this relationship to be able to have a more conclusive affirmation. Thus, with more acquisitions near the mixture Reynolds number of the acquisition 14, it would be possible to investigate more accurately this relationship.

Besides, due to the limits of the fast-closing system several dispersed bubbles acquisitions were removed, once their measured GVF was not reliable. Also, one dispersed bubble acquisition was used to fit the quadratic curve. Therefore, only three acquisitions of dispersed bubbles were evaluated and one of them, acquisition 33, presented a high error. Thus, to assess more accurately if the quadratic relationship is also valid for the dispersed bubble case it required to measure more dispersed bubble points.

Furthermore, with more points of the dispersed bubble and churn flow, it would be possible to investigate the curve fit for each pattern separately and compare the performance with the quadratic trend observed and also obtain a more accurate quadratic fit.

5.5.4 Flow pattern identification

In the Section 5.2.1, a clear difference between the spectrograms of the different flow patterns was observed. In slug and churn flow patterns, there was a considerable variation of the amplitudes of the frequencies from $2400\,\mathrm{Hz}$ to $2800\,\mathrm{Hz}$ which was not present in the dispersed bubble flow. Furthermore, in Section 5.4 the same difference was clearly observed in the envelope of the acquisitions 1, 6 and 25. Thus, it is possible to use both spectrogram and envelope, to develop an algorithm that is capable to at least classify the flow, for instance, into dispersed bubble or churn and slug flow. The usage of the envelope was preferable, as the envelope calculation is cheap computationally.

Thus, analysing the envelope for the different acquisitions and their repetitions. It was observed that the envelope for churn flow cases were the ones that had the highest amplitude when compared with the other flow patterns. Therefore, the RMS of each acquisition and repetition were calculated. Then, it was possible to set a threshold of $0.28\,\mathrm{m\,s^{-2}}$, which divides most of the churn flow cases from other patterns. The RMS of the envelope of the 140 acquisitions is presented in Figure 5.20. The dots are the acquisitions. The symbols are the flow pattern, and the dashed line is the threshold that determines if the flow pattern is the churn flow or not.

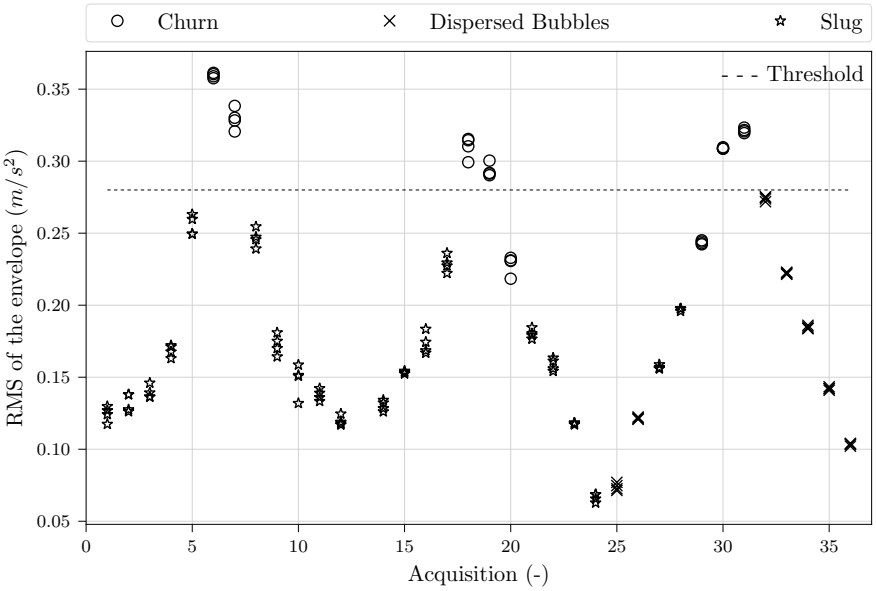

Figure 5.20: RMS of the envelope of all acquisitions.

As can be observed in Figure 5.20, the acquisitions 20 and 29 were improperly classified as a slug flow or dispersed bubble. If the threshold were adjusted to lower values to classify those acquisitions as churn flow, consequently the acquisitions 5, 8, 17, 31 and 32 would be wrongly classified as churn flow. Although the performance was not ideal, this threshold is capable of distinguishing 24 of 32 churn flow cases.

Moreover, when analysing the envelope with different cut-off frequencies for the GVF correlation in Section 5.5.3, it was observed that despite changes in the cut-off frequency, the

general envelope shape for the acquisitions classified as a slug and churn flow did not change dramatically as the shape of the dispersed bubbles cases. Also, in Section 3.4 was asserted that it is possible to measure the degree of similarity of the signal with autocorrelation.

Thus, using the Pearson correlation, with the envelope with different cut-off frequencies and a threshold of 0.701, it was possible to separate most of the dispersed bubble cases from the slug and churn flow cases. The Pearson correlation coefficients of the envelope of the 140 acquisitions are exhibited in the Figure 5.21. The dots are the acquisitions. The symbols are the flow pattern, and the dashed line is the threshold that determines if the flow pattern is dispersed bubbles or not.

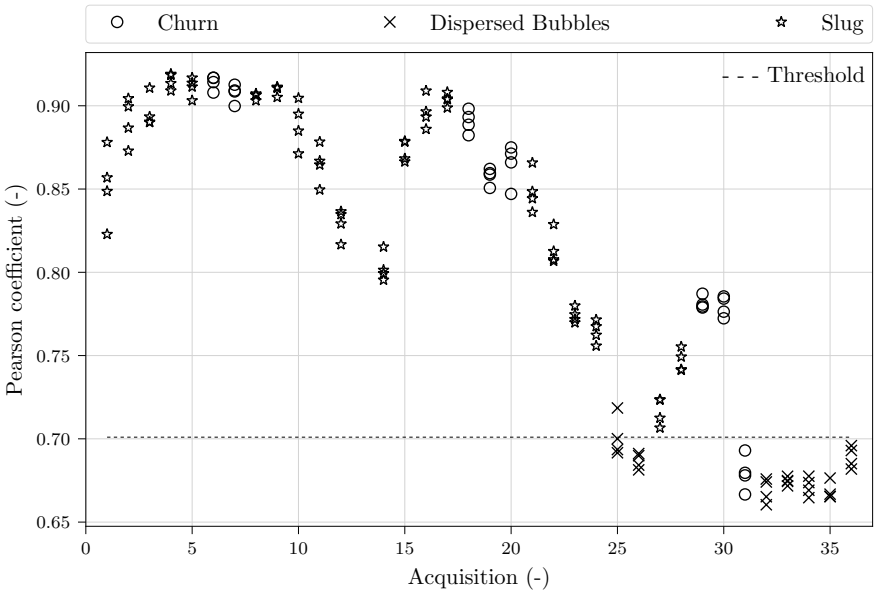

Figure 5.21: Pearson correlation of all acquisitions.

As can be observed in Figure 5.21, the acquisition 31 were wrongly classified as a dispersed bubble and one repetition of the acquisition 25 were wrongly classified as a slug or churn flow. Although, by using the RMS of the envelope associated with the Pearson correlation coefficient, it is possible to avoid the inaccurately classified acquisition 31. On the other hand, if the threshold were higher two repetitions of the acquisition 27 would be incorrectly classified.

Firstly, the point is classified if it is a churn flow or not using the RMS criterion. If it is not a churn flow, the point is then classified if it is dispersed bubble or not using the Pearson correlation criterion. Therefore, as the acquisition 31 is classified as a churn flow by the RMS criterion, it will be not incorrectly classified by the Pearson correlation coefficient. It can be observed in Figure 5.22, where the Pearson correlation and RMS are the X-axis and Y-axis respectively. The symbols are the flow pattern classified visually, and the indicated dashed lines are the threshold mentioned above. The flow pattern regions are also indicated.

The confusion matrix of pattern classification using the criteria used is presented in Figure 5.23. The confusion matrix is a common tool used to present the performance of classification algorithms. It indicates how the points were improperly classified by organising the true and

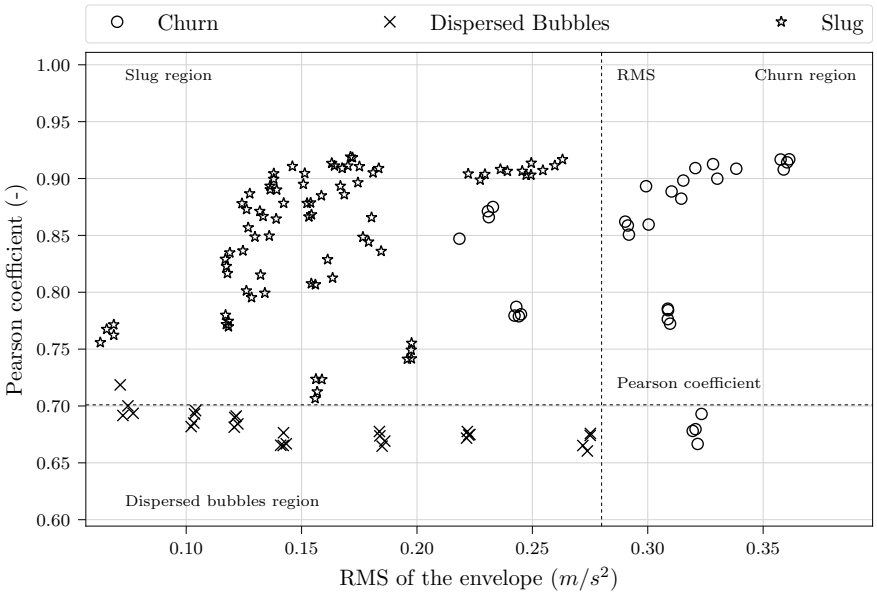

Figure 5.22: Pearson correlation and RMS of all acquisitions.

predicted labels in a matrix. The columns are the predicted labels and the rows are the true labels. In this context, the columns are the predicted flow pattern using the algorithm developed, and the rows are the flow pattern visually determined. The confusion matrix is set in a way that the matrix diagonal indicate how many points were correctly classified. Hence, a hypothetical algorithm that can determine the flow pattern accurately will result in an identity matrix.

The other confusion matrix elements indicate how the flow pattern was wrongly classified. For instance, in Figure 5.23 the first row of the column 'Slug' indicates the number of points that were classified as slug flow by the algorithm, but the true classification was a churn flow. Also, in the second row of the column 'Slug' indicates the number of points that were classified as slug flow, but the correct classification was dispersed bubbles.

It is noticeable that the criteria developed were able to classify accurately $93.57\,\%$ of the points. The incorrectly detected acquisitions were mistakenly classified as a slug flow while it was a churn flow and dispersed bubble. The wrongly classified points, in the churn flow case, are the commented ones while analysing the envelope RMS performance. The wrongly classified point, in the dispersed bubble case, is the repetition of the acquisition 25.

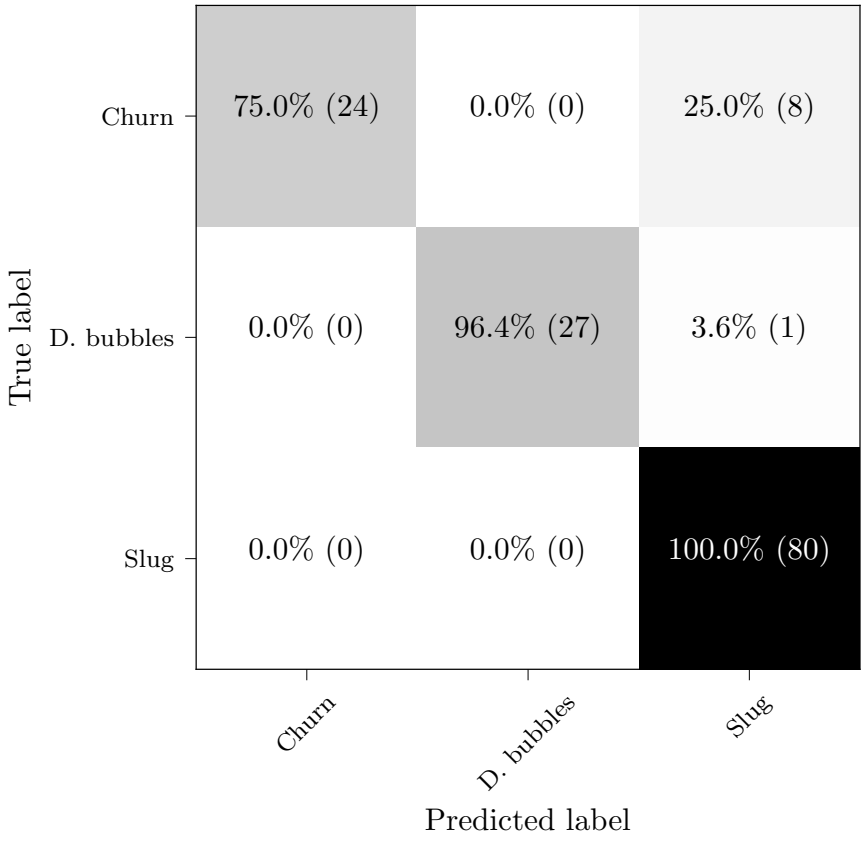

Figure 5.23: Confusion matrix of the flow pattern classification algorithm.

5.6 Other tests

This section presents additional tests performed on the experimental apparatus using the tools discussed in previous sections. For the following tests, the transducers positioning was modified. The new positioning aimed to place the transducers closer to the visualisation section. Moreover, instead of measuring the vibration in different planes, the four transducers were now placed in the same plane. They were spaced irregularly along the tube, to be able to assess the distance that the cross-correlation can obtain a more accurate result. Besides, with the transducers closer to the visualisation section it was easier to synchronise the flow filming with the vibration signal.

The first transducer was placed $0.48\,\mathrm{m}$ from the first pneumatic valve. Then, the second transducer was placed $0.175\,\mathrm{m}$ from the first transducer. The third transducer was placed $0.505\,\mathrm{m}$ from the second transducer. Finally, the fourth transducer was placed $0.973\,\mathrm{m}$ from the third transducer.

The first subsection presents a test with an elongated bubble rising in a stagnant liquid. The second subsection presents a single-phase flow case with the highest liquid velocity obtained. The elongated bubble rising in a stagnant liquid test aims to verify if the turbulence behind the 'Taylor bubble' can indeed induce a significant vibration, which is distinguishable from the other source of vibration and noise. The second subsection presents some analysis of the output flow

from the progressive cavity pump.

5.6.1 Drift velocity

According to Shoham [2], the drift velocity of a phase is the velocity of the phase relative to a surface moving at the mixture velocity. In the stagnant liquid, the drift velocity is the 'Taylor bubble' rise velocity [2]. As stated in Section 3.6.5, many correlations aims to predict the translational velocity of the 'Taylor bubble'. Moreover, most of the presented correlations used a linear superposition of the elongated bubble in stagnant liquid with the influence of the moving liquid, as shown in Equation 3.45.

To be able to calculate the 'Taylor bubble' rising velocity a new experimental procedure was elaborated. In this new procedure, the pump was switched off, and the liquid bypass line was closed. Then, the gas block valve was closed, the *FCV-101* was opened, and the gas line pressure was adjusted. The fast-closing system was deactivated. Thus, the volume of the bubble was not measured. The acquisition of the data and the video was started by observing a differential pressure transducer that was placed just below the fast-closing system. Hence, as the differential pressure transducer signal changed considerably, the acquisitions were started. Finally, the 'Taylor bubble' was generated by quickly manually opening and then closing the gas block valve.

The procedure mentioned above was repeated four times. Then, it was calculated the STFT of the vibration signal of the first transducer, and it is presented in Figure 5.24. The STFT was set with the same parameters used in Section 5.2.1. The spectrogram presented uses a logarithm scale. The grayscale used, the points with higher amplitudes are darker, and the points with lower amplitudes are the lighter points. Moreover, the grayscale limits are the lower and higher amplitudes observed.

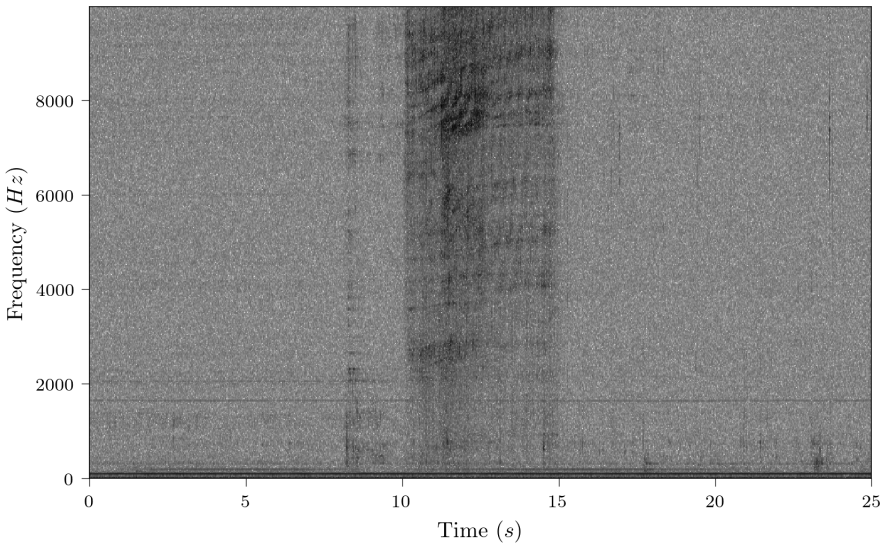

Figure 5.24: STFT of 25 s of the elongated bubble rising.

Analysing the vibration spectrogram in Figure 5.24, it is noticeable that for the time before

the seventh second, there is no perceptible distinct amplitude variation. The spectrogram in this time interval appears to be uniform. Then, after the seventh second, it is observable a slight increase in all frequencies. Next, approximately in the tenth second, there is a considerable increase in the all frequencies mostly in frequencies above the $2000\,\mathrm{Hz}$ and this increase lasts for approximately $5\,\mathrm{s}$.

After the fifteenth second the vibration spectrogram is similar to the beginning of the acquisition. The pattern of amplitude increase in frequencies specially above $2000\,\mathrm{Hz}$ and then a decrease to a uniform spectrogram was observed in all transducers and for all repetitions. Therefore, the increase of the amplitudes in the all frequencies due to the turbulence mentioned in Section 5.2.1, could also be observed in an elongated bubble rising in stagnant liquid. Moreover, it was perceptible that, in general, for these tests the highest amplitudes occurred in the frequencies near the $8000\,\mathrm{Hz}$, as observed in the Figure 5.24.

As observed in Figure 5.24, the vibration signal amplitude changes considerably in all frequencies when the 'Taylor bubble' passed. Thus, the amplitude variation in time of the vibration signal is easily observed with the vibration signal in time. The vibration signal in time is presented in Figure 5.25

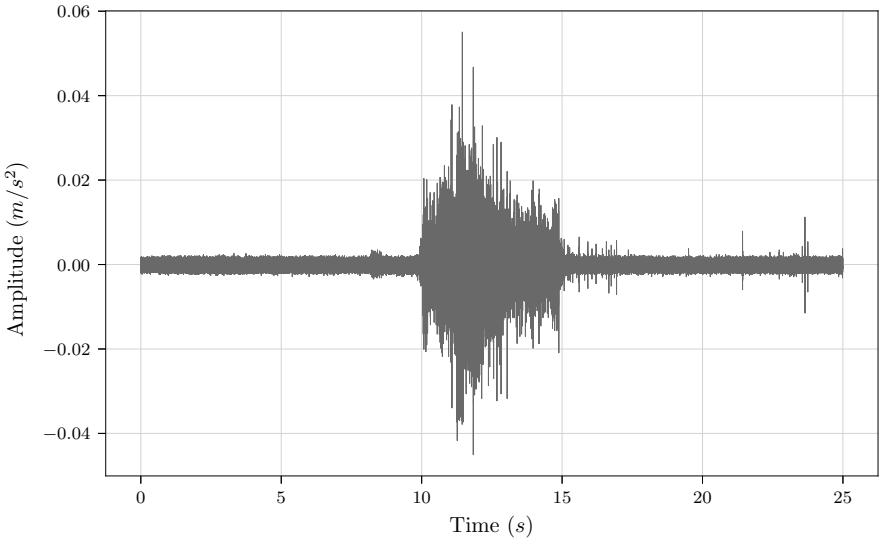

Figure 5.25: $25\,\mathrm{s}$ of the vibration signal of the elongated bubble rising.

The elongated bubble could be observed in all transducers. Thus, by using the same procedure used in Section 5.5.2 to calculate the 'Taylor bubble' velocity but for non-stagnant liquid, it would be possible to calculate the elongated bubble rising velocity. However, as stated above the highest amplitude variation was different from the presented in Section 5.2.1. Therefore, the use of the same frequency band, $2400\,\mathrm{Hz}$ to $2800\,\mathrm{Hz}$, may not be ideal.

Analysing the spectrogram presented in Figure 5.24 and the spectrograms of the other repetitions, it was observed that the frequency band with highest amplitudes that also changes with time, it was the frequency band from $2000\,\mathrm{Hz}$ to $10\,000\,\mathrm{Hz}$. As mentioned, the highest amplitudes observed were at frequencies near the $8000\,\mathrm{Hz}$. Hence, it would be better to calculate

the bubble rising velocity using a frequency band that contains those frequencies. Moreover, in the Section 5.5.2 it was used only the envelope of the filtered vibration signal to calculate the V_{TB}. In this case, it was also tested the energy of the signal obtained from the STFT and the filtered vibration signal.

The calculated velocities can be observed in Table 5.2. Furthermore, the elongated bubble rising velocity for all repetitions was manually estimated using the flow filming. Thus, the results using the flow filming are also shown in Table 5.2. The vibration results are from the cross-correlation of the second and the last transducers. It was the distance that presented the lower standard deviation between repetitions. Finally, to calculate the elongated bubble rising velocity it was used the Equation 3.45 with C_1 of 0.35. It is approximately the value of Nicklin, Wilkes and Davidson [67], and it is the value for the Bendiksen [68] and Théron [70] correlations, when considering vertical flows. Thus, the elongated bubble rising velocity with the correlation is approximately $0.2512\,\mathrm{m\,s^{-1}}$.

Table 5.2: Calculated elongated bubble rising velocity using cross-correlation.

		Repetitions velocities ($\mathrm{m\,s^{-1}}$)			
Source	Method	1	2	3	4
2400 Hz to 2800 Hz	Filtered	0.2487	0.2409	0.2457	0.2321
	STFT	0.2503	0.2392	0.2577	0.2386
	Envelope	0.2523	0.2581	0.2578	0.2561
2000 Hz to 10 000 Hz	Filtered	0.2494	0.2594	0.2648	0.2431
	STFT	0.2496	0.2474	0.2585	0.2460
	Envelope	0.2523	0.2581	0.2578	0.2561
Image	Manual	0.2568	0.2545	0.2579	0.2545

It noticeable in Table 5.2 that the frequency band did not affect the velocity calculated with the envelope. On the other hand, the frequency band affected the STFT and filtered vibration signal methods considerably. Besides, it is perceptible that all estimated velocities using the flow filming presented velocities higher than the literature correlation.

Comparing the velocities calculated with cross-correlation in Table 5.2 with the predicted velocity using the literature correlation. It is notable that all methods for all repetitions were able to estimate the velocity with a difference of $\pm 10\,\%$. Besides, the STFT method with a broader frequency band obtained on average the smallest percentage error, $1.77\,\%$. Furthermore, the STFT method obtained for all repetitions, but repetition 3, velocities lower than the literature correlation and the image. On the other hand, the envelope method obtained on average the smallest percentage error when comparing with the image estimated velocities, $0.99\,\%$.

Finally, the turbulence behind the 'Taylor bubble' can indeed induce a significant vibration, which is distinguishable from the other source of vibration and noise. Once, the turbulence of an elongated bubble in a stagnant liquid was sufficient to calculate the elongated bubble rising velocity with reasonable accuracy. Thus, the results presented in this section reinforces the stated

in Section 5.2.1 and the results presented in Section 5.5.2 and Section 5.5.1.

5.6.2 Progressive cavity pump

According to Vetter and Kozmiensky [77], theoretically, the progressive cavity pumps are pulsation-free, like all screw-type pumps. However, the authors mention that in reality, a slight pulsation is unavoidable due to internal leakages. Moreover, Paladino *et al.* [78] mention that several factors affect the flow leakage or 'slippage', such as the clearance between the rotor and stator, the fluid viscosity and the pressure difference between the cavities. Moreover, the number of cavities need to increase when the total differential pressure between the inlet and the outlet of the pump increases, to reduce the slippage.

Paladino *et al.* [78] state that if the stator is deformable, as the pressure increases the clearance and the slippage between the cavities also increases. They also mentioned that the flow regime near the sealing region also affects how the slippage will occur. In laminar flows, the slippage varies linearly, and in turbulent flows, the slippage will be proportional to some power less than 1 of the pressure drop [78].

As mentioned in Section 2.1.1, the pulsating flow is a FIV mechanism. Thus, it is important to assess the possible occurrence of a pulsating flow in the experiments. As stated above, the slippage which can cause a pulsating flow is related to the pressure difference between the cavities, which is related to the number of cavities of the pump and the differential pressure between its inlet and outlet.

On the other hand, as described in Section 4.1, the liquid and two-phase line are not pressurised. Moreover, the inlet of the pump is connected to the tank where the outlet of the pump is also connected. The tank is also opened to the atmosphere. Thus, when the pump is pumping, the difference of pressure between the inlet and the outlet of the pump is mainly related to the friction and localised pressure drop. Hence, the highest differential pressure, in this case, is when the pumping is at its maximum volumetric flow rate.

Finally, to verify the occurrence of a pulsating flow in the experimental apparatus used, it was set a liquid velocity of approximately $4\,\mathrm{m\,s^{-1}}$. It is the highest volumetric flow rate obtained. Then, it was used the STFT of the acquired vibration data, to try to observe a distinct amplitude variation of the amplitude of higher frequencies as observed in Section 5.2.1. The STFT was calculated using the same parameters used in Section 5.2.1. The spectrogram presented uses a logarithm scale. The grayscale used, the points with higher amplitudes are darker, and the points with lower amplitudes are the lighter points. Moreover, the grayscale limits are the lower and higher amplitudes observed. The STFT is presented in Figure 5.26.

As observed in Figure 5.26, it is not perceptible a significant and distinct frequency amplitude variation along the time, as observed in Section 5.2.1 and 5.6.1. Thus, the vibration caused by the pulsation of the flow of the progressive cavity pump was not significant to be measured by the transducers from where they were positioned.

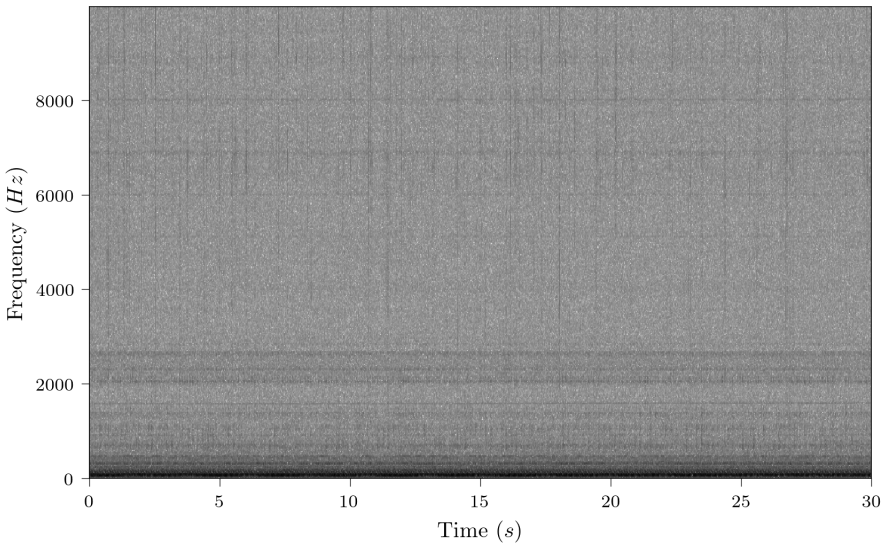

Figure 5.26: STFT of $30\,\mathrm{s}$ of the vibration signal with a liquid velocity of $4\,\mathrm{m\,s^{-1}}$.

6 Conclusions

6.1 General conclusions

In general, the results presented in Section 5 for vertical two-phase flow are consistent with the currently available literature, which is for horizontal two-phase flow. The results from analysing the signal with time-frequency tools suggest that the turbulence behind the 'Taylor bubble' are considerable and its effects could be distinguished from the others excitation mechanisms. A consequence of this was investigated, and it was possible to detect the 'Taylor bubble' passage utilising peak detections algorithms. Nevertheless, it was also possible to estimate some two-phase flow properties and classify the two-phase flow pattern with the vibration signal.

The evidence presented by contrasting the Fourier transform with the mixture Reynolds number in Section 5.1 pointed towards the idea that the subtle increase in the amplitudes of a specific frequency band was correlated with flow patterns, that are notorious for being oscillatory regarding liquid and gas passage. It was also suggested that the reason that those amplitudes were not high as the lower frequencies, was due to the mentioned in Section 3.3, where the frequencies magnitudes of the Fourier transform are an average over the whole length of the signal. Therefore, an analysis with time-frequency tools would be more appropriated.

Among the various TFA techniques, this work focused only on the short-time Fourier transform and wavelet transform. In both methods, the output spectrogram suggested that for the dispersed bubbles cases there was no significant change of the frequencies amplitudes along the time. On the other hand, for the slug and churn flow cases, the results supported the idea that turbulence just behind of the 'Taylor bubble' were considerable, and its effects could be distinguished from the others excitation mechanisms, where it was identified a consistent amplitude variation along the time. These results are consistent with the current literature. The amplitude variation pointed towards the idea to detect the 'Taylor bubble' with peak detection algorithms.

The energy of a frequency band was used to highlight the amplitude variation observed in the time-frequency analysis. It was observed that the number of peaks of churn flow was higher than the slug flow case analysed, which were consistent with the experiments. The energy signal suggested that the turbulent zone behind the 'Taylor bubble' does not have a significant effect when compared with other structural excitation mechanisms for lower gas flow rates. It pointed the idea that with turbulence reduction, it will be more difficult to detect them.

Various peak detections algorithms were tried to detect the energy peaks in the energy signal. It was observed that the energy amplitude varied dramatically across the same flow pattern and between flow patterns. Therefore, it was used the algorithm presented in Section 3.5 which had

satisfactory results. Thus, the average slug frequency could be estimated.

The signal energy amplitude variation pointed towards the idea that the analysis of the vibration signal in time in a specific frequency band would be relevant. Then, it was used a digital second-order Butterworth pass-band filter to analyse the signal in time domain. As suggested, the energy and the filtered vibration signal had a noticeable relationship between them. However, a noisy signal was observed which poses a problem to the peak detection algorithms, which pointed towards the idea to use the envelope of the filtered vibration signal.

The signal envelope was obtained by calculating the modulus of the Hilbert transform. However, it resulted in a 'noisy' envelope which was filtered by a low-pass Butterworth filter of second order. Then, the filtered envelope was analysed, and similar conclusions from the energy signal were drawn. Similar mean slug frequencies were obtained, using the same peak detection algorithm from the energy signal.

In the time domain analysis, it was possible to measure the mean slug frequency for specific acquisitions. Thus, the analysis was extended to the others acquisitions and the two vibration measurement stations. The results of this analysis indicate that the proposed technique presented a consistent result over the repetitions for the slug and churn flows. Furthermore, the results were consistent with the available literature for slug frequency in the two-phase vertical flow. However, as the liquid velocity increased, a few acquisitions presented a high standard deviation despite being classified as slug or churn flows. It was discussed that the high standard deviation is related to the flow pattern transition. The evidence of the difference from the mean slug frequency of the two vibration measurement station suggests an effect of the gas-phase acceleration.

In Section 3.4, it was mentioned that using the cross-correlation between two signals it is possible to measure the time delay between them. Then, the results in Section 5.2.1 pointed towards the idea that if there were a high-frequency attenuation of the band frequency analysed over the structure. It would be possible to estimate the V_{GTB} by calculating the cross-correlation between the two vibration measurement station. The results of this analysis indicate that the proposed technique presented a consistent result over the repetitions for most of slug and churn flows cases, due to the low standard deviation. Furthermore, it was mentioned that the V_{GTB} can be considered approximately the V_{TB}, which has a set of correlation available in the literature. Hence, the different literature correlations were compared with the obtained V_{TB}. The results were consistent with the correlations.

The acquisitions 31 and 34, which was classified as a churn flow and dispersed bubble respectively, also presented a low standard deviation but the calculated velocity did not match with any of the two-phase flow velocities. Besides, the 31 acquisition case is near the transition region between the churn and dispersed bubbles, and it may have influenced the results. In general, the dispersed bubbles cases presented a high standard deviation. The results indicate that the transducer positioning and the envelope settings are not adequated to analyse the dispersed bubble cases.

As an exploratory approach, in Section 5.5.3, it was tried to correlate the envelope of the

filtered vibration signal with the GVF. The findings indicate that there is a quadratic correlation between the measurement GVF and the standard deviation of the envelope of the filtered signal. The coefficient of determination, R^2, obtained was of 0.93 for all acquisitions. Then, a quadratic fit using a few selected acquisitions and removing acquisitions with mixture Reynolds number below the acquisition 14 obtained a coefficient of determination of 0.97. It was tried to fit the GVF with linear, quadratic, cubic, exponential and logarithm functions.

In the Sections 5.2.1 and 5.4, a clear difference between the spectrograms signal envelopes of the different flow patterns was observed. Thus, it suggested the possibility to use both spectrogram and envelope to determine the flow pattern. However, the spectrogram is more expensive computationally thus the envelope approach was used. Then, similarly to the estimation of GVF with the envelope, an exploratory approach was used to look for different parameters that change considerably over the flow patterns. The results suggested that it is possible to separate the churn flow pattern from the other patterns by using the RMS of the envelope with a threshold. Moreover, it was used the Pearson correlation coefficient to determine if the flow is dispersed bubble. This method was capable of classifying accurately $93.57\,\%$ of the points.

In Section 5.5.2 it was shown that the 'Taylor bubble' velocity within a flowing liquid could be measured with reasonable accuracy. However, it was not possible to assess the vibration induced by the 'Taylor bubble' separately. Thus, a new experimental procedure was elaborated. It generated an elongated bubble under a stagnant liquid. Thus, the elongated bubble velocity could also be obtained using literature correlations and compared with the proposed method. The proposed method could calculate the velocity with reasonable accuracy. Besides, the turbulence behind the 'Taylor bubble' could induce a significant structural vibration, which was distinguishable from the other source of vibration and noise.

In Section 5.6.2 it was mentioned that the progressive cavity pumps are not pulsation-free due to internal leakages. Once pulsating flow is FIV mechanism, it was investigated the possibility of liquid pulsation in the pipeline. Thus, a new experimental procedure was elaborated with the highest liquid volumetric flow rate obtained in the experimental apparatus. Then, it was not observed a significant and distinct frequency amplitude variation along the time. Therefore, the vibration caused by the pulsation of the flow of the progressive cavity pump was not significant to be measured by the transducers from where they were positioned.

6.2 Limitations

This work certainly has some limitations. The most important lies in the fact that some aspects of the findings might not be transferable to other piping systems. Due to the fact that the frequency band analysed and used to get all the results presented is specific to this experimental apparatus. Additionally, this study is based on the turbulence behind the 'Taylor bubble', thus, the findings are limited to fluids that have similar viscosity. However, the idea can be generalised to other piping systems and fluids, by looking for the piping underdamped modes to select a specific

band where the turbulence effect is more prominent and then apply the same techniques and analysis used in this work.

Finally, many potential limitations and weakness need to be considered. First, the accelerometer position affects the results. If the accelerometer position is changed, it is required to change the thresholds of the pattern classification and also a new GVF curve fit. On the other hand, as the mean slug frequency and velocity estimation do not depend directly on the signal. Thus, it is still possible to estimate the flow velocity when changing the accelerometer position by only updating the distance between the measurement stations. Furthermore, the peak detection algorithm does not have free parameters. Therefore, the algorithm is capable to detect the peaks despite the changing in the transducer position.

Second, the frequency attenuation along the pipe was enough to enable the velocity calculation with cross-correlation. However, if for some reason, there are some impacts or periodic force that results in a signal similar to the observed, near to the transducers, the proposed technique will result in wrong estimations. The picture is thus still incomplete.

6.3 Knowledge contributions

This study is a step towards enhancing our understanding of flow-induced vibration by two-phase flows in vertical upward flow piping system. To date, differently, from horizontal two-phase flows, it was not possible to find similar works that study the effect of the turbulence of the slug and churn flows in the vibration of straight pipelines in vertical upward flows.

6.4 Future works

This research has raised up many questions in need of further investigation.

On a broader level, research is also needed to determine better the interactions between the slug and churn flows turbulent regions with the structure.

Further works with an additional and more established measurement system to obtain the V_{TB} and slug frequency would be able to better assess the proposed technique accuracy.

Extra experimental investigations need to be done to verify the gas void fraction quadratic relationship with the envelope subjected over low mixture Reynolds number flows.

Additional works need to be done to establish a better relationship between the envelope with the gas void fraction, an analytical approach is suggested.

Additional work in the parameter used to classify the flow patterns would help to enhance the technique.

Further experimental investigations with different piping systems and fluids are needed to assess the technique robustness.

Bibliography

[1] G. Falcone, “Chapter 1 Multiphase Flow Fundamentals”, in *Multiphase Flow Metering*, ser. Developments in Petroleum Science, G. Falcone, G. F. Hewitt and C. Alimonti, Eds., vol. 54, Elsevier, 2009, pp. 1–18.

[2] O. Shoham, *Mechanistic Modeling of gas liquid two phase flow in pipes*. Richardson, Texas, EUA: The Society of Petroleum Engineers (SPE), 2006.

[3] G. Falcone, “Chapter 2 Introduction to Multiphase Flow Metering”, in *Multiphase Flow Metering*, ser. Developments in Petroleum Science, G. Falcone, G. F. Hewitt and C. Alimonti, Eds., vol. 54, Elsevier, 2009, pp. 19–31.

[4] ——, “Chapter 4 Key Multiphase Flow Metering Techniques”, in *Multiphase Flow Metering*, ser. Developments in Petroleum Science, G. Falcone, G. F. Hewitt and C. Alimonti, Eds., vol. 54, Elsevier, 2009, pp. 47–190.

[5] M. M. F. Figueiredo, J. L. Goncalves, A. M. V. Nakashima, A. M. F. Fileti and R. D. M. Carvalho, “The use of an ultrasonic technique and neural networks for identification of the flow pattern and measurement of the gas volume fraction in multiphase flows”, *Experimental Thermal and Fluid Science*, vol. 70, pp. 29–50, 2016.

[6] C.-g. Xie, “Measurement Of Multiphase Flow Water Fraction And”, pp. 232–239, 2007.

[7] Y. Murai, S. Ohta, A. Shigetomi, Y. Tasaka and Y. Takeda, “Development of an ultrasonic void fraction profiler”, *Measurement Science and Technology*, vol. 20, no. 11, 2009.

[8] M. J. da Silva, S. Thiele, E. Schleicher and U. Hampel, “Wire-Mesh Sensors for High-Resolution Gas-Liquid Multiphase Flow Visualization”, *Proceedings of COBEM 2009; 20th International Congress of Mechanical Engineering*, 2009.

[9] H. F. Velasco Peña and O. M. H. Rodriguez, “Applications of wire-mesh sensors in multiphase flows”, *Flow Measurement and Instrumentation*, vol. 45, pp. 255–273, 2015.

[10] H. M. Prasser, A. Böttger and J. Zschau, “A new electrode-mesh tomograph for gas-liquid flows”, *Flow Measurement and Instrumentation*, vol. 9, no. 2, pp. 111–119, 1998.

[11] M. G. Rasteiro, R. Silva, F. A. P. Garcia and P. Faia, “Electrical tomography: A review of configurations and applications to particulate processes”, *KONA Powder and Particle Journal*, vol. 29, no. 29, pp. 67–80, 2011.

[12] U. Hampel, M. Speck, D. Koch, H. J. Menz, H. G. Mayer, J. Fietz, D. Hoppe, E. Schleicher, C. Zippe and H. M. Prasser, “Experimental ultra fast X-ray computed tomography with a linearly scanned electron beam source”, *Flow Measurement and Instrumentation*, vol. 16, no. 2-3, pp. 65–72, 2005.

[13] T. Nakamura and S. Kaneko, *Flow-Induced vibrations classification and lessons from practical experiences*. 2008.

[14] M. J. Pettigrew, C. E. Taylor, N. J. Fisher, M Yetisir and B. A. W. Smith, "Flow-induced vibration: recent findings and open questions", *Nuclear Engineering and Design*, vol. 185, pp. 249–276, 1998.

[15] L. E. Ortiz-Vidal, N. W. Mureithi and O. M. H. Rodriguez, "Vibration response of a pipe subjected to two-phase flow: Analytical formulations and experiments", *Nuclear Engineering and Design*, vol. 313, pp. 214–224, 2017.

[16] L. E. Ortiz-Vidal, O. M. H. Rodriguez and N. W. Mureithi, "An Exploratory Experimental Technique to Predict Two-Phase Flow Pattern From Vibration Response", *ASME2013 Pressure Vessels and Piping Conference. Volume 4: Fluid-Structure Interaction*, V004T04A061, 2013.

[17] "Chapter 1 - Introduction", in *Flow-induced Vibrations (Second Edition)*, S. Kaneko, T. Nakamura, F. Inada, M. Kato, K. Ishihara, T. Nishihara and M. A. Langthjem, Eds., Second Edi, Oxford: Academic Press, 2014, pp. 1–28.

[18] R. D. Blevins, *Flow-induced vibration*. Van Nostrand Reinhold Co., 1977.

[19] S. Miwa, M. Mori and T. Hibiki, "Two-phase flow induced vibration in piping systems", *Progress in Nuclear Energy*, vol. 78, no. 2015, pp. 270–284, 2015.

[20] R. D. Blevins, "Flow-induced vibration in nuclear reactors: A review", *Progress in Nuclear Energy*, vol. 4, no. 1, pp. 25–49, 1979.

[21] L. E. O. Vidal and O. M. H. Rodriguez, "Flow-Induced Vibration Due To Gas-Liquid Pipe Flow : Knowledge Evolution", in *COBEM 2011*, Natal, Rio Grande do Norte, Brazil: ABCM, 2011.

[22] M. J. Pettigrew and C. E. Taylor, "Two-Phase Flow-Induced Vibration: An Overview", *Journal of Pressure Vessel Technology*, vol. 116, no. 3, p. 233, 1994.

[23] T. Hibiki and M. Ishii, "Effect of flow-induced vibration on local flow parameters of two-phase flow", *Nuclear Engineering and Design*, vol. 185, no. 2-3, pp. 113–125, 1998.

[24] J.-L. Riverin and M. J. Pettigrew, "Vibration Excitation Forces Due to Two-Phase Flow in Piping Elements", *Journal of Pressure Vessel Technology*, vol. 129, no. 1, p. 7, 2007.

[25] T. Sasakawa, A. Serizawa and Z. Kawara, "Fluid-elastic vibration in two-phase cross flow", *Experimental Thermal and Fluid Science*, vol. 29, no. 3, pp. 403–413, 2005.

[26] M. P. Païdoussis, "Real-life experiences with flow-induced vibration", *Journal of Fluids and Structures*, vol. 22, no. 6-7, pp. 741–755, 2006.

[27] S. Khushnood, Z. M. Khan, M. A. Malik, Z. U. Koreshi and M. A. Khan, "A review of heat exchanger tube bundle vibrations in two-phase cross-flow", *Nuclear Engineering and Design*, vol. 230, no. 1-3, pp. 233–251, 2004.

[28] F. T. Kanizawa, L. P. R. de Oliveira and G. Ribatski, “State-of-the-Art Review on Flow Patterns, Superficial Void Fraction and Flow-Induced Vibration During Two-Phase Flows Across Tube Bundles”, in *Volume 2: Fora*, ASME, 2012, p. 79.

[29] O. Sadek, A. Mohany and M. Hassan, “Numerical investigation of the cross flow fluidelastic forces of two-phase flow in tube bundle”, *Journal of Fluids and Structures*, vol. 79, pp. 171–186, 2018.

[30] N. bin Jiang, F. rui Xiong, F. gang Zang, Y. xiong Zhang and H. huan Qi, “Analysis on vibration response of U-tube bundles caused by two-phase cross-flow turbulence”, *Annals of Nuclear Energy*, vol. 99, pp. 328–334, 2017.

[31] M. Shaaban and A. Mohany, “Flow-induced vibration of three unevenly spaced in-line cylinders in cross-flow”, *Journal of Fluids and Structures*, vol. 76, pp. 367–383, 2018.

[32] S. Kaneko, T. Nakamura, F. Inada, M. Kato, K. Ishihara, T. Nishihara and M. A. Langthjem, “Chapter 4 - Vibrations Induced by Internal Fluid Flow”, in *Flow-induced Vibrations (Second Edition)*, Second Edi, Oxford: Academic Press, 2014, pp. 157–195.

[33] B. G. Sinir and D. D. Demir, “The analysis of nonlinear vibrations of a pipe conveying an ideal fluid”, *European Journal of Mechanics, B/Fluids*, vol. 52, pp. 38–44, 2015.

[34] D. G. Gorman, J. M. Reese and Y. L. Zhang, “Vibration of a flexible pipe conveying viscous pulsating fluid flow”, *Journal of Sound and Vibration*, vol. 230, no. 2, pp. 379–392, 2000.

[35] H. R. Ozöz, “Non-linear vibrations and stability analysis of tensioned pipes conveying fluid with variable velocity”, *International Journal of Non-Linear Mechanics*, vol. 36, no. 7, pp. 1031–1039, 2001.

[36] S. I. Lee and J. Chung, “New non-linear modelling for vibration analysis of a straight pipe conveying fluid”, *Journal of Sound and Vibration*, vol. 254, no. 2, pp. 313–325, 2003.

[37] B. H. Li, H. S. Gao, H. B. Zhai, Y. S. Liu and Z. F. Yue, “Free vibration analysis of multi-span pipe conveying fluid with dynamic stiffness method”, *Nuclear Engineering and Design*, vol. 241, no. 3, pp. 666–671, 2011.

[38] Q. Ni, Z. L. Zhang and L. Wang, “Application of the differential transformation method to vibration analysis of pipes conveying fluid”, *Applied Mathematics and Computation*, vol. 217, no. 16, pp. 7028–7038, 2011.

[39] S. J. Li, G. M. Liu and W. T. Kong, “Vibration analysis of pipes conveying fluid by transfer matrix method”, *Nuclear Engineering and Design*, vol. 266, pp. 78–88, 2014.

[40] M. Giraudeau, N. W. Mureithi and M. J. Pettigrew, “Two-Phase Flow-Induced Forces on Piping in Vertical Upward Flow: Excitation Mechanisms and Correlation Models”, *Journal of Pressure Vessel Technology*, vol. 135, no. 3, p. 030 907, 2013.

[41] J. Tian, C. Yuan, L. Yang, C. Wu, G. Liu and Z. Yang, "The vibration analysis model of pipeline under the action of gas pressure pulsation coupling", *Engineering Failure Analysis*, vol. 66, pp. 328–340, 2016.

[42] R. P. Evans, J. D. Blotter and A. G. Stephens, "Flow Rate Measurements Using Flow-Induced Pipe Vibration", *Journal of Fluids Engineering*, vol. 126, no. 2, p. 280, 2004.

[43] A. L. Gama, L. R.d. S. Ferreira, P. H. A. Walter, L. R. dos Santos Ferreira and P. H. A. Walter Filho, "Experimental Study on the Measurement of Two-Phase Flow Rate Using Pipe Vibration", in *Proceedings of 20th International Congress of Mechanical Engineering, COBEM*, 2009, pp. 15–20.

[44] C. Hua, C. Wang, Y. Geng and T. Shi, "Noninvasive flow regime identification for wet gas flow based on flow-induced vibration", *Chinese Journal of Chemical Engineering*, vol. 18, no. 5, pp. 795–803, 2010.

[45] Y. Geng, F. Ren and C. Hua, "An auxiliary measuring technology of wet gas flow based on the vibration signals of the pipe", *Flow Measurement and Instrumentation*, vol. 27, pp. 113–119, 2012.

[46] J. M. Mandhane, G. A. Gregory and K. Aziz, "A flow pattern map for gas-liquid flow in horizontal pipes", *International Journal of Multiphase Flow*, vol. 1, no. 4, pp. 537–553, 1974. arXiv: arXiv:1011.1669v3.

[47] K. Shin, *Fundamentals of signal processing for sound and vibration engineers*. Chichester,West Sussex, England: John Wiley & Sons, 2008.

[48] R. Figliola and D. Beasley, *Theory and design for mechanical measurements*, 5th, L. Ratts and A. Melhorn, Eds. Hoboken, New Jersey, United States of America: John Wiley & Sons Inc., 2011.

[49] H. P. Hsu, *Schaum's outline of theory and problems of signals and systems*. New York, NY: McGraw-Hill, 1995, pp. 1–483.

[50] J. W. Cooley and J. W. Tukey, "An algorithm for the machine calculation of complex Fourier series", *Mathematics of Computation*, vol. 19, no. 90, p. 297, 1965.

[51] A. V. Oppenheim and R. W. Schafer, *Discrete Time Signal Processing*. Upper Saddle River, New Jersey, United States of America: Prentice-Hall, Inc., 2009, p. 1120.

[52] J. G. Proakis, *Digital signal processing : principles, algorithms, and applications*. Upper Saddle River, N.J: Prentice Hall, 1996.

[53] S. W. Smith, *Digital signal processing*. Sab Diego, California, United States of America: California Technical Publishing, 1999, p. 688. arXiv: 97-80293.

[54] D. E. Newland, *An Introduction to Random Vibrations, Spectral & Wavelet Analysis*, Mineola, New York, United States of America, 2005.

[55] D. E. Newland, “Wavelet Analysis of Vibration Signals”, *Handbook of Noise and Vibration Control*, pp. 585–597, 2007.

[56] S. Mallat, “A Wavelet Tour of Signal Processing”, *A Wavelet Tour of Signal Processing*, 2009. arXiv: arXiv:1011.1669v3.

[57] B. MacLennan, “Gabor Representations of Spatiotemporal Visual Images”, pp. 1–42, 1991.

[58] M. Hall, “Resolution and uncertainty in spectral decomposition”, *First Break*, vol. 24, no. 12, pp. 43–47, 2006.

[59] R. X. Gao and R. Yan, “Wavelets: Theory and applications for manufacturing”, *Wavelets: Theory and Applications for Manufacturing*, pp. 1–224, 2011. arXiv: arXiv:1011.1669v3.

[60] C. Torrence and G. P. Compo, “A practical guide to wavelet analysis”, *Bulletin of the American Meteorological society*, vol. 79, no. 1, pp. 61–78, 1998.

[61] N. G. Nikolaou and I. A. Antoniadis, “Demodulation of vibration signals generated by defects in rolling element bearings using complex shifted Morlet wavelets”, *Mechanical Systems and Signal Processing*, vol. 16, no. 4, pp. 677–694, 2002.

[62] F. Scholkmann, J. Boss and M. Wolf, “An efficient algorithm for automatic peak detection in noisy periodic and quasi-periodic signals”, *Algorithms*, vol. 5, no. 4, pp. 588–603, 2012.

[63] H. Rodrigues and R. Morales, “A comparitive study of closure equations for gas-liquid slug flow”, *19th International Congress of Mechanical Engineering*, 2007.

[64] G. B. Wallis, “One-dimensional two-phase flow”, in *AIChE Journal*, 6, vol. 16, New York, NY, United States of America, 1969, pp. 896–1105.

[65] A. E. Dukler and M. G. Hubbard, “A Model for Gas-Liquid Slug Flow in Horizontal and Near Horizontal Tubes”, *Industrial & Engineering Chemistry Fundamentals*, vol. 14, no. 4, pp. 337–347, 1975.

[66] Y. Taitel and D. Barnea, “A consistent approach for calculating pressure drop in inclined slug flow”, *Chemical Engineering Science*, vol. 45, no. 5, pp. 1199–1206, 1990.

[67] D. J. Nicklin, M. A. Wilkes and J. F. Davidson, “Two-Phase Flow in Vertical Tubes”, *Transactions of the Institution of Chemical Engineers*, vol. 40, pp. 61–67, 1962.

[68] K. H. Bendiksen, “An experimental investigation of the motion of long bubbles in inclined tubes”, *International Journal of Multiphase Flow*, vol. 10, no. 4, pp. 467–483, 1984.

[69] A. E. Dukler, D. Moalem Maron and N. Brauner, “A physical model for predicting the minimum stable slug length”, *Chemical Engineering Science*, vol. 40, no. 8, pp. 1379–1385, 1985.

[70] B. Théron, "Écoulements diphasiques instationnaires en conduite horizontale", PhD thesis, Institut National Polytechnique de Toulouse, France, 1989.

[71] N. Petalas and K. Aziz, "A Mechanistic Model for Multiphase Flow in Pipes", *Journal of Canadian Petroleum Technology*, vol. 39, no. 06, pp. 43–55, 2000.

[72] M. Abdulkadir, V. Hernandez-Perez, L. Abdulkareem, I. S. Lowndes and B. J. Azzopardi, "Characteristics of slug flow in a vertical riser", *34th SPE Annual International Conference and Exhibition*, vol. 2, pp. 875–881, 2010.

[73] G. F. Hewitt, J.-M. Delhaye and N. Zuber, *Multiphase science and technology*. Springer Science & Business Media, 2013, vol. 2.

[74] V. R. Inc., *Phantom VEO 640*, 2018.

[75] W. Monte Verde, "Performance modeling of ESP pumps performance operating with gas-viscous liquid mixtures", PhD. Thesis, University of Campinas, 2016.

[76] Y. Taitel, D. Bornea and A. E. Dukler, "Modelling flow pattern transitions for steady upward gas-liquid flow in vertical tubes", *AIChE Journal*, vol. 26, no. 3, pp. 345–354, 1980.

[77] G. Vetter and R. Kozmiensky, "Pulsation and NPSHA in rotary positive displacement pumps", *World Pumps*, vol. 1999, no. 389, pp. 37–42, 1999.

[78] E. E. Paladino, J. A. Lima, P. A. S. Pessoa and R. F. C. Almeida, "A computational model for the flow within rigid stator progressing cavity pumps", *Journal of Petroleum Science and Engineering*, vol. 78, no. 1, pp. 178–192, 2011.

[79] F. E. Jones and G. L. Harris, "ITS-90 density of water formulation for volumetric standards calibration", *Journal of Research of the National Institute of Standards and Technology*, vol. 97, no. 3, p. 335, 1992.

[80] F. White, *Fluid mechanics*, 6th. New York: McGraw-Hill, 2007.

A Python codes

A.1 Frequency domain and time-frequency analysis

The Python code below was used to perform the frequency domain and time-frequency analysis.

```
import numpy as np
import scipy.signal as sg
from nptdms import TdmsFile
import matplotlib.pyplot as plt


# Open the file
acq = 1 # Acquisition number
rep = 1 # Repetition number
td_file = TdmsFile('./data/acq{}/{}/vibration.tdms'.format(acq, rep))
# Get the sample rate
fs = td_file.object('Horizontal Settings')
fs = fs.properties['Min. Sample Rate']
# Get the data
chnls, data = [], []
for chnl in td_file.group_channels('Channels'):
   data += [chnl.data]
   chnls += [chnl.channel]
# Convert the list to n-dimensional numpy array
data = np.array(data)
# Get the total time
tt = data.shape[1]/fs

# Set channel to be analysed
chnl = 0


# Perform the FFT
X = np.fft.fft(data[chnl])
n = X.size
T = 1/fs
freq = np.fft.fftfreq(n, d=T)
# FFT modulus and positive part
```

```
X = np.abs(X)[1:int(n/2)]/n
freq = freq[1:int(n/2)]
# Plot the FFT
plt.plot(freq, X)
plt.xlabel(r'Frequency ($Hz$)')
plt.ylabel(r'Amplitude ($m/s^2$)')
plt.grid(True)


# Perform the STFT
f, ts, z = sg.stft(data[chnl], fs=fs, nperseg=3000)
# Calculate the modulus of the STFT
z = np.abs(z)
# Plot the STFT
plt.pcolormesh(ts, f, np.log10(z), cmap='jet')
plt.xlabel(r'Time ($s$)')
plt.ylabel(r'Frequency ($Hz$)')


# Wavelet transform
# Morlet wavelet
def morlet(t, s=1.0, w0=6, complete=True):
    x = t/s
    output = np.exp(1j * w0 * x)
    if complete:
        output -= np.exp(-0.5 * (w0**2))
    output *= np.exp(-0.5 * (x ** 2)) * np.pi ** (-0.25)
    return output

x = data[chnl]
# Wavelet central frequency
w0 = 12 # Hz
# Set the frequency band
lmts = [1, 100]
# Set the number of frequencies in the frequency band
nelm = 3
# Create an array of the frequencies to be calculated
freqs = np.linspace(lmts[0], lmts[1], nelm)
# Get the wavelet scales
scales = (w0 + (2 + w0**2)**.5)/(4*np.pi*freqs)
# Set the dt
```

```
dtt = 1/fs
# Initialize the cwt vector
cwt = np.zeros((len(scales), x.shape[0]), dtype=np.complex)
ts = np.array(np.arange(0, x.shape[0]/fs, dtt))

# Compute the wavelet
for idx, s in enumerate(scales):
    # number of points needed to capture wavelet
    M = 10*s/dtt
    M = x.shape[0] if M > x.shape[0] else M
    # times to use, centred at zero
    t = np.arange((-M + 1) / 2., (M + 1) / 2.) * dtt
    # sample wavelet and normalise
    psi = (dtt/(s**0.5))*morlet(t, s, w0)
    # perform the convolution
    cwt[idx, :] = sg.fftconvolve(x, psi, mode='same')

# Get the modulus of cwt
cwt = np.abs(cwt)
# Plot the wavelet transform
plt.pcolormesh(ts, freqs, np.log10(cwt), cmap='jet')
plt.xlabel(r'Time ($s$)')
plt.ylabel(r'Frequency ($Hz$)')
```

A.2 Signal energy and envelope

The Python code below was used to generate and perform the analysis on the signal energy and the vibration signal envelope. It also contains the AMPD code and the mean slug frequency calculation with the AMPD output.

```
import numpy as np
import scipy.signal as sg
from nptdms import TdmsFile
import matplotlib.pyplot as plt


# Open the file
acq = 1 # Acquisition number
rep = 1 # Repetition number
td_file = TdmsFile('./data/acq{}/{}/vibration.tdms'.format(acq, rep))
# Get the sample rate
```

```
fs = td_file.object('Horizontal Settings')
fs = fs.properties['Min. Sample Rate']
# Get the data
chnls, data = [], []
for chnl in td_file.group_channels('Channels'):
   data += [chnl.data]
   chnls += [chnl.channel]
# Convert the list to n-dimensional numpy array
data = np.array(data)
# Get the total time
tt = data.shape[1]/fs

# Set channel to be analysed
chnl = 0

# Wavelet transform
# Define the Morlet wavelet function
def morlet(t, s=1.0, w0=6, complete=True):
   x = t / s
   output = np.exp(1j * w0 * x)
   if complete:
      output -= np.exp(-0.5 * (w0**2))
   output *= np.exp(-0.5 * (x ** 2)) * np.pi ** (-0.25)
   return output


x = data[chnl]
# Wavelet central frequency
w0 = 12 # Hz
# Set the frequency band
lmts = [1, 100]
# Set the number of frequencies in the frequency band
nelm = 3
# Create an array of the frequencies to be calculated
freqs = np.linspace(lmts[0], lmts[1], nelm)
# Get the wavelet scales
scales = (w0 + (2 + w0**2)**.5) / (4 * np.pi * freqs)
# Set the dt
dtt = 1 / fs
# Initialize the cwt vector
cwt = np.zeros((len(scales), x.shape[0]), dtype=np.complex)
```

```
ts = np.array(np.arange(0, x.shape[0] / fs, dtt))

# Compute the wavelet
for idx, s in enumerate(scales):
    # number of points needed to capture wavelet
    M = 10 * s / dtt
    M = x.shape[0] if M > x.shape[0] else M
    # times to use, centred at zero
    t = np.arange((-M + 1) / 2., (M + 1) / 2.) * dtt
    # sample wavelet and normalise
    psi = (dtt / (s**0.5)) * morlet(t, s, w0)
    # perform the convolution
    cwt[idx, :] = sg.fftconvolve(x, psi, mode='same')

# Get the modulus of cwt
cwt = np.abs(cwt)
# Caclulate the energy of a frequency band
cwt_en = np.power(cwt.sum(axis=0),2)
# Plot the energy of the signal
plt.plot(ts, cwt_en)
plt.xlabel(r'Time ($s$)')
plt.ylabel(r'Frequency ($Hz$)')

# Calculate the filtered envelope of the filtered vibration signal
# Set the filters limits
filt_band = [2400, 2800]
filt_low = [12]
# Set the Butterworth filter parameters
b_band, a_band = sg.butter(2, np.array(filt_band)*2/fs, btype='band')
b_low, a_low = sg.butter(2, np.array(filt_low)*2/fs, btype='low')
# Filter the vibration signal
vib_filt = sg.filtfilt(b_band, a_band, data[chnl])
# Calculate the Hilbert transform
h = sg.hilbert(vib_filt)
# Calculate the envelope
h_env = np.abs(h)
# Filter the envelope
h_envf = sg.filtfilt(b_low, a_low, h_env)

# Generate a time array
ts = np.linspace(0, tt, h_envf.shape[0])
```

```
# Plot the filtered envelope
plt.plot(ts, h_envf)
plt.grid(True)
plt.xlabel(r'Time ($s$)')
plt.ylabel(r'Amplitude ($m/s^2$)')

# Define the AMPD function
def ampd(x):
    # Create preprocessing linear fit
    t = np.arange(0, len(y))
    # Fit a linear curve to detrend
    pol = np.polyfit(t, y, 1)
    fit = np.polyval(pol, t)
    # Detrend
    dtry = y - fit
    # Get the dimensions
    N = dtry.shape[0]
    L = np.ceil(N / 2).astype('int') - 1
    # Generate random matrix
    LSM = np.random.uniform(1.0, 2.0, size=(L, N)) # uniform + alpha
        = 1
    # Get the LSM matrix
    for k in np.arange(1, L):
        # Initialize an array of false values
        mask = np.zeros(N, dtype=bool)
        # Get the scale mask
        mask[k:N - k - 1] = (dtry[k: N - k - 1] > dtry[0: N - 2*k - 1]
                        )*(dtry[k: N - k - 1] > dtry[2*k: N - 1])
        LSM[k - 1, mask] = 0
    # Get the row-wise summation minimum
    G = np.sum(LSM, 1)
    l = np.where(G == G.min())[0][0]
    LSM = LSM[0:l, :]
    # Calculate the standard deviation
    S = np.std(LSM, 0)
    # Get the peaks
    pks = np.where(S == 0)[0]
    return pks

# Get the peaks of the filtered envelope
pks = ampd(h_envf)
```

```
# Caculate the mean frequency
mean_f = np.mean(1/np.diff(ts[pks]))
# Plot the with the peaks and the mean slug frequency
plt.plot(ts,y)
plt.plot(ts[pks], y[pks], 'ro')
plt.title(r'Mean slug frequency: {:.2f} $Hz$'.format(mean_f))
plt.grid(True)
plt.xlabel(r'Time ($s$)')
plt.ylabel(r'Amplitude ($m/s^2$)')
```

A.3 V_{TB} estimation

The Python code below was used to calculate the V_{TB} using the filtered envelope of the filtered vibration signal. It uses the cross-correlation between two vibration measurement station.

```
import numpy as np
import scipy.signal as sg
from nptdms import TdmsFile
import matplotlib.pyplot as plt


# Open the file
acq = 1 # Acquisition number
rep = 1 # Repetition number
td_file = TdmsFile('./data/acq{}/{}/vibration.tdms'.format(acq, rep))
# Get the sample rate
fs = td_file.object('Horizontal Settings')
fs = fs.properties['Min. Sample Rate']
# Get the data
chnls, data = [], []
for chnl in td_file.group_channels('Channels'):
    data += [chnl.data]
    chnls += [chnl.channel]
# Convert the list to n-dimensional numpy array
data = np.array(data)
# Get the total time
tt = data.shape[1] / fs

# Set channel to be analysed
chnl = [0, 1]

```

```
# Calculate the filtered envelope of the filtered vibration signal
# Set the filters limits
filt_band = [2400, 2800]
filt_low = [12]
# Set the Butterworth filter parameters
b_band, a_band = sg.butter(2, np.array(filt_band)*2/fs, btype='band')
b_low, a_low = sg.butter(2, np.array(filt_low)*2/fs, btype='low')
# Filter the vibration signal
vib_filt = sg.filtfilt(b_band, a_band, data[chnl])
# Calculate the Hilbert transform
h = sg.hilbert(vib_filt)
# Calculate the envelope
h_env = np.abs(h)
# Filter the envelope
h_envf = sg.filtfilt(b_low, a_low, h_env)

# Get the highest correlation delay using FFT
# Set the distance between the transducers
l = 1.5
# Perform the FFT
X = np.fft.rfft(h_envf[1])
Y = np.fft.rfft(h_envf[0])
R = X*np.conjugate(Y)
cc = np.split(np.fft.irfft(R), 2)[0]
# Get the highest correlation index
shift = cc.argmax()
# Calculate the velocity
vel = l*fs/shift
print(r'The calculated velocity is: {:.2f} (m/s)'.format(vel))
```

A.4 Flow pattern

The Python code below was used to obtain the flow pattern.

```
import numpy as np
import scipy.stats as st
import scipy.signal as sg
from nptdms import TdmsFile
import matplotlib.pyplot as plt


```

```
# Open the file
acq = 1 # Acquisition number
rep = 1 # Repetition number
td_file = TdmsFile('./data/acq{}/{}/vibration.tdms'.format(acq, rep))
# Get the sample rate
fs = td_file.object('Horizontal Settings')
fs = fs.properties['Min. Sample Rate']
# Get the data
chnls, data = [], []
for chnl in td_file.group_channels('Channels'):
    data += [chnl.data]
    chnls += [chnl.channel]
# Convert the list to n-dimensional numpy array
data = np.array(data)
# Get the total time
tt = data.shape[1] / fs

# Set channel to be analysed
chnl = 0

# Calculate the filtered envelope of the filtered vibration signal
# Set the filters limits
filt_band = [2400, 2800]
filt_low = [12, 50]
# Set the Butterworth filter parameters
b_band, a_band = sg.butter(2, np.array(filt_band)*2/fs, btype='band')
b_low1, a_low1 = sg.butter(2, np.array(filt_low[0])*2/fs,
    btype='low')
b_low2, a_low2 = sg.butter(2, np.array(filt_low[1])*2/fs,
    btype='low')
# Filter the vibration signal
vib_filt = sg.filtfilt(b_band, a_band, data[chnl])
# Calculate the Hilbert transform
h = sg.hilbert(vib_filt)
# Calculate the envelope
h_env = np.abs(h)
# Filter the envelope
h_envf1 = sg.filtfilt(b_low1, a_low1, h_env)
h_envf2 = sg.filtfilt(b_low2, a_low2, h_env)

# Calculate the RMS of the envelope
```

```
47 rms = np.sqrt(np.power(h_envf1,2).mean())
48 # Calculate the Pearson correlation coefficient
49 prsn = st.pearsonr(h_envf1, h_envf2)[0]
50 # Show the rms and prsn correlation coefficient
51 print('The RMS is: {:.2f} and the Pearson correlation coefficient
      is: {:.2f}'.format(rms, prsn))
52 # Pattern classification
53 if rms > 0.28:
54    ptt = 'Churn'
55 elif prsn > 0.701:
56    ptt = 'Slug'
57 else:
58    ptt = 'Dispersed bubble'
59 print('The flow pattern is: {}'.format(ptt))
```

B Uncertainty analysis

B.1 Theory

According to Figliola and Beasley [48], experimental tests require a method to assess the results quality. In this context, the uncertainty analysis provides a methodical approach to estimating the quality of the results of a completed or not tests. The uncertainty describes an interval about the measured value that the true value must be within an arbitrary probability. This interval is due to the inability to know the true value, but only the measured value, which is subject to the different sources of errors. Thus, the uncertainty analysis is the process of identifying, quantifying and combining the errors [48].

According to Figliola and Beasley [48], in test engineering, it is commonly used a probability level of $95\,\%$ to report final uncertainties. It is equivalent to assuming the probability covered by two standard deviations. Moreover, it is assumed that the error has a normal distribution. Thus, in order to get the confidence interval for a given probability level, it used the Student's t-test, $t_{\nu>30,P}$, for measurements with the degree of freedom, v, lower than 30. On the other hand, for degrees of freedom higher than 30, it can be used the z-score or for a probability level of $95\,\%$ the t-test with $t_{\nu>30,95} \approx 2$.

B.1.1 Zero-order uncertainty

Figliola and Beasley [48] state that even when all errors are zero, the measured value is subjected to our ability to resolve the information provided by the instrument. This error is called zero-order uncertainty, u_0. It assumes that the only difference between the true value and the measured value are due to the instrument resolution and the other aspects of the measurement are perfectly controlled. Thus, according to Figliola and Beasley [48], the uncertainty interval for resolution uncertainty is given by

$$u_0 = \pm\frac{1}{2}\,resolution \quad (95\%). \tag{B.1}$$

The value of u_0 represent reasonably well the uncertainty interval on either side of the reading with a probability of $95\,\%$.

B.1.2 Systematic error

Figliola and Beasley [48] mentions that when an error remains constant in repeated measurement under fixed operating conditions, it is called systematic error. It can cause in the measurement high or low offsets from the true value of the measured variable. Moreover, due to its invariance,

it can be difficult to estimate the value of a systematic error or even recognise its presence. The systematic for a probability level of P is written as

$$\pm B = \pm t_{\nu,P}\, b \ (P\%). \tag{B.2}$$

The $t_{\nu,P}$ is the Student's t-test with a v degree of freedom with $P\%$ probability level.

The instrument uncertainty given by the manufacturer is an estimate of the expected uncertainty due to the instrument, and if no probability level is provided within it, a $95\,\%$ level can be assumed [48]. Important to note that calibration cannot eliminate the systematic error, but it can reduce the uncertainty.

B.1.3 Random error

The random error can be observed as the scattering of the measured data when repeated measurements are made with fixed operating conditions. The random error is introduced through measurement procedure and technique, the repeatability and resolution of the measurement system components, a temporal and spatial variation of the measured variable, and by the variations in the process operation and environmental conditions from which the measurements were taken [48].

The probable range of a random error is given by its random uncertainty. The random standard uncertainty, $s_{\overline{x}}$, is defined by the interval given by $\pm\, s_{\overline{x}}$ or $\pm P$, where

$$P = s_{\overline{x}} = \frac{s_x}{\sqrt{N}}, \tag{B.3}$$

where N is the number of samples and s_x is the standard deviation. Thus, the interval given by $\pm\, s_{\overline{x}}$ has a confidence level of one standard deviation, which is equivalent to a probability of $68\,\%$ for a population of x having a normal distribution. On the other hand, the random uncertainty at a desired confidence level is defined by $\pm t_{\nu,P}\, s_{\overline{x}}$ [48].

B.1.4 Combining errors

Figliola and Beasley [48] mention that each measurement error interacts with other errors, and then affect the overall measurement uncertainty. According to Figliola and Beasley [48], a realistic uncertainty estimation for the measured variable, u_x, can be computed using the RSS (root sum squared) method and it is given by

$$u_x = \sqrt{\sum_{k=1}^{k} u_k^2}, \tag{B.4}$$

where k is different errors.

B.1.5 Error propagation

In engineering the measured variable is often used to estimate another variable using a functional relationship with measured values. For instance, to estimate the air specific mass using the ideal gas law, by measuring the gas temperature and pressure. Thus, it may be desirable to compute the air specific mass uncertainty from the temperature and pressure uncertainties. Therefore, it is required to calculate how each transducer uncertainty affects the air specific mass uncertainty.

In order to simplify the analysis, suppose it is desired to compute the uncertainty of a dependent variable y from a measured variable x, thus $y = f(x)$. Then, considering that the combined systematic errors of the measured variable is given by $B_{\overline{x}}$. Therefore, it is reasonable to assume that the true value of y is in the interval defined by

$$\overline{y} \pm \delta y = f(\overline{x} \pm B_{\overline{x}}). \tag{B.5}$$

Expanding the equation B.5 as Taylor series,

$$\overline{y} \pm \delta y = f(\overline{x}) \pm \left[\left(\frac{dy}{dx} \right)_{x=\overline{x}} B_{\overline{x}} + \frac{1}{2} \left(\frac{d^2y}{dx^2} \right)_{x=\overline{x}} (B_{\overline{x}})^2 + \ldots \right]. \tag{B.6}$$

Analysing the equation B.6, it is perceptible that $\overline{y} = f(\overline{x})$, and the term inside the squared brackets estimate δy. Thus, considering that $B_{\overline{x}}$ is small, a linear approximation for δy, by neglecting the higher order terms of the Taylor series expansion, is reasonable. Therefore, δy is given by

$$\delta y \approx \left(\frac{dy}{dx} \right)_{x=\overline{x}} B_{\overline{x}}. \tag{B.7}$$

Hence δy is the x uncertainty propagated to y. Then, rewriting equation B.7 in terms of the uncertainties of x and y results in

$$u_y = \left(\frac{dy}{dx} \right)_{x=\overline{x}} u_x. \tag{B.8}$$

It was shown the error propagation for univariate function. However, the idea can be expanded for multivariate functions, for instance, the air specific mass, which is a function of pressure and temperature. Then, consider a function R, which is determined by a functional relationship between independent variables $x_1, x_2, \ldots, x_L$, defined by

$$R = f(x_1, x_2, \ldots, x_L). \tag{B.9}$$

Thus, the uncertainty of a given independent variable L, u_{x_L}, will propagate to R, $u_{R,L}$, similarly to equation B.8 but with a partial derivative. It is given by

$$u_{R,L} = \left(\frac{\partial R}{\partial x_L} \right)_{x=\overline{x}} u_{x_L} = \theta_L u_{x_L}. \tag{B.10}$$

Finally, it is possible to get the R uncertainty, by propagating each R independent variable uncertainty and combining them with equation B.4, which yields to

$$u_R = \left[\sum_{i=1}^{L} \left(\theta_i u_{x_i} \right)^2 \right]^{\frac{1}{2}}. \tag{B.11}$$

Moreover, the degree of freedom of the random error of multivariate functions is obtained by

$$\nu = \frac{\left[\sum_{i=1}^{L} \left(\theta_i u_{x_i} \right)^2 \right]^2}{\sum_{i=1}^{L} \frac{\left(\theta_i u_{x_i} \right)^4}{N-1}}, \tag{B.12}$$

where N is the sample number.

B.2 Transducers uncertainty

This section presents the uncertainty for each process variable transducer used. The transducers uncertainties will be used to propagate the error from the measured process variables to calculated two-phase flow properties.

As mentioned in Section 4.2, the sample rate used was of $10\,\mathrm{kHz}$ and according to Section 4.6 the data was acquired during $30\,\mathrm{s}$. Therefore, the number of samples for each process variable transducer was of $300\,000$.

B.2.1 PT-10X

According to the pressure transmitter manufacturer datasheet, the transducer accuracy is $0.065\,\%$ of the transducer range that is 0 to $1000\,\mathrm{kPa}$.

The uncertainty for the PT-10X transducers was separated into instrument uncertainty and measurement uncertainty. Then, after calculating the uncertainties of systematic and random errors for each case, it was calculated the total transducer uncertainty.

- Instrument uncertainty:
  - The transducer accuracy can be considered a systematic error. Then,

$$B_1 = 0.065 \cdot 10^{-2}(1000 \cdot 10^3 - 0) = 650\,\mathrm{Pa}; \tag{B.13}$$

  - The manufacturer did not provide the random error. Thus, $P_1 = 0$;
- Measurement uncertainty:
  - It was not possible to measure the systematic error for the measurements. Thus, $B_2 = 0$;

  - The random error can be estimated using the equation B.3. Thus,

$$P_2 = \frac{s_{P_{10X}}}{\sqrt{300\,000}}; \tag{B.14}$$

- Combining the systematic error and random error from the instrument and the measurement

$$B_{P_{10X}} = \left({B_1}^2 + {B_2}^2\right)^{\frac{1}{2}} = 650\,\mathrm{Pa}, \tag{B.15}$$

$$P_{P_{10X}} = \left({P_1}^2 + {P_2}^2\right)^{\frac{1}{2}} = \frac{s_{P_{10X}}}{\sqrt{300\,000}}. \tag{B.16}$$

As can be seen above, total transducer uncertainty depends on the measurement. Therefore, each acquisition will have a different uncertainty.

B.2.2 PDT-101

According to the pressure transmitter manufacturer datasheet, the transducer accuracy is $0.065\,\%$ of the transducer range that is 0 to $2\,\mathrm{kPa}$.

The uncertainty for the PDT-101 transducer was separated into instrument uncertainty and measurement uncertainty. Then, after calculating the uncertainties of systematic and random errors for each case, it was calculated the total transducer uncertainty.

- Instrument uncertainty:
  - The transducer accuracy can be considered a systematic error. Then,

$$B_1 = 0.065 \cdot 10^{-2}(2 \cdot 10^3 - 0) = 1.3\,\mathrm{Pa}; \tag{B.17}$$

  - The manufacturer did not provide the random error. Thus, $P_1 = 0$;

- Measurement uncertainty:
  - It was not possible to measure the systematic error for the measurements. Thus, $B_2 = 0$;
  - The random error can be estimated using the equation B.3. Thus,

$$P_2 = \frac{s_{P_{D101}}}{\sqrt{300\,000}}; \tag{B.18}$$

- Combining the systematic error and random error from the instrument and the measurement

$$B_{P_{D101}} = \left({B_1}^2 + {B_2}^2\right)^{\frac{1}{2}} = 1.3\,\mathrm{Pa}, \tag{B.19}$$

$$P_{P_{D101}} = \left({P_1}^2 + {P_2}^2\right)^{\frac{1}{2}} = \frac{s_{P_{D101}}}{\sqrt{300\,000}}. \tag{B.20}$$

As can be seen above, total transducer uncertainty depends on the measurement. Therefore, each acquisition will have a different uncertainty.

B.2.3 PT-301

According to the pressure transmitter manufacturer datasheet, the transducer accuracy is $0.04\,\%$ of the transducer range that is 0.1 to $48\,\mathrm{kPa}$.

The uncertainty for the PT-301 transducer was separated into instrument uncertainty and measurement uncertainty. Then, after calculating the uncertainties of systematic and random errors for each case, it was calculated the total transducer uncertainty.

- Instrument uncertainty:
  - The transducer accuracy can be considered a systematic error. Then,

$$B_1 = 0.04 \cdot 10^{-2}(48 \cdot 10^3 - 0.1 \cdot 10^3) = 19.16\,\mathrm{Pa}; \tag{B.21}$$

  - The manufacturer did not provide the random error. Thus, $P_1 = 0$;
- Measurement uncertainty:
  - It was not possible to measure the systematic error for the measurements. Thus, $B_2 = 0$;
  - The random error can be estimated using the equation B.3. Thus,

$$P_2 = \frac{s_{P_{301}}}{\sqrt{300\,000}}; \tag{B.22}$$

- Combining the systematic error and random error from the instrument and the measurement

$$B_{P_{301}} = \left({B_1}^2 + {B_2}^2\right)^{\frac{1}{2}} = 19.16\,\mathrm{Pa}, \tag{B.23}$$

$$P_{P_{301}} = \left({P_1}^2 + {P_2}^2\right)^{\frac{1}{2}} = \frac{s_{P_{301}}}{\sqrt{300\,000}}. \tag{B.24}$$

As can be seen above, total transducer uncertainty depends on the measurement. Therefore, each acquisition will have a different uncertainty.

B.2.4 TT-X0X

The resistance thermometer PT-100 has an accuracy that changes according to the measured temperature, $u_{\overline{T}}$. Thus, the uncertainty from systematic error will also depend on the measured temperature.

The uncertainty for the TT-X0X transducers was separated into instrument uncertainty and measurement uncertainty. Then, after calculating the uncertainties of systematic and random errors for each case, it was calculated the total transducer uncertainty.

- Instrument uncertainty:
  - The transducer accuracy can be considered a systematic error. Then,

$$B_1 = u_{\overline{T}}; \tag{B.25}$$

  - The manufacturer did not provide the random error. Thus, $P_1 = 0$;
- Measurement uncertainty:
  - It was not possible to measure the systematic error for the measurements. Thus, $B_2 = 0$;
  - The random error can be estimated using the equation B.3. Thus,

$$P_2 = \frac{s_{T_{X0X}}}{\sqrt{300\,000}}; \tag{B.26}$$

- Combining the systematic error and random error from the instrument and the measurement

$$B_{T_{X0X}} = \left({B_1}^2 + {B_2}^2\right)^{\frac{1}{2}} = u_{\overline{T}}, \tag{B.27}$$

$$P_{T_{X0X}} = \left({P_1}^2 + {P_2}^2\right)^{\frac{1}{2}} = \frac{s_{T_{X0X}}}{\sqrt{300\,000}}. \tag{B.28}$$

As can be seen above, total transducer uncertainty depends on the measurement. Therefore, each acquisition will have a different uncertainty.

B.2.5 FT-101

According to the flow transmitter manufacturer datasheet, the transducer accuracy is $0.5\,\%$ of the measured value, $\overline{x}$.

The uncertainty for the FT-101 transducer was separated into instrument uncertainty and measurement uncertainty. Then, after calculating the uncertainties of systematic and random errors for each case, it was calculated the total transducer uncertainty.

- Instrument uncertainty:
  - The transducer accuracy can be considered a systematic error. Then,

$$B_1 = 0.5 \cdot 10^{-2}\,\overline{x}; \tag{B.29}$$

  - The manufacturer did not provide the random error. Thus, $P_1 = 0$;

- Measurement uncertainty:

  - It was not possible to measure the systematic error for the measurements. Thus, $B_2 = 0$;
  - The random error can be estimated using the equation B.3. Thus,

$$P_2 = \frac{s_{F_{101}}}{\sqrt{300\,000}}; \tag{B.30}$$

- Combining the systematic error and random error from the instrument and the measurement

$$B_{F_{101}} = \left({B_1}^2 + {B_2}^2\right)^{\frac{1}{2}} = 0.5 \cdot 10^{-2}\,\overline{x}, \tag{B.31}$$

$$P_{F_{101}} = \left({P_1}^2 + {P_2}^2\right)^{\frac{1}{2}} = \frac{s_{F_{101}}}{\sqrt{300\,000}}. \tag{B.32}$$

As can be seen above, total transducer uncertainty depends on the measurement. Therefore, each acquisition will have a different uncertainty.

B.3 Error propagation

This section presents the error propagation for each two-phase flow property calculated and used in this work. It will be based on the uncertainties obtained from Section B.2. Besides, as the two-phase properties will be calculated near the second vibration measurement station, the errors will be propagated to the transducers near it.

As mentioned in Section B.2, the transducers uncertainties depend on the measured value. Therefore, this section will only propagate the error, and the calculated uncertainty for each acquisition will be presented in the further section.

B.3.1 Diameter

The pipe has a diameter, d, of $52.5\,\mathrm{mm}$. According to the pipe manufacturer, the diameter uncertainty is of $\pm 1\,\%$. It can be considered a systematic error. Then,

$$B_d = 1 \cdot 10^{-2}\,0.0525 = 0.000\,525\,\mathrm{m}. \tag{B.33}$$

The manufacturer did not provide the random error. Thus, $P_d = 0$. Therefore, the diameter uncertainty is given by

$$d = \overline{d} \pm B_d. \tag{B.34}$$

B.3.2 Liquid specific mass

Due to the pipeline operating pressure, the water compressibility effect was neglected. Thus, it was used the equation proposed by Jones and Harris [79] to obtain the water specific mass as a function solely of temperature. The function is given as

$$\rho_L = -3.821216{\cdot}10^{-7}T^4+6.943248{\cdot}10^{-5}T^3-8.523829{\cdot}10^{-3}T^2+6.32693{\cdot}10^{-2}T+999.85308, \tag{B.35}$$

where T is the measured temperature. The equation B.35 derivative is given by

$$\frac{d\rho_L}{dT} = -15.284864{\cdot}10^{-7}T^3+20.829744{\cdot}10^{-5}T^2-17.047658{\cdot}10^{-3}T+6.32693{\cdot}10^{-2}. \tag{B.36}$$

Thus, the systematic error is given by

$$B_{\rho_L} = \left[\left(\left.\frac{d\rho_L}{dT}\right|_{\overline{T}_{301}} B_{T_{301}}\right)^2\right]^{\frac{1}{2}} = \left.\frac{d\rho_L}{dT}\right|_{\overline{T}_{301}} B_{T_{301}}. \tag{B.37}$$

The random error is given by

$$P_{\rho_L} = \left[\left(\left.\frac{d\rho_L}{dT}\right|_{\overline{T}_{301}} P_{T_{301}}\right)^2\right]^{\frac{1}{2}} = \left.\frac{d\rho_L}{dT}\right|_{\overline{T}_{301}} P_{T_{301}}. \tag{B.38}$$

Once the equation B.35 is a univariate function, the degree of freedom according to the equation B.12 is $N-1 = 299\,999$. Moreover, as the degree of freedom is higher than 30, $t_{\nu,95} = 2$. Thus, the liquid specific mass uncertainty is given by

$$\rho_L = \overline{\rho}_L \pm (B_{\rho_L} + 2P_{\rho_L}) \tag{B.39}$$

B.3.3 Gas specific mass

The air specific mass,ρ_G, can be obtained by using the ideal gas law given by

$$PV = mRT \quad \therefore \quad \rho_G = \frac{P}{RT}, \tag{B.40}$$

where P is the gas pressure, V is the gas volume, m is the gas mass, R is the gas constant, and T is the gas temperature. The equation B.40 partial derivatives are

$$\frac{\partial\rho_G}{\partial P} = \frac{1}{RT}, \tag{B.41}$$

$$\frac{\partial\rho_G}{\partial T} = -\frac{P}{RT^2}, \tag{B.42}$$

Thus, the systematic error is given by

$$B_{\rho_G} = \left[\left(\frac{\partial \rho_G}{\partial P}\bigg|_{\overline{T}_{301}} B_{P_{301}} \right)^2 + \left(\frac{\partial \rho_G}{dT}\bigg|_{\overline{T}_{301},\overline{P}_{301}} B_{T_{301}} \right)^2 \right]^{\frac{1}{2}}. \tag{B.43}$$

The random error is given by

$$P_{\rho_G} = \left[\left(\frac{\partial \rho_G}{\partial P}\bigg|_{\overline{T}_{301}} P_{P_{301}} \right)^2 + \left(\frac{\partial \rho_G}{\partial T}\bigg|_{\overline{T}_{301},\overline{P}_{301}} P_{T_{301}} \right)^2 \right]^{\frac{1}{2}}. \tag{B.44}$$

The degree of freedom is given by equation B.12. Considering

$$\lambda = \left(\frac{\partial \rho_G}{\partial P}\bigg|_{\overline{T}_{301}} P_{P_{301}} \right)^2$$

and

$$\xi = \left(\frac{\partial \rho_G}{\partial T}\bigg|_{\overline{T}_{301},\overline{P}_{301}} P_{T_{301}} \right)^2,$$

the air specific mass degree of freedom is given by

$$\nu_{\rho_G} = \frac{[\lambda + \xi]^2}{\frac{\lambda^2}{N-1} + \frac{\xi^2}{N-1}}. \tag{B.45}$$

Then, the air specific mass uncertainty is given by

$$\rho_G = \overline{\rho}_G \pm (B_{\rho_G} + t_{\nu_{\rho_G},95} P_{\rho_G}). \tag{B.46}$$

B.3.4 Liquid viscosity

Due to the pipeline operating pressure, the water compressibility effect was neglected. Thus, it was used the equation proposed by White [80] to obtain the water viscosity as a function solely of temperature. The function is given as

$$\mu_L = \mu_0 e^{7.0032z^2 - 5.306z - 1.704}, \quad z = \frac{273.15}{T} \quad \text{and} \quad \mu_0 = 1.788\,10^{-3}\mathrm{Pa\,s}. \tag{B.47}$$

The temperature in equation B.47 is in Kelvin. Thus, the equation B.47 derivative is given by

$$\frac{d\mu_L}{dT} = \mu_0 \left(-14.006 \frac{273.15^2}{T^3} + 5.306 \frac{273.15}{T^2} \right) e^{7.0032z^2 - 5.306z - 1.704} \tag{B.48}$$

Thus, the systematic error is given by

$$B_{\mu_L} = \left[\left(\left. \frac{d\mu_L}{dT} \right|_{\overline{T}_{301}} B_{T_{301}} \right)^2 \right]^{\frac{1}{2}} = \left. \frac{d\mu_L}{dT} \right|_{\overline{T}_{301}} B_{T_{301}}. \tag{B.49}$$

The random error is given by

$$P_{\mu_L} = \left[\left(\left. \frac{d\mu_L}{dT} \right|_{\overline{T}_{301}} P_{T_{301}} \right)^2 \right]^{\frac{1}{2}} = \left. \frac{d\mu_L}{dT} \right|_{\overline{T}_{301}} P_{T_{301}}. \tag{B.50}$$

Once the equation B.47 is a univariate function, the degree of freedom according to the equation B.12 is $N - 1 = 299\,999$. Moreover, as the degree of freedom is higher than 30, $t_{\nu,95} = 2$. Thus, the liquid viscosity uncertainty is given by

$$\mu_L = \overline{\mu}_L \pm (B_{\mu_L} + 2P_{\mu_L}) \tag{B.51}$$

B.3.5 Gas viscosity

The gas viscosity was estimated using the Sutherland law where the air viscosity can be obtained by

$$\mu_G = \mu_0 \left(\frac{T}{T_0} \right)^{\frac{3}{2}} \left(\frac{T_0 + S}{T + S} \right), \tag{B.52}$$

where $S = 110.4\,\mathrm{K}$, $T_0 = 273.15\,\mathrm{K}$ and $\mu_0 = 1.71\,10^{-5}\mathrm{Pa\,s}$. Thus, the equation B.52 derivative is given by

$$\frac{d\mu_G}{dT} = \frac{\mu_0 \sqrt{T}(T + 3S)(T_0 + S)}{2T_0^{\frac{3}{2}}(T + S)^2}. \tag{B.53}$$

Thus, the systematic error is given by

$$B_{\mu_G} = \left[\left(\left. \frac{d\mu_G}{dT} \right|_{\overline{T}_{301}} B_{T_{301}} \right)^2 \right]^{\frac{1}{2}} = \left. \frac{d\mu_G}{dT} \right|_{\overline{T}_{301}} B_{T_{301}}. \tag{B.54}$$

The random error is given by

$$P_{\mu_G} = \left[\left(\left. \frac{d\mu_G}{dT} \right|_{\overline{T}_{301}} P_{T_{301}} \right)^2 \right]^{\frac{1}{2}} = \left. \frac{d\mu_G}{dT} \right|_{\overline{T}_{301}} P_{T_{301}}. \tag{B.55}$$

Once the equation B.52 is a univariate function, the degree of freedom according to the equation B.12 is $N - 1 = 299\,999$. Moreover, as the degree of freedom is higher than 30, $t_{\nu,95} = 2$. Thus, the gas viscosity uncertainty is given by

$$\mu_G = \overline{\mu}_G \pm (B_{\mu_G} + 2P_{\mu_G}) \tag{B.56}$$

B.3.6 Liquid superficial velocity

By definition, the liquid superficial velocity is expressed as

$$v_{SL} = \frac{q_L}{A}, \tag{B.57}$$

where

$$q_L = \frac{W_L}{60\rho_L} \quad \text{and} \quad A = \frac{\pi d^2}{4}. \tag{B.58}$$

Thus, the v_{SL} can be written as function of liquid mass flow rate, W_L, liquid specific mass, ρ_L, and the diameter, d. Then, it is given as

$$v_{SL} = \frac{4W_L}{60\rho_L \pi d^2}. \tag{B.59}$$

Therefore, the equation B.59 partial derivatives are

$$\frac{\partial v_{SL}}{\partial W_L} = \frac{4}{60\rho_L \pi d^2}, \tag{B.60}$$

$$\frac{\partial v_{SL}}{\partial \rho_L} = -\frac{4W_L}{60{\rho_L}^2 \pi d^2}, \tag{B.61}$$

$$\frac{\partial v_{SL}}{\partial d} = -\frac{8W_L}{60\rho_L \pi d^3}. \tag{B.62}$$

Thus, the systematic error is given by

$$B_{v_{SL}} = \left[\left(\left.\frac{\partial v_{SL}}{\partial W_L}\right|_{\overline{\rho}_L} B_{F_{101}} \right)^2 + \left(\left.\frac{\partial v_{SL}}{\partial \rho_L}\right|_{\overline{W}_L, \overline{\rho}_L} B_{\rho_L} \right)^2 + \left(\left.\frac{\partial v_{SL}}{\partial d}\right|_{\overline{W}_L, \overline{\rho}_L} B_d \right)^2 \right]^{\frac{1}{2}}. \tag{B.63}$$

The random error is given by

$$P_{v_{SL}} = \left[\left(\left.\frac{\partial v_{SL}}{\partial W_L}\right|_{\overline{\rho}_L} P_{F_{101}} \right)^2 + \left(\left.\frac{\partial v_{SL}}{\partial \rho_L}\right|_{\overline{W}_L, \overline{\rho}_L} P_{\rho_L} \right)^2 \right]^{\frac{1}{2}}. \tag{B.64}$$

The degree of freedom is given by equation B.12. Considering

$$\lambda = \left(\left.\frac{\partial v_{SL}}{\partial W_L}\right|_{\overline{\rho}_L} P_{F_{101}} \right)^2$$

and

$$\xi = \left(\frac{\partial v_{SL}}{\partial \rho_L}\bigg|_{\overline{W}_L, \overline{\rho}_L} P_{\rho_L} \right)^2,$$

the liquid superficial velocity degree of freedom is given by

$$\nu_{v_{SL}} = \frac{[\lambda + \xi]^2}{\frac{\lambda^2}{N-1} + \frac{\xi^2}{N-1}}. \tag{B.65}$$

Then, the liquid superficial velocity uncertainty is given by

$$v_{SL} = \overline{v}_{SL} \pm (B_{v_{SL}} + t_{\nu_{v_{SL}},95} P_{v_{SL}}). \tag{B.66}$$

B.3.7 Gas superficial velocity

The laminar flow element calibration curve states that the air volumetric flow rate is related to pressure drop as follows,

$$q_{laminar} = 1.894694615 \cdot 10^{-6} P_{D101}, \tag{B.67}$$

where P_{D101} is the differential pressure measured by the PDT-101 transducer. Moreover, as presented in Section 4.1, the laminar flow element is placed at the bottom of the experimental apparatus. On the other hand, it is required to calculate the two-phase properties near the second vibration measurement station. Thus, to account the air expansion between the laminar flow element and near the second vibration measurement station, it was used the ideal gas law. The expansion correction can be obtained by

$$q_y = \frac{P_x T_y}{P_y T_x} q_x \therefore q_G = \frac{P_{101} T_{301}}{P_{301} T_{101}} q_{laminar}, \tag{B.68}$$

where P is the pressure, T is the temperature in Kelvin, and q is the volumetric flow rate. The subscripts x and y indicate the different measurement points.

By definition, the gas superficial velocity is expressed as

$$v_{SG} = \frac{q_G}{A}, \tag{B.69}$$

where

$$A = \frac{\pi d^2}{4}, \tag{B.70}$$

q_G is the gas volumetric flow rate, and d is the pipe diameter. Rewriting the equation B.69 by replacing the equations B.68 and equation B.70, it is obtained

$$v_{SG} = \frac{4 P_{101} T_{301} 1.894694615 \cdot 10^{-6} P_{D101}}{\pi d^2 P_{301} T_{101}}. \tag{B.71}$$

Therefore, the equation B.71 partial derivatives are

$$\frac{\partial v_{SG}}{\partial P_{101}} = \frac{4T_{301}1.894694615 \cdot 10^{-6}P_{D101}}{\pi d^2 P_{301}T_{101}}, \tag{B.72}$$

$$\frac{\partial v_{SG}}{\partial T_{301}} = \frac{4P_{101}1.894694615 \cdot 10^{-6}P_{D101}}{\pi d^2 P_{301}T_{101}}, \tag{B.73}$$

$$\frac{\partial v_{SG}}{\partial P_{D101}} = \frac{4P_{101}T_{301}1.894694615 \cdot 10^{-6}}{\pi d^2 P_{301}T_{101}}, \tag{B.74}$$

$$\frac{\partial v_{SG}}{\partial P_{301}} = -\frac{4P_{101}T_{301}1.894694615 \cdot 10^{-6}P_{D101}}{\pi d^2 P_{301}^2 T_{101}}, \tag{B.75}$$

$$\frac{\partial v_{SG}}{\partial T_{101}} = -\frac{4P_{101}T_{301}1.894694615 \cdot 10^{-6}P_{D101}}{\pi d^2 P_{301}T_{101}^2}, \tag{B.76}$$

$$\frac{\partial v_{SG}}{\partial d} = -\frac{8P_{101}T_{301}1.894694615 \cdot 10^{-6}P_{D101}}{\pi d^3 P_{301}T_{101}}. \tag{B.77}$$

Thus, the systematic error is given by

$$\begin{aligned} B_{v_{SG}} = \Bigg[&\left(\frac{\partial v_{SG}}{\partial P_{101}}\bigg|_{\overline{X}_a} B_{P_{101}} \right)^2 + \left(\frac{\partial v_{SG}}{\partial T_{301}}\bigg|_{\overline{X}_b} B_{T_{301}} \right)^2 + \left(\frac{\partial v_{SG}}{\partial P_{D101}}\bigg|_{\overline{X}_c} B_{P_{D101}} \right)^2 + \\ &+ \left(\frac{\partial v_{SG}}{\partial P_{301}}\bigg|_{\overline{X}_d} B_{P_{301}} \right)^2 + \left(\frac{\partial v_{SG}}{\partial T_{101}}\bigg|_{\overline{X}_e} B_{T_{101}} \right)^2 + \left(\frac{\partial v_{SG}}{\partial d}\bigg|_{\overline{X}_f} B_d \right)^2 \Bigg]^{\frac{1}{2}}. \end{aligned} \tag{B.78}$$

The random error is given by

$$\begin{aligned} P_{v_{SG}} = \Bigg[&\left(\frac{\partial v_{SG}}{\partial P_{101}}\bigg|_{\overline{X}_a} P_{P_{101}} \right)^2 + \left(\frac{\partial v_{SG}}{\partial T_{301}}\bigg|_{\overline{X}_b} P_{T_{301}} \right)^2 + \left(\frac{\partial v_{SG}}{\partial P_{D101}}\bigg|_{\overline{X}_c} P_{P_{D101}} \right)^2 + \\ &+ \left(\frac{\partial v_{SG}}{\partial P_{301}}\bigg|_{\overline{X}_d} PB_{P_{301}} \right)^2 + \left(\frac{\partial v_{SG}}{\partial T_{101}}\bigg|_{\overline{X}_e} P_{T_{101}} \right)^2 \Bigg]^{\frac{1}{2}}. \end{aligned} \tag{B.79}$$

The $\overline{X}_x$ means the partial derivative at a given location. Hence, $\overline{X}_a = \{\overline{T}_{301}, \overline{P}_{D101}, \overline{P}_{301}, \overline{T}_{101}\}$, $\overline{X}_b = \{\overline{P}_{101}, \overline{P}_{D101}, \overline{P}_{301}, \overline{T}_{101}\}$, $\overline{X}_c = \{\overline{T}_{301}, \overline{P}_{101}, \overline{P}_{301}, \overline{T}_{101}\}$ and $\overline{X}_d = \overline{X}_e = \overline{X}_f = \{\overline{T}_{301}, \overline{P}_{101}, \overline{P}_{D101}, \overline{P}_{301}, \overline{T}_{101}\}$. The degree of freedom is given by equation B.12. Considering

$$\lambda = \left(\frac{\partial v_{SG}}{\partial P_{101}}\bigg|_{\overline{X}_a} P_{P_{101}} \right)^2, \quad \xi = \left(\frac{\partial v_{SG}}{\partial T_{301}}\bigg|_{\overline{X}_b} P_{T_{301}} \right)^2, \quad \gamma = \left(\frac{\partial v_{SG}}{\partial P_{D101}}\bigg|_{\overline{X}_c} P_{P_{D101}} \right)^2,$$

$$\omega = \left(\frac{\partial v_{SG}}{\partial P_{301}}\bigg|_{\overline{X}_d} P_{P_{301}} \right)^2, \quad \text{and} \quad \eta = \left(\frac{\partial v_{SG}}{\partial T_{101}}\bigg|_{\overline{X}_e} P_{T_{101}} \right)^2,$$

the gas superficial velocity degree of freedom is given by

$$\nu_{v_{SG}} = \frac{\left[\lambda + \xi + \gamma + \omega + \eta\right]^2}{\frac{\lambda^2}{N-1} + \frac{\gamma^2}{N-1} + \frac{\omega^2}{N-1} + \frac{\eta^2}{N-1}}. \tag{B.80}$$

Then, the gas superficial velocity uncertainty is given by

$$v_{SG} = \overline{v}_{SG} \pm (B_{v_{SG}} + t_{\nu_{v_{SG}},95} P_{v_{SG}}). \tag{B.81}$$

B.3.8 Mixture velocity

By definition, the mixture velocity is expressed as

$$v_M = v_{SL} + v_{SG}. \tag{B.82}$$

It is observable that the partial derivatives of the equation B.82 are 1 for either variables. Thus, the systematic error is given by

$$B_{v_M} = \left[{B_{v_{SL}}}^2 + {B_{v_{SG}}}^2 \right]^{\frac{1}{2}}. \tag{B.83}$$

Then, the random error is given by

$$P_{v_M} = \left[{P_{v_{SL}}}^2 + {P_{v_{SG}}}^2 \right]^{\frac{1}{2}}. \tag{B.84}$$

The degree of freedom is given by equation B.12. Thus, the mixture velocity degree of freedom is given by

$$\nu_{v_M} = \frac{\left[{P_{v_{SL}}}^2 + {P_{v_{SG}}}^2 \right]^2}{\frac{{P_{v_{SL}}}^4}{N-1} + \frac{{P_{v_{SG}}}^4}{N-1}}. \tag{B.85}$$

Then, the mixture velocity uncertainty is given by

$$v_M = \overline{v}_M \pm (B_{v_M} + t_{\nu_{v_M},95} P_{v_M}). \tag{B.86}$$

B.3.9 Measured GVF

The fast-closing system uses the hydrostatic pressure of the liquid trapped inside it to estimate the two-phase flow gas void fraction. The hydrostatic pressure is obtained using the PT-301 transducer. Hence, by using the calculated liquid specific mass, it is possible to estimate the liquid height. Then, with the fast-closing system length, it is possible to estimate the gas void

fraction. The GVF, α_{fc}, is the ratio of liquid height, h, with the fast-closing system length, h_{fc}. This ratio is expressed as

$$\alpha_{fc} = 1 - \frac{h}{h_{fc}}. \tag{B.87}$$

Moreover, the liquid height as a function of the hydrostatic pressure is given as

$$h = \frac{P_{301}}{\rho_L g}, \tag{B.88}$$

where g is the gravity. Finally, combining and rearranging the equations B.87 and B.88, it is possible to obtain the following expression

$$\alpha_{fc} = 1 - \frac{P}{\rho_L h_{fc} g} \tag{B.89}$$

Therefore, the equation B.89 partial derivatives are

$$\frac{\partial \alpha_{fc}}{\partial P_{301}} = -\frac{1}{\rho_L h_{fc} g}, \tag{B.90}$$

$$\frac{\partial \alpha_{fc}}{\partial \rho_L} = \frac{P_{301}}{{\rho_L}^2 h_{fc} g}, \tag{B.91}$$

$$\frac{\partial \alpha_{fc}}{\partial h_{fc}} = \frac{P_{301}}{\rho_L {h_{fc}}^2 g}. \tag{B.92}$$

The uncertainty of the fast-closing system length is $\pm 0.5\,\mathrm{mm}$. It can be considered a systematic error. Then,

$$B_{h_{fc}} = 0.0005\,\mathrm{m}. \tag{B.93}$$

It was not accounted the random error from the fast-closing system length measurements. Thus, $P_{h_{fc}} = 0$. Therefore, the diameter uncertainty is given by

$$h_{fc} = \overline{h}_{fc} \pm B_{h_{fc}}. \tag{B.94}$$

Thus, the systematic error for the measured GVF is given by

$$B_{\alpha_{fc}} = \left[\left(\frac{\partial \alpha_{fc}}{\partial P_{301}}\bigg|_{\overline{\rho}_L, \overline{h}_{fc}} B_{P_{301}} \right)^2 + \left(\frac{\partial \alpha_{fc}}{\partial \rho_L}\bigg|_{\overline{X}_a} B_{\rho_L} \right)^2 + \left(\frac{\partial \alpha_{fc}}{\partial h_{fc}}\bigg|_{\overline{X}_a} B_{h_{fc}} \right)^2 \right]^{\frac{1}{2}}. \tag{B.95}$$

The $\overline{X}_a$ means the partial derivative at $\{\overline{P}_{301}, \overline{\rho}_L, \overline{h}_{fc}\}$.

As the two-phase flow is considered pseudo-permanent and it is required to trap the flow to measure the GVF. It is possible that the flow trapped within the fast-closing system is not a

reasonable sample from the flow. In order to estimate the GVF more accurately, it was performed four repetitions, as mentioned in Section 4.7. Therefore, it is also required to account for the random error from trapping the flow. Thus, it was used the equation B.3 to estimate a random error for the repetitions. It is given by

$$P_{rep} = \frac{s_{rep}}{\sqrt{4}}. \tag{B.96}$$

The measured GVF random error is given by

$$P_{\alpha_{fc}} = \left[\left(\frac{\partial \alpha_{fc}}{\partial P_{301}}\bigg|_{\overline{\rho}_L, \overline{h}_{fc}} P_{P_{301}} \right)^2 + \left(\frac{\partial \alpha_{fc}}{\partial \rho_L}\bigg|_{\overline{X}_a} P_{\rho_L} \right)^2 + \left(\frac{\partial \alpha_{fc}}{\partial h_{fc}}\bigg|_{\overline{X}_a} P_{h_{fc}} \right)^2 + {P_{rep}}^2 \right]^{\frac{1}{2}}. \tag{B.97}$$

The degree of freedom is given by equation B.12. Considering

$$\lambda = \left(\frac{\partial \alpha_{fc}}{\partial P_{301}}\bigg|_{\overline{\rho}_L, \overline{h}_{fc}} P_{P_{301}} \right)^2, \quad \xi = \left(\frac{\partial \alpha_{fc}}{\partial \rho_L}\bigg|_{\overline{X}_a} P_{\rho_L} \right)^2,$$

$$\gamma = \left(\frac{\partial \alpha_{fc}}{\partial h_{fc}}\bigg|_{\overline{X}_a} P_{h_{fc}} \right)^2, \quad \text{and} \quad \omega = {P_{rep}}^2,$$

the measured GVF degree of freedom is given by

$$\nu_{\alpha_{fc}} = \frac{[\lambda + \xi + \gamma + \omega]^2}{\frac{\lambda^2}{N-1} + \frac{\xi^2}{N-1} + \frac{\gamma^2}{N-1} + \frac{\omega^2}{3}}. \tag{B.98}$$

Then, the measured GVF uncertainty is given by

$$\alpha_{fc} = \overline{\alpha}_{fc} \pm (B_{\alpha_{fc}} + t_{\nu_{\alpha_{fc}}, 95} P_{\alpha_{fc}}). \tag{B.99}$$

B.3.10 Homogeneous GVF

By definition, the homogeneous gas void fraction is expressed as

$$\alpha = \frac{v_{SG}}{v_{SG} + v_{SL}}. \tag{B.100}$$

Therefore, the equation B.100 partial derivatives are

$$\frac{\partial \alpha}{\partial v_{SL}} = -\frac{v_{SG}}{(v_{SG} + v_{SL})^2}, \tag{B.101}$$

$$\frac{\partial \alpha}{\partial v_{SG}} = \frac{v_{SL}}{(v_{SG} + v_{SL})^2}. \tag{B.102}$$

Thus, the systematic error is given by

$$B_\alpha = \left[\left(\frac{\partial \alpha}{\partial v_{SL}} \bigg|_{\overline{v}_{SL}, \overline{v}_{SG}} B_{v_{SL}} \right)^2 + \left(\frac{\partial \alpha}{\partial v_{SG}} \bigg|_{\overline{v}_{SL}, \overline{v}_{SG}} B_{v_{SG}} \right)^2 \right]^{\frac{1}{2}}. \tag{B.103}$$

The random error is given by

$$P_\alpha = \left[\left(\frac{\partial \alpha}{\partial v_{SL}} \bigg|_{\overline{v}_{SL}, \overline{v}_{SG}} P_{v_{SL}} \right)^2 + \left(\frac{\partial \alpha}{\partial v_{SG}} \bigg|_{\overline{v}_{SL}, \overline{v}_{SG}} P_{v_{SG}} \right)^2 \right]^{\frac{1}{2}}. \tag{B.104}$$

The degree of freedom is given by equation B.12. Considering

$$\lambda = \left(\frac{\partial \alpha}{\partial v_{SL}} \bigg|_{\overline{v}_{SL}, \overline{v}_{SG}} P_{v_{SL}} \right)^2$$

and

$$\xi = \left(\frac{\partial \alpha}{\partial v_{SG}} \bigg|_{\overline{v}_{SL}, \overline{v}_{SG}} P_{v_{SG}} \right)^2,$$

the homogeneous GVF degree of freedom is given by

$$\nu_\alpha = \frac{[\lambda + \xi]^2}{\frac{\lambda^2}{N-1} + \frac{\xi^2}{N-1}}. \tag{B.105}$$

Then, the homogeneous GVF uncertainty is given by

$$\alpha = \overline{\alpha} \pm (B_\alpha + t_{\nu_\alpha, 95} P_\alpha). \tag{B.106}$$

B.3.11 Mixture specific mass

By definition, the mixture specific mass is expressed as

$$\rho_M = \rho_L(1 - \alpha) + \rho_G \alpha. \tag{B.107}$$

Therefore, the equation B.100 partial derivatives are

$$\frac{\partial \rho_M}{\partial \rho_L} = 1 - \alpha, \tag{B.108}$$

$$\frac{\partial \rho_M}{\partial \rho_G} = \alpha, \tag{B.109}$$

$$\frac{\partial \rho_M}{\partial \alpha} = \rho_G - \rho_L. \tag{B.110}$$

Thus, the systematic error is given by

$$B_{\rho_M} = \left[\left((1-\overline{\alpha}) B_{\rho_L} \right)^2 + \left(\overline{\alpha} B_{\rho_G} \right)^2 + \left((\overline{\rho}_G - \overline{\rho}_L) B_\alpha \right)^2 \right]^{\frac{1}{2}}. \tag{B.111}$$

The random error is given by

$$P_{\rho_M} = \left[\left((1-\overline{\alpha}) P_{\rho_L} \right)^2 + \left(\overline{\alpha} P_{\rho_G} \right)^2 + \left((\overline{\rho}_G - \overline{\rho}_L) P_\alpha \right)^2 \right]^{\frac{1}{2}}. \tag{B.112}$$

The degree of freedom is given by equation B.12. Considering

$$\lambda = \left((1-\overline{\alpha}) P_{\rho_L} \right)^2, \quad \xi = \left(\overline{\alpha} P_{\rho_G} \right)^2 \quad \text{and} \quad \gamma = \left((\overline{\rho}_G - \overline{\rho}_L) P_\alpha \right)^2,$$

the mixture specific mass degree of freedom is given by

$$\nu_{\rho_M} = \frac{\left[\lambda + \xi + \gamma \right]^2}{\frac{\lambda^2}{N-1} + \frac{\xi^2}{N-1} + \frac{\gamma^2}{N-1}}. \tag{B.113}$$

Then, the mixture specific mass uncertainty is given by

$$\rho_M = \overline{\rho}_M \pm (B_{\rho_M} + t_{\nu_{\rho_M},95} P_{\rho_M}). \tag{B.114}$$

B.3.12 Mixture viscosity

By definition, the mixture viscosity is expressed as

$$\mu_M = \mu_L (1-\alpha) + \mu_G \alpha. \tag{B.115}$$

Therefore, the equation B.100 partial derivatives are

$$\frac{\partial \mu_M}{\partial \mu_L} = 1 - \alpha, \tag{B.116}$$

$$\frac{\partial \mu_M}{\partial \mu_G} = \alpha, \tag{B.117}$$

$$\frac{\partial \mu_M}{\partial \alpha} = \mu_G - \mu_L. \tag{B.118}$$

Thus, the systematic error is given by

$$B_{\mu_M} = \left[\left((1-\overline{\alpha}) B_{\mu_L} \right)^2 + \left(\overline{\alpha} B_{\mu_G} \right)^2 + \left((\overline{\mu}_G - \overline{\mu}_L) B_\alpha \right)^2 \right]^{\frac{1}{2}}. \tag{B.119}$$

The random error is given by

$$P_{\mu_M} = \left[\left((1-\overline{\alpha}) P_{\mu_L} \right)^2 + \left(\overline{\alpha} P_{\mu_G} \right)^2 + \left((\overline{\mu}_G - \overline{\mu}_L) P_\alpha \right)^2 \right]^{\frac{1}{2}}. \tag{B.120}$$

The degree of freedom is given by equation B.12. Considering

$$\lambda = \left((1-\overline{\alpha})P_{\mu_L}\right)^2, \quad \xi = \left(\overline{\alpha}P_{\mu_G}\right)^2 \quad \text{and} \quad \gamma = \left((\overline{\mu}_G - \overline{\mu}_L)P_\alpha\right)^2,$$

the mixture viscosity degree of freedom is given by

$$\nu_{\mu_M} = \frac{\left[\lambda + \xi + \gamma\right]^2}{\frac{\lambda^2}{N-1} + \frac{\xi^2}{N-1} + \frac{\gamma^2}{N-1}}. \tag{B.121}$$

Then, the mixture viscosity uncertainty is given by

$$\mu_M = \overline{\mu}_M \pm (B_{\mu_M} + t_{\nu_{\mu_M},95}P_{\mu_M}). \tag{B.122}$$

B.3.13 Mixture Reynolds number

By definition, the mixture Reynolds number is expressed as

$$Re_M = \frac{\rho_M v_M d}{\mu_M}. \tag{B.123}$$

Therefore, the equation B.100 partial derivatives are

$$\frac{\partial Re_M}{\partial \rho_M} = \frac{v_M d}{\mu_M}, \tag{B.124}$$

$$\frac{\partial Re_M}{\partial v_M} = \frac{\rho_M d}{\mu_M}, \tag{B.125}$$

$$\frac{\partial Re_M}{\partial d} = \frac{\rho_M v_M}{\mu_M}, \tag{B.126}$$

$$\frac{\partial Re_M}{\partial \mu_M} = -\frac{\rho_M v_M d}{{\mu_M}^2}. \tag{B.127}$$

Thus, the systematic error is given by

$$\begin{aligned} B_{Re_M} = \Bigg[&\left(\frac{\partial Re_M}{\partial \rho_M}\bigg|_{\overline{X}_a} B_{\rho_M} \right)^2 + \left(\frac{\partial Re_M}{\partial v_M}\bigg|_{\overline{X}_b} B_{v_M} \right)^2 + \left(\frac{\partial Re_M}{\partial d}\bigg|_{\overline{X}_c} B_d \right)^2 + \\ &+ \left(\frac{\partial Re_M}{\partial \mu_M}\bigg|_{\overline{X}_d} B_{\mu_M} \right)^2 \Bigg]^{\frac{1}{2}}. \end{aligned} \tag{B.128}$$

The random error is given by

$$P_{Re_M} = \left[\left(\frac{\partial Re_M}{\partial \rho_M}\bigg|_{\overline{X}_a} P_{\rho_M} \right)^2 + \left(\frac{\partial Re_M}{\partial v_M}\bigg|_{\overline{X}_b} P_{v_M} \right)^2 + \left(\frac{\partial Re_M}{\partial \mu_M}\bigg|_{\overline{X}_d} P_{\mu_M} \right)^2 \right]^{\frac{1}{2}}. \tag{B.129}$$

The $\overline{X}_x$ means the partial derivative at a given location. Hence, $\overline{X}_a = \{\overline{v}_M, \overline{\mu}_M\}$, $\overline{X}_b = \{\overline{\rho}_M, \overline{\mu}_M\}$ and $\overline{X}_c = \overline{X}_d = \{\overline{\rho}_M, \overline{v}_M, \overline{\mu}_M\}$. The degree of freedom is given by equation B.12. Considering

$$\lambda = \left(\frac{\partial Re_M}{\partial \rho_M}\bigg|_{\overline{X}_a} P_{\rho_M} \right)^2, \quad \xi = \left(\frac{\partial Re_M}{\partial v_M}\bigg|_{\overline{X}_b} P_{v_M} \right)^2,$$

and

$$\gamma = \left(\frac{\partial Re_M}{\partial \mu_M}\bigg|_{\overline{X}_d} P_{\mu_M} \right)^2,$$

the mixture Reynolds number degree of freedom is given by

$$\nu_{Re_M} = \frac{[\lambda + \xi + \gamma]^2}{\frac{\lambda^2}{N-1} + \frac{\xi^2}{N-1} + \frac{\gamma^2}{N-1}}. \tag{B.130}$$

Then, the mixture Reynolds number uncertainty is given by

$$Re_M = \overline{Re}_M \pm (B_{Re_M} + t_{\nu_{Re_M},95} P_{Re_M}). \tag{B.131}$$

B.4 Calculated uncertainty

The mean and the uncertainty (u_x) for each transducer and property presented above are presented in the Tables B.1, B.2, B.3, B.4 and B.5.

Table B.1: Measured GVF, homogeneous GVF and superficial velocities.

	GVF (%)		H. GVF (%)		v_{SL} ($\mathrm{m\,s^{-1}}$)		v_{SG} ($\mathrm{m\,s^{-1}}$)	
Acq.	Mean	u_x	Mean	u_x	Mean	u_x	Mean	u_x
1	22.2195	1.0307	30.2758	2.3897	0.5418	0.0610	0.2123	0.0194
2	32.1045	2.9182	40.0173	2.9306	0.5411	0.0609	0.3349	0.0282
3	46.9434	5.2984	54.4301	3.6143	0.5402	0.0608	0.6138	0.0495
4	51.0123	2.4197	68.2740	4.3890	0.5414	0.0610	1.1300	0.0898
5	64.4682	8.6301	79.4806	5.2974	0.5384	0.0606	2.0447	0.1619
6	60.3018	7.1888	86.9002	6.0851	0.5427	0.0611	3.5601	0.2812
7	64.9159	3.2063	82.6032	5.6181	0.7604	0.0856	3.5876	0.2834
8	56.0517	6.6579	73.2483	4.7626	0.7607	0.0857	2.0611	0.1628
9	50.9624	3.2418	60.9099	3.9648	0.7609	0.0857	1.1679	0.0928
10	38.3651	3.7140	46.8964	3.2969	0.7609	0.0857	0.6584	0.0532
11	25.1113	3.7874	32.2881	2.5903	0.7613	0.0857	0.3547	0.0304
12	17.0268	1.1506	21.7889	1.9397	0.7580	0.0853	0.2058	0.0195
14	18.3429	1.0318	24.8122	2.1484	1.0537	0.1186	0.3438	0.0287
15	33.8064	2.6080	38.5830	2.9113	1.0517	0.1184	0.6540	0.0525
16	44.5320	3.9440	52.6003	3.5539	1.0466	0.1178	1.1515	0.0914
17	54.3550	2.7053	66.0490	4.2691	1.0451	0.1177	2.0211	0.1600
18	61.2887	5.9341	77.3156	5.1040	1.0497	0.1182	3.5657	0.2811
19	56.5463	2.7131	70.3939	4.5554	1.5052	0.1695	3.5737	0.2818
20	47.1270	1.0000	57.8068	3.8046	1.5049	0.1694	2.0571	0.1623
21	37.0212	1.4911	42.1198	3.0826	1.5011	0.1690	1.0890	0.0866
22	26.0588	2.5045	30.1869	2.4816	1.5008	0.1690	0.6471	0.0524
23	15.0911	1.3701	19.4956	1.7962	1.4974	0.1686	0.3623	0.0312
24	7.8255	1.6044	12.4501	1.2351	1.4998	0.1689	0.2132	0.0196
25	4.2288	0.5285	8.4046	0.8707	2.1369	0.2406	0.1965	0.0182
26	9.8371	1.9923	14.3929	1.3981	2.1375	0.2407	0.3594	0.0299
27	18.8022	0.7732	22.6608	2.0147	2.1317	0.2400	0.6240	0.0501
28	28.1623	0.8674	34.4358	2.7094	2.1319	0.2400	1.1188	0.0887
29	39.2876	0.9414	47.9506	3.3445	2.1286	0.2397	1.9595	0.1547
30	49.5712	1.9485	63.2811	4.0990	2.1268	0.2395	3.6644	0.2888
31	36.8073	0.7453	51.8937	3.5221	2.9830	0.3359	3.2182	0.2536
32	29.4763	0.5536	40.8570	3.0225	2.9690	0.3343	2.0508	0.1618
33	17.7636	1.4763	27.2174	2.3066	2.9629	0.3336	1.1079	0.0880
34	11.9144	0.5752	18.1457	1.6941	2.9571	0.3329	0.6559	0.0531
35	4.0036	1.4158	11.0652	1.1152	2.9560	0.3328	0.3687	0.0318
36	5.4442	0.4493	6.2446	0.6618	2.9569	0.3329	0.1975	0.0182

Table B.2: Liquid and gas specific mass and viscosity.

	ρ_L ($\mathrm{kg\,m^{-3}}$)		ρ_G ($\mathrm{kg\,m^{-3}}$)		μ_L ($\mathrm{Pa\,s}\ 10^4$)		μ_G ($\mathrm{Pa\,s}\ 10^5$)	
Acq.	Mean	u_x	Mean	u_x	Mean	u_x	Mean	u_x
1	994.6622	0.0644	1.5797	0.0013	7.5249	0.0309	1.8688	0.0008
2	994.6693	0.0643	1.5406	0.0013	7.5283	0.0309	1.8687	0.0008
3	994.6904	0.0642	1.4850	0.0013	7.5384	0.0310	1.8684	0.0008
4	994.6911	0.0642	1.4367	0.0013	7.5388	0.0310	1.8684	0.0008
5	994.6994	0.0642	1.4186	0.0013	7.5428	0.0310	1.8683	0.0008
6	994.9063	0.0631	1.4176	0.0013	7.6446	0.0316	1.8653	0.0008
7	994.8989	0.0632	1.4509	0.0013	7.6409	0.0316	1.8654	0.0008
8	995.0591	0.0624	1.4574	0.0013	7.7224	0.0322	1.8631	0.0008
9	995.0762	0.0623	1.4784	0.0013	7.7312	0.0322	1.8628	0.0008
10	995.0515	0.0624	1.5217	0.0013	7.7184	0.0321	1.8632	0.0008
11	995.0296	0.0625	1.5736	0.0013	7.7071	0.0321	1.8635	0.0008
12	995.0575	0.0624	1.6130	0.0014	7.7215	0.0322	1.8631	0.0008
14	993.7615	0.0686	1.5901	0.0013	7.1244	0.0283	1.8812	0.0008
15	993.7899	0.0685	1.5454	0.0013	7.1362	0.0284	1.8808	0.0008
16	993.8574	0.0682	1.5105	0.0013	7.1643	0.0286	1.8799	0.0008
17	993.8724	0.0681	1.4887	0.0013	7.1705	0.0286	1.8797	0.0008
18	993.8368	0.0683	1.4859	0.0013	7.1557	0.0285	1.8802	0.0008
19	993.7529	0.0687	1.5700	0.0013	7.1210	0.0283	1.8813	0.0008
20	993.7071	0.0689	1.5589	0.0013	7.1022	0.0282	1.8819	0.0008
21	993.6367	0.0692	1.5762	0.0013	7.0736	0.0280	1.8828	0.0008
22	993.5660	0.0695	1.5997	0.0013	7.0451	0.0278	1.8838	0.0008
23	993.5576	0.0695	1.6277	0.0013	7.0417	0.0278	1.8839	0.0008
24	993.5582	0.0695	1.6498	0.0013	7.0420	0.0278	1.8839	0.0008
25	993.8623	0.0682	1.7025	0.0014	7.1667	0.0286	1.8798	0.0008
26	993.7743	0.0686	1.6947	0.0014	7.1300	0.0283	1.8810	0.0008
27	993.7667	0.0686	1.6809	0.0014	7.1269	0.0283	1.8811	0.0008
28	993.7598	0.0686	1.6703	0.0014	7.1241	0.0283	1.8812	0.0008
29	993.9839	0.0676	1.6724	0.0014	7.2181	0.0289	1.8782	0.0008
30	993.9363	0.0678	1.6969	0.0014	7.1980	0.0288	1.8788	0.0008
31	993.9502	0.0678	1.7038	0.0014	7.2043	0.0288	1.8787	0.0008
32	994.2226	0.0665	1.7082	0.0014	7.3227	0.0296	1.8750	0.0008
33	994.2149	0.0665	1.7081	0.0014	7.3193	0.0295	1.8751	0.0008
34	994.1656	0.0668	1.7073	0.0014	7.2974	0.0294	1.8757	0.0008
35	994.1524	0.0668	1.7071	0.0014	7.2916	0.0294	1.8759	0.0008
36	994.1663	0.0668	1.7073	0.0014	7.2977	0.0294	1.8757	0.0008

Table B.3: Mixture properties and homogeneous mixture Reynolds number.

	v_M ($\mathrm{m\,s^{-1}}$)		ρ_M ($\mathrm{kg\,m^{-3}}$)		μ_M ($\mathrm{Pa\,s}\ 10^4$)		Re (-)	
Acq.	Mean	u_x	Mean	u_x	Mean	u_x	Mean	u_x
1	0.7541	0.0640	693.9956	23.7317	5.3016	0.1767	51816	5440
2	0.8760	0.0671	597.2429	29.1049	4.5889	0.2159	59310	6557
3	1.1540	0.0784	454.0850	35.8974	3.5356	0.2661	77922	10459
4	1.6714	0.1085	316.5548	43.5944	2.5184	0.3228	111024	22376
5	2.5832	0.1729	205.2328	52.6182	1.6954	0.3897	160766	57947
6	4.1028	0.2877	131.5615	60.4545	1.1630	0.4538	258935	148193
7	4.3480	0.2961	174.2779	55.8133	1.4830	0.4188	267279	116476
8	2.8217	0.1840	267.2614	47.3211	2.2017	0.3590	179516	45397
9	1.9288	0.1263	389.8747	39.3943	3.1346	0.2994	125873	19976
10	1.4193	0.1009	529.1194	32.7553	4.1848	0.2489	94211	11130
11	1.1160	0.0909	674.2588	25.7335	5.2772	0.1960	74876	7856
12	0.9638	0.0875	778.5937	19.2704	6.0777	0.1483	64844	6796
14	1.3975	0.1221	747.5822	21.3163	5.4033	0.1505	101535	10526
15	1.7057	0.1295	610.9520	28.8871	4.4555	0.2030	122825	13233
16	2.1981	0.1491	471.8806	35.2672	3.4949	0.2483	155844	20179
17	3.0662	0.1986	338.4134	42.3663	2.5588	0.2983	212869	39827
18	4.6154	0.3049	226.5947	50.6497	1.7688	0.3557	310222	96334
19	5.0789	0.3288	295.3174	45.1976	2.2409	0.3159	351430	77809
20	3.5620	0.2347	420.1789	37.7477	3.1057	0.2633	253072	36783
21	2.5900	0.1899	575.7836	30.5817	4.1737	0.2129	187639	20833
22	2.1479	0.1769	694.1227	24.6171	4.9754	0.1713	157354	16321
23	1.8598	0.1715	800.1747	17.8175	5.7056	0.1251	136958	14370
24	1.7130	0.1700	870.0642	12.2514	6.1886	0.0881	126461	13726
25	2.3333	0.2413	910.4755	8.6389	6.5801	0.0662	169545	18890
26	2.4969	0.2425	850.9852	13.8702	6.1309	0.1000	182001	19513
27	2.7557	0.2452	768.9525	19.9881	5.5546	0.1415	200344	20792
28	3.2506	0.2559	652.1258	26.8801	4.7358	0.1888	235079	24673
29	4.0881	0.2852	518.1647	33.1874	3.8472	0.2356	289169	34516
30	5.7912	0.3752	366.0368	40.6722	2.7621	0.2875	403044	68517
31	6.2012	0.4209	479.0371	34.9479	3.5633	0.2475	437842	55861
32	5.0198	0.3714	588.7109	29.9983	4.4076	0.2164	352146	38586
33	4.0708	0.3450	724.0804	22.8934	5.3782	0.1659	287843	29722
34	3.6130	0.3372	814.0770	16.8135	6.0071	0.1228	257149	27069
35	3.3247	0.3343	884.3355	11.0678	6.5053	0.0834	237369	25960
36	3.1544	0.3334	932.1903	6.5680	6.8535	0.0545	225342	25506

Table B.4: Pressure transducers.

	PT-101 (kPa)		PT-102 (kPa)		PT-301 (kPa)		PDT-101 (kPa)	
Acq.	Mean	u_x	Mean	u_x	Mean	u_x	Mean	u_x
1	295.1073	2.5501	206.6305	2.5513	138.8763	0.0758	0.1130	0.0051
2	292.3200	2.5501	197.0068	2.5513	135.4291	0.0759	0.1750	0.0051
3	283.9244	2.5503	181.8561	2.5516	130.5167	0.0763	0.3186	0.0051
4	272.7003	2.5500	167.6625	2.5513	126.2706	0.0773	0.5895	0.0051
5	253.2465	2.5504	159.8431	2.5516	124.6690	0.0774	1.1325	0.0051
6	275.0597	2.5501	156.0221	2.5514	124.3164	0.0777	1.8162	0.0051
7	271.8495	2.5502	164.1079	2.5515	127.2494	0.0774	1.8922	0.0051
8	318.6444	2.5502	168.6771	2.5514	127.6137	0.0768	0.9311	0.0051
9	340.2409	2.5503	177.0222	2.5516	129.4305	0.0767	0.5015	0.0051
10	351.7692	2.5501	189.6993	2.5513	133.2552	0.0761	0.2815	0.0051
11	359.3324	2.5503	203.3486	2.5514	137.8231	0.0758	0.1533	0.0051
12	333.2660	2.5504	212.8985	2.5516	141.2368	0.0758	0.0986	0.0051
14	287.3879	2.5496	211.5801	2.5508	141.0022	0.0758	0.1894	0.0051
15	280.8636	2.5497	199.7987	2.5510	137.0043	0.0758	0.3584	0.0051
16	270.6952	2.5498	188.7053	2.5510	133.8224	0.0761	0.6416	0.0051
17	251.4554	2.5497	180.1479	2.5510	131.8723	0.0764	1.1943	0.0051
18	324.1344	2.5496	175.5303	2.5509	131.6680	0.0769	1.6348	0.0051
19	317.7245	2.5497	194.2800	2.5509	139.2280	0.0763	1.7694	0.0051
20	362.1683	2.5498	196.8375	2.5510	138.3070	0.0761	0.8849	0.0051
21	384.1093	2.5498	204.9394	2.5510	139.9297	0.0759	0.4461	0.0051
22	393.4508	2.5497	212.7317	2.5508	142.1051	0.0758	0.2627	0.0051
23	401.6758	2.5498	220.3643	2.5510	144.6053	0.0758	0.1464	0.0051
24	322.3180	2.5496	225.7018	2.5508	146.5693	0.0757	0.1088	0.0051
25	318.0723	2.5496	237.9667	2.5507	150.8254	0.0757	0.1047	0.0051
26	313.2893	2.5498	233.9908	2.5509	150.2576	0.0758	0.1932	0.0051
27	306.0952	2.5496	229.6441	2.5507	149.0503	0.0758	0.3403	0.0051
28	293.9255	2.5497	224.8278	2.5509	148.1153	0.0758	0.6314	0.0051
29	341.0097	2.5498	220.9846	2.5509	147.9895	0.0759	0.9541	0.0051
30	334.5395	2.5496	220.8798	2.5508	150.2270	0.0759	1.8432	0.0051
31	350.0383	2.5499	257.0351	2.5510	150.8185	0.0757	1.5521	0.0051
32	385.3182	2.5498	253.4260	2.5509	150.8209	0.0757	0.9014	0.0051
33	408.3162	2.5497	252.5565	2.5507	150.8213	0.0757	0.4595	0.0051
34	421.5361	2.5499	253.4745	2.5510	150.8238	0.0757	0.2629	0.0051
35	430.6344	2.5499	254.1911	2.5510	150.8240	0.0757	0.1447	0.0051
36	312.3041	2.5499	252.8599	2.5510	150.8224	0.0757	0.1068	0.0051

Table B.5: Temperature transducers and Coriolis flow meter.

	TT-101 (°C)		TT-102 (°C)		TT-301 (°C)		FT-101 ($\mathrm{kg\,min^{-1}}$)	
Acq.	Mean	u_x	Mean	u_x	Mean	u_x	Mean	u_x
1	29.1688	0.1963	33.1041	0.1961	33.1089	0.1961	69.9978	1.3792
2	28.6650	0.1963	33.1087	0.1961	33.0873	0.1961	69.9017	1.3774
3	29.1178	0.1963	33.0841	0.1961	33.0231	0.1961	69.7918	1.3754
4	28.7627	0.1963	33.0633	0.1961	33.0208	0.1961	69.9417	1.3783
5	28.3211	0.1963	33.0229	0.1961	32.9955	0.1961	69.5633	1.3712
6	28.7858	0.1963	32.1694	0.1961	32.3583	0.1961	70.1334	1.3819
7	28.2318	0.1963	32.4816	0.1961	32.3812	0.1961	98.2610	1.9310
8	27.9965	0.1963	32.3661	0.1961	31.8805	0.1961	98.3111	1.9318
9	28.0323	0.1963	31.7606	0.1961	31.8268	0.1961	98.3458	1.9324
10	27.9702	0.1963	31.8834	0.1961	31.9045	0.1961	98.3418	1.9323
11	27.1598	0.1963	31.9348	0.1961	31.9735	0.1961	98.3834	1.9331
12	27.3809	0.1963	31.9116	0.1961	31.8860	0.1961	97.9602	1.9251
14	30.4112	0.1963	35.7538	0.1961	35.7646	0.1961	136.0105	2.6690
15	30.5582	0.1963	35.6924	0.1961	35.6834	0.1961	135.7501	2.6639
16	31.3741	0.1963	35.5332	0.1961	35.4897	0.1961	135.1062	2.6516
17	31.2814	0.1963	35.3738	0.1961	35.4466	0.1961	134.9129	2.6479
18	31.9339	0.1963	35.3330	0.1961	35.5488	0.1961	135.4995	2.6591
19	32.4522	0.1963	35.4195	0.1961	35.7887	0.1961	194.2883	3.8102
20	31.6015	0.1963	35.4635	0.1961	35.9193	0.1961	194.2343	3.8090
21	31.2648	0.1963	35.5537	0.1961	36.1194	0.1961	193.7256	3.7991
22	31.3784	0.1963	35.8071	0.1961	36.3192	0.1961	193.6733	3.7980
23	30.7818	0.1963	35.9946	0.1961	36.3433	0.1961	193.2435	3.7897
24	30.7200	0.1963	36.0011	0.1961	36.3415	0.1961	193.5471	3.7955
25	30.1900	0.1963	35.5492	0.1961	35.4745	0.1961	275.8449	5.4078
26	29.6584	0.1963	35.7297	0.1961	35.7269	0.1961	275.8966	5.4087
27	29.6574	0.1963	35.4819	0.1961	35.7489	0.1961	275.1473	5.3941
28	29.6353	0.1963	35.0312	0.1961	35.7684	0.1961	275.1686	5.3944
29	29.5974	0.1963	35.2612	0.1961	35.1233	0.1961	274.8068	5.3874
30	29.2633	0.1963	35.2633	0.1961	35.2608	0.1961	274.5628	5.3826
31	28.9798	0.1963	35.2789	0.1961	35.2195	0.1961	385.1015	7.5487
32	29.1683	0.1963	35.2064	0.1961	34.4238	0.1961	383.4027	7.5154
33	29.1783	0.1963	34.6612	0.1961	34.4466	0.1961	382.6082	7.4999
34	28.4996	0.1963	34.3099	0.1961	34.5920	0.1961	381.8382	7.4849
35	28.4755	0.1963	34.5129	0.1961	34.6305	0.1961	381.6990	7.4821
36	28.0228	0.1963	34.6960	0.1961	34.5900	0.1961	381.8201	7.4845

C Closure relationships

C.1 V_{TB} obtained

The values of the V_{TB} and the standard deviation between the repetitions of the proposed method and the literature correlation are presented in Table C.1 and Table C.2.

Table C.1: Mean V_{TB} and its standard deviation between the repetitions in $\mathrm{m\,s^{-1}}$of the vibration method and the Nicklin, Wilkes and Davidson [67], Bendiksen [68] and Théron [70] correlations.

	Vibration		Nicklin (1962)		Bendiksen (1984)		Théron (1989)	
Acq.	Mean	Std.	Mean	Std.	Mean	Std.	Mean	Std.
1	1.2075	0.0413	1.1583	0.0012	1.1576	0.0012	1.1576	0.0012
2	1.3268	0.0276	1.3044	0.0041	1.3037	0.0041	1.3037	0.0041
3	1.7886	0.0620	1.6382	0.0026	1.6375	0.0026	1.6375	0.0026
4	2.9464	0.1149	2.2581	0.0102	2.2574	0.0102	2.2574	0.0102
5	4.1680	0.0851	3.3523	0.0157	3.3515	0.0157	3.3515	0.0157
6	5.7906	0.1590	5.1743	0.0175	5.1736	0.0175	5.1736	0.0175
7	5.9947	0.0802	5.4695	0.0103	5.4687	0.0103	5.4687	0.0103
8	4.3971	0.1459	3.6388	0.0046	3.6381	0.0046	3.6381	0.0046
9	3.0399	0.0770	2.5679	0.0039	2.5672	0.0039	2.5672	0.0039
10	2.1793	0.0841	1.9565	0.0017	1.9558	0.0017	1.9558	0.0017
11	1.6974	0.0236	1.5928	0.0012	1.5921	0.0012	1.5921	0.0012
12	1.4562	0.0275	1.4104	0.0029	1.4096	0.0029	1.4096	0.0029
14	1.9638	0.0097	1.9305	0.0021	1.9298	0.0021	1.9298	0.0021
15	2.4084	0.0067	2.3003	0.0047	2.2996	0.0047	2.2996	0.0047
16	3.2146	0.0557	2.8910	0.0051	2.8903	0.0051	2.8903	0.0051
17	4.5189	0.0517	3.9322	0.0153	3.9314	0.0153	3.9314	0.0153
18	6.1456	0.0285	5.7902	0.0124	5.7895	0.0124	5.7895	0.0124
19	6.5498	0.0443	6.3477	0.0102	6.3470	0.0102	6.3470	0.0102
20	4.9400	0.0471	4.5282	0.0037	4.5275	0.0037	4.5275	0.0037
21	3.5569	0.0080	3.3622	0.0035	3.3615	0.0035	3.3615	0.0035
22	2.9595	0.0131	2.8316	0.0013	2.8309	0.0013	2.8309	0.0013
23	2.5410	0.0192	2.4862	0.0007	2.4855	0.0007	2.4855	0.0007
24	2.3905	0.0428	2.3099	0.0034	2.3092	0.0034	2.3092	0.0034
27	3.7356	0.0450	3.5619	0.0049	3.5612	0.0049	3.5612	0.0049
28	4.3462	0.0528	4.1560	0.0063	4.1552	0.0063	4.1552	0.0063
29	5.4951	0.0539	5.1606	0.0060	5.1599	0.0060	5.1599	0.0060
30	7.2459	0.0529	7.2037	0.0159	7.2030	0.0159	7.2030	0.0159
31	0.3879	0.1561	7.6974	0.0178	7.6967	0.0178	7.6967	0.0178

Table C.2: Mean V_{TB} and its standard deviation between the repetitions in $\mathrm{m\,s^{-1}}$of the vibration method and the Petalas and Aziz [71] and Dukler, Moalem Maron and Brauner [69] correlations.

	Vibration		Petalas and Aziz (2000)		Dukler (1985)	
Acq.	Mean	Std.	Mean	Std.	Mean	Std.
1	1.2075	0.0413	0.9495	0.0012	0.9253	0.0012
2	1.3268	0.0276	1.0975	0.0042	1.0744	0.0042
3	1.7886	0.0620	1.4333	0.0026	1.4152	0.0027
4	2.9464	0.1149	2.0506	0.0101	2.0480	0.0104
5	4.1680	0.0851	3.1265	0.0154	3.1649	0.0160
6	5.7906	0.1590	4.8953	0.0168	5.0250	0.0179
7	5.9947	0.0802	5.1794	0.0099	5.3263	0.0106
8	4.3971	0.1459	3.4085	0.0044	3.4575	0.0047
9	3.0399	0.0770	2.3585	0.0039	2.3643	0.0040
10	2.1793	0.0841	1.7523	0.0017	1.7401	0.0017
11	1.6974	0.0236	1.3887	0.0012	1.3688	0.0012
12	1.4562	0.0275	1.2053	0.0029	1.1826	0.0030
14	1.9638	0.0097	1.7224	0.0022	1.7135	0.0022
15	2.4084	0.0067	2.0891	0.0047	2.0911	0.0048
16	3.2146	0.0557	2.6707	0.0050	2.6941	0.0052
17	4.5189	0.0517	3.6862	0.0148	3.7569	0.0156
18	6.1456	0.0285	5.4771	0.0118	5.6537	0.0126
19	6.5498	0.0443	6.0098	0.0096	6.2228	0.0104
20	4.9400	0.0471	4.2622	0.0037	4.3654	0.0038
21	3.5569	0.0080	3.1304	0.0034	3.1751	0.0036
22	2.9595	0.0131	2.6112	0.0012	2.6335	0.0013
23	2.5410	0.0192	2.2716	0.0007	2.2808	0.0007
24	2.3905	0.0428	2.0977	0.0034	2.1009	0.0035
27	3.7356	0.0450	3.3257	0.0047	3.3789	0.0050
28	4.3462	0.0528	3.9025	0.0061	3.9854	0.0065
29	5.4951	0.0539	4.8739	0.0058	5.0109	0.0061
30	7.2459	0.0529	6.8279	0.0150	7.0966	0.0162
31	0.3879	0.1561	7.2975	0.0168	7.6006	0.0182